Spectral Hole Burning for Ultra-stable Lasers

Shuo Zhang

PSL UNIVERSITÉ PARIS

THÈSE DE DOCTORAT
DE L'UNIVERSITÉ PSL

Préparée à l'Observatoire de Paris

Trous Brûlés Spectraux pour Les Lasers Ultra-stables
Spectral Hole Burning for Ultra-stable Lasers

Soutenue par
Shuo ZHANG
Le 13 Avril 2022

Ecole doctorale n° 564
Ecole Doctorale Physique en Ile de France

Spécialité
Physique

Composition du jury :

Frederic DU BURCK Professor, Université Sorbonne Paris Nord (LPL)	*Rapporteur*
Marie HOUSSIN Professor, Université Aix-Marseilles (PIIM)	*Rapporteur*
Alexandre TALLAIRE CNRS Research Director (IRCP), Institut de Recherche de Chimie Paris	*Examinateur*
Perinne BERGER Doctor, Thalès	*Examinateur*
Yann LE COQ CNRS Research Engineer, Observatoire de Paris (SYRTE)	*Directeur de thèse*
Bess FANG SORTAIS Associate Astronomer, Observatoire de Paris (SYRTE)	*Codirecteur de thèse*
Signe SEIDELIN Associate Professor, Université Grenoble Alpes(Institut Néel)	*Codirecteur de thèse*

SYRTE l'Observatoire de Paris | PSL
SYstèmes de Référence Temps-Espace

Acknowledgment

This PhD work has been carried out at the SYRTE laboratory (Systèmes de Référence Temps-Espace) at Observatoire de Paris, in collaboration with Institut Néel and Chime Paris. I would like to give acknowledgments here to all the people who have helped me directly or indirectly in the past three and half years. Without them, it will be impossible for me to finish this PhD thesis with so many interesting scientific results and joyful memories in the heart of the most beautiful city in the world, Paris.

I would like to thank Frederick Du Burck and Marie Houssin, who have accepted to review this work, as well as Alexandre Tallaire and Perinne Berger for being part of the jury for my defense.

I would like to sincerely thank my supervisor Yann Le Coq, who is a role model to me, a great scientist that I hope I could become in the future. Yann gave me massive support during my PhD project whenever I encountered difficulties and problems, not only in the scientific research but also in the daily life. Thanks to his supervision and guidance, my research can be carried out very efficiently in the right direction. I feel so grateful to have such a wise and patient man as my supervisor!

I would like to thank my co-supervisor Bess Fang Sortais, who kindly spent lots of time with me in the lab, helping me to master the experimental techniques and explaining me the principle of our work with great patience. She was always there whenever I needed her, and she is definitely the one from whom I learnt the most directly. I appreciate the way that she devoted herself to the lab, and I feel really

lucky to have had her supervising me during my PhD work.

It's also my great honor to work with Signe Seidelin, my other co-supervisor from Institut Néel, who is extremely kind and warmhearted. The work with Signe is always pleasant and productive, which makes me feel the joy of scientific research. She is willing to hear my opinion all the time and encourage me to put forward my own ideas in discussions, which means a lot to me. Signe is more than a teacher for me, and I am more grateful than I can express.

Next, I would never forget my dear colleagues in the SHB lab. My thanks first go to my two elder brothers: Nemanja Lučić, a super creative man who is always willing to share his genius idea; and Nicolas Galland, who is always enthusiastic and makes experimental work more fun. I will always remember those beautiful days that we spent together, and I wish them all the best in the future. I am also very glad to have met Xiuji Lin and Michael Hartman at the end of my PhD. I Hope you enjoy the time in Paris and have great success in research, realizing the final goal of our lab.

Moreover, It is also my great pleasure to have met all the lovely colleagues in SYRTE. My special thanks go to:

- Sebastien Bize, the group leader of the optical frequency group (FOP). He is always happy for discussions and he loves to share his solid knowledge and insightful ideas with others. I would also like to thank his kind encouragement every time I give talk in FOP group meeting.

- Rodolphe Le Targat, who is in charge of the frequency comb in the lab. I have worked a lot with him to measure our laser frequency stability, which is critical for my experiments. Without Rodolphe, it is impossible to finish my work in the SHB lab.

- Jérome Lodewyck, who is in charge of strontium optical lattice clocks and also very proficient in all programming languages. Thank you Jérome for your kind

advice on the optical path design and programming work.

- Sébastien Lambert and Sébastien Merlet, who are my tutor and parrain in the doctoral school. The suggestions from them make my thesis project go smoothly.

- My officemates Fatima Rahmouni, Benjamin Pointard, and Fatim Hankard. Their positive and optimistic attitude towards life and work makes our office a very pleasant place full of laughter.

- Also I will never forget my dear friends, the PhD students and postdocs: William Moreno and Yannick Foucault (for helping me move those heavy machines); Héctor Álvarez Martínez (for spending a lot of time in measuring the frequency stability); Angélique Lartaux, Manuel Andia, Clara Zyskind, Jesus Romero, Miguel Cifuentes, Mads Tønnes, Alexis Mehlman (for the lunches we had together and the good times we chatted in the garden); Changlei Guo, Yuejiao Zi, Dan Xu, and Haosen Shang (for our scientific discussion in Chinese and the time we shared our local food). I appreciate the interesting scientific discussion and the spare time we spent together. I Hope they are all doing great in the current work and hope to see them again in the near future!

- David Holleville, Benoît Carré, Bertrand Venon for their help to design and fix mechanical devices. Michel Lours, José Pinto, Laurent Volodimer for their patience in explaining the electric diagram and advice in all the electrical technical issues. Pascal Blondé, Maxime Laiguillon, Teddy Carlucci for their kind help in solving the IT problems in the daily work and also the professional support for my defense online.

Finally, I would like to thank my family, who have been given me unconditional support and endless love. A special thank goes to my fiancé Jiawen Liu and our cute dog Momo, who make my life in Paris so lovely and unforgettable!

Acronyms

ADC	Analog to Digital Converters
AOM	Acousto-Optic Modulator
DAC	Digital to Analog Converters
E-field	Electric Field
Eu:YSO	Eu^{3+}:Y_2SiO_5
FFT	Fast Fourier Transform
FPGA	Field-Programmable Gate Array
FWHM	Full Width at Half Maximum
IFFT	Inverse Fast Fourier Transform
IVC	Inner Vacuum Chamber
MSPS	Mega Sample per Second
OVC	Outside Vacuum Chamber
PBS	Polarizing Beam Splitter
PD	Photo Diode
PDH	Pound–Drever–Hall
PPLN	Periodically Poled Lithium Niobate
REI	Rare Earth Ion
RF	Radio Frequency
RMS	Root Mean Square
SDR	Software Defined Radio
SH	Spectral Hole
SHB	Spectral Hole Burning
SYRTE	Systèmes de Référence Temps-Espace
USRP	Universal Software Radio Peripheral
YSO	Y_2SiO_5

Introduction

Rare-earth ions (REI) doped into a crystalline matrix have since the nineties proven to be excellent candidates for an ever growing number of applications due to their exceptional coherence properties [1, 2]. Examples of recent applications are as varied as ranging from information processing schemes [3] and quantum optical memories [4, 5] to laser stabilization techniques [6, 7] - the latter being one of the major motivations of the work presented in this manuscript.

The REI doped crystals have not only been exploited for the outstanding properties of the optical transitions [8], but also for using the spin degrees of freedom in the ions as well [9]. This allows the access of a wide range of frequencies, which holds promise for novel spin-optical transduction schemes [10], which in turn constitutes an important building block for several quantum processing schemes [11]. Other recent proposals for rare-earth doped crystals include combining the internal optical degrees of freedom of the ions with the mechanical degrees of freedom of the crystalline matrix itself, which for instance can be shaped as a resonator of which the vibrations can be efficiently coupled to a narrow optical transition [12, 13].

Despite the fact that the coherence properties of the REI have been studied extensively for more than 30 years, far from all the characteristics of this system required to proceed further in the technological applications are currently known. This is in part due to the high complexity of the system, but also, as the applications are getting more and more advanced, effects that previously were considered only negligible - or

even invisible - are starting to be the limiting factors for exploiting the technology to its fullest potential.

In particular, for a laser stabilization technique -in which a laser is frequency locked to a narrow optical transition in a REI- to be successful, all sources of noise must be carefully characterized, in order to reduce them to an absolute minimum. In the course of this thesis, two major contributions to the instability of an optical transition have been identified: 1) the effect of external electrical fields to the crystal, arising from the environment in particular due to surrounding equipment, and 2) the mechanical stress on the host crystal, arising for instance due to the vibrations of the cryostat. The effect of electrical fields and uniaxial stress have therefore been extensively studied in the thesis, in order to characterize their quantitative impact on the optical transition, within field directions and ranges so far unexplored, and with an uncertainly well below earlier measurements. Moreover, we have conducted studies on the effect of pressure variation inside the cryogenic set-up, allowing to confirm the position of a pressure "sweet-spot" for which the optical transition is almost insensitive to temperature fluctuations.

State-of-the-art of ultra-stable lasers

Lasers with ultra-high stability are required in many high-precision measurements, such as for the development of optical lattice clocks [14–18], gravitational wave detectors [19] or opto-electronic generation of ultra-low phase noise microwave signals [20]. Standard ultra-stable lasers use transmission peaks of a high-finesse Fabry-Perot cavity at room temperatures as frequency reference. In such systems, the stability imposed by the fundamental limitation arises from the thermal agitation of the atoms that constitute the Fabry-Perot cavity [21], a low 10^{-16} relative frequency stability for a timescale of approximately 1 second are reached [22, 23] in standard configurations. In order to significantly improve on the performance within this approach, radical modifications are required (such as increasing the cavity mode volume [24],

using crystalline materials for the spacer and mirror [25] or the mirror coatings [26], cooling down to cryogenic temperatures [27], or a combination of these approaches).

A different approach to frequency stabilization as mentioned above is to frequency lock a laser to a narrow optical transition in a REI dopant within a crystalline matrix. Or, more precisely, locking to a narrow spectral features previously photo-imprinted in rare-earth doped crystals by spectral-hole burning. Spectral features as narrow as 1 kHz have thus been observed in Eu^{3+}:Y_2SiO_5 crystals [28], with photon-echo experiments indicating the possibility to achieve structures as narrow as a few 100 Hz [29,30]. Recently, an experiment in the group of S. Schiller at Dusseldorf University effectively realized spectral holes below 1 kHz large at a temperature of 1.2 K and a polarizing magnetic field of 0.8 T [31]. Short term stability of 6×10^{-16} between 2 and 10 s have been demonstrated with this technique [28], making it hold promise of a better performance compared to standard Fabry Perot techniques. This constitutes the main motivation for investigating the Eu^{3+}:Y_2SiO_5 system in my thesis.

Outline of the thesis

The manuscript is divided into 3 chapters followed by the conclusion. The first chapter provides the background required to understand our physical set-up as well as the various experimental techniques utilized throughout the work. In particular, we give a detailed description of the technique of spectral hole burning, on which most of our results are presented in Ch. 1 including a novel detection method with multiple spectral holes and the temperature and pressure coupled environment which allows a global cancellation of their impact on the frequency of the spectral hole. In Ch. 2, we present the measurement on electric-field induced frequency displacements of our spectral ultra-narrow structure, both in the linear and quadratic regime. Ch. 3 is devoted to the measurements of the effect on the spectral structure of applying a calibrated uniaxial strain to the crystal. In the conclusion, I will discuss the utility of the results in the context of future applications, in particular in the field of frequency

metrology, but also beyond.

To briefly cite a few of the main results of this work, in order to get better frequency stability, our investigation of three holes probing allows us to get lower detection noise, paving the way to improve the laser frequency stability by increasing the number of holes in the probing structure. The detailed results are in Ch. 1 including the modification of the digital signal processing flowgraph, and employment of functional blocks to get cleaner spectrum and continuous phase sample.

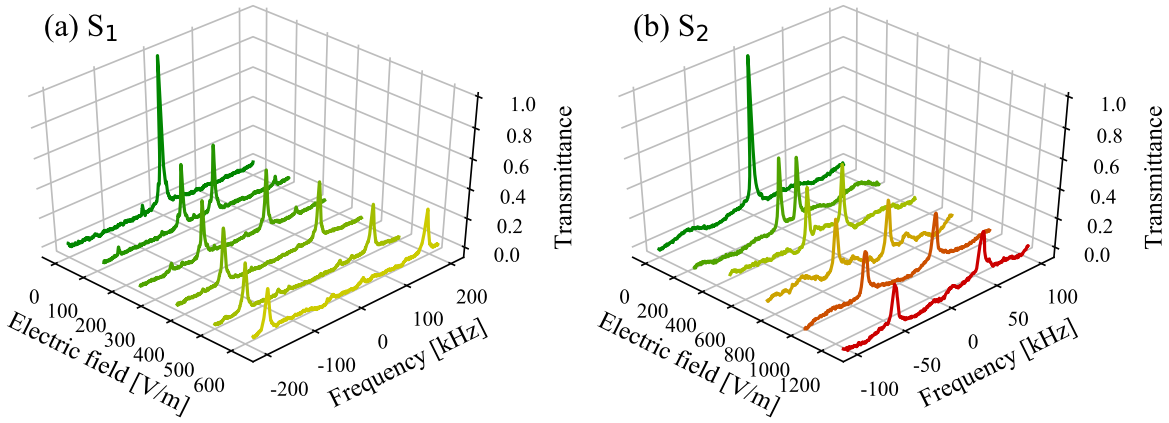

Figure 0-1: Transmittance of an Eu^{3+} doped crystal containing a spectral hole as a function of the electric field applied (see also Ch. 2 and ref [32]). Gradient colors used in plotting individual spectrum indicate the increase in electric field from green to red (0 $V.m^{-1}$ to 1250 $V.m^{-1}$ respectively).
.

Figure 0-1 (described in detail in Ch. 2) illustrates the behavior of the spectral structure (for two different crystal sites in our Eu^{3+} doped crystal, see Sec. 2.3.1) when an external electric field is applied and gradually increased. From these and similar measurements, we can extract both the linear and quadratic Stark shifts. Due to the precision of our measurements, we can provide an upper limit on the much smaller quadratic electric shifts, which potentially could be a limiting factor to the performance of a frequency locked ultra-stable laser.

One of the important results from Ch. 3 is the measurements of the mechanical

tunability of spectral feature by applying a calibrated uniaxial stress on the crystal, and from this, the strain sensitivity coefficients of our rare-earth doped ions (Eu^{3+}). Typical measurement are shown in Fig. 0-2.

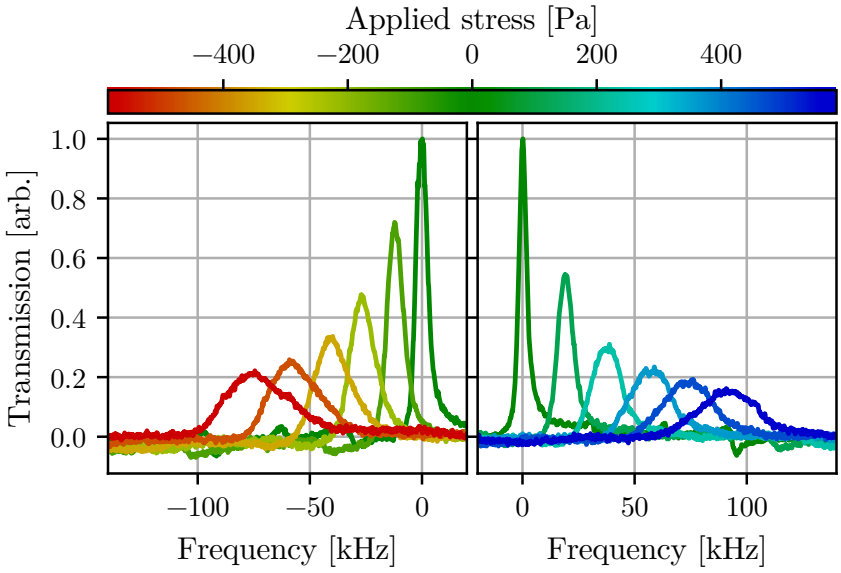

Figure 0-2: An example of the transmittance of an Eu^{3+} doped crystal containing a spectral hole as a function of applied stress. Measurements are carried out along D_1 axis and crystal site 2. (see also Ch. 3 and ref [6]).

The strain measurements are of relevance to the frequency stabilization techniques, in which stress on the crystal should be minimized in order to get better frequency stability. As mentioned above, recent articles propose to exploit stress as a resource in order to mechanically couple for instance the crystalline resonator to an optical transition. For such applications, knowledge of the strain sensitivity also plays a crucial role, and the results of our measurements can be directly transposed and exploited in this context as well. I have in parallel during my thesis participated in experiments preparing for the investigating such a mechanical resonator [13], in addition to experiments in which we for the first time have observed the inhomogeneous of the REI linewidth within this resonator. However, as this have not been the main focus of my work, I have not included a discussion of these aspects in the thesis.

Contents

Chapter 1

Experimental Techniques for Ultra-stable Lasers based on Spectral Hole Burning

This chapter is to present the spectral hole burning technique for ultra-stable lasers starting from a brief introduction of the spectral hole burning technique in Sec. 1.1, following with the specific crystal used as the hole burning material in our laboratory in Sec. 1.2. The experimental set-up is described in details in Sec. 1.3, including the optical path design and digital signal processing. To develop ultra-stable lasers, we frequency lock the laser onto the spectral holes, in order to benefit from the laser's frequency stability. The details about the spectral hole burning parameters and locking performance in our system are presented in Sec. 1.4. Our recent work to further improve the laser frequency stability is presented in Sec. 1.5, including the search of a temperature-pressure coupled 'magic environment', where we use coupled temperature and pressure fluctuations of a helium gas chamber surrounding the rare earth doped crystal to remove first order dependence of the spectral hole resonant frequency to temperature fluctuations, and the optimization of the digital signal generation and processing flowgraph in order to reach a lower detection noise level, overcoming our

previous limitations and paving the way to our future work about multiple modes probing. Note that this chapter focuses mostly on the most recent developments, but previous work (which is an useful background to this chapter), was published in [33], and is also described in great details in N. Galland's PhD dissertation [34].

1.1 Spectral Hole Burning Technique

Spectral Hole Burning (SHB) technique in rare earth ion doped crystal is a frequency selection method based on the optical transition of the dopant ions. The condition of the spectral hole to be burned is that the material needs to have an inhomogeneously broadened absorption spectrum, and in the meantime, the absorption spectrum can be modified so that the selection of the frequency can be achieved by pumping the crystal with a narrow-band laser. The ions at resonance with the laser are optically pumped away and eventually decay into one of the metastable hyperfine states, becoming off resonant with the incoming light. Spectral holes (SH) will then appear as a homogeneously broadened (if the pump laser is sufficiently narrow) transmission peaks imprinted on the inhomogeneously broadened absorption spectrum. It is then possible to frequency lock a laser on such a spectral hole, in a similar way as lasers are traditionally locked to absorption/transmission peaks of atomic or molecular samples or Fabry-Perot cavities.

An interesting application of this technique lies in that the resonant frequency of a spectral hole may be less sensitive to several environmental perturbations than other techniques used for frequency stabilization. In particular, the thermal Brownian noise, limiting the standard Fabry-Perot cavities at a low 10^{-16} fractional frequency stability at 1 s are expected to be below 10^{-18} for certain combinations of rare-earth ion and crystalline matrix. Therefore, spectral hole burning is a promising candidate for the development of the next generation of ultra-stable lasers.

1.2 Photo-imprinted Spectral Pattern in Eu^{3+}:Y_2SiO_5 System

In our laboratory, a crystal of Eu^{3+}:Y_2SiO_5 (Eu:YSO) is used as the spectral hole burning material, and the crystal is put in a cryostat to reach the cryogenic temperatures. The hyperfine structure of europium ions make it possible to let the crystal be transparent to the resonant frequency of a certain optical transition ($^7F_0 \rightarrow {}^5D_0$).

By pumping the crystal on this $^7F_0 \rightarrow {}^5D_0$ transition, a narrow spectral hole can be burnt. Full width half maximum linewidth of a few kHz are routinely realized in this material at SYRTE. Such linewidth is comparable with that of the high finesse Fabry-Perot cavity typically used in optical frequency metrology for laser stabilization.

Because of the cryogenic temperature at which it operates (with lower thermal excitations), and the high mechanical quality factor of crystalline materials (compared to the amorphous glass typically used for Fabry-Perot cavities), it is expected that the frequency of the spectral hole thus burned is much less impacted by thermal noise than the resonant frequency of a Fabry-Perot cavity [35, 36]. This section is to describe the spectral holes burnt in the Eu:YSO system that we used in the laser frequency stabilization.

1.2.1 Eu^{3+} ions Hyperfine Structure at Cryogenic Temperature

Europium ion has hyperfine structure for both $^7F_0$ and $^5D_0$ states, with the spin momentum difference of 1/2 for the sub-levels as it shown in Fig. 1-1. The energy difference between the sub-levels determines the absorption frequency difference when probing the crystal. The frequency separation between the sub-levels ranges from 30 MHz to 100 MHz [29, 37]. The coupling between them is weak.

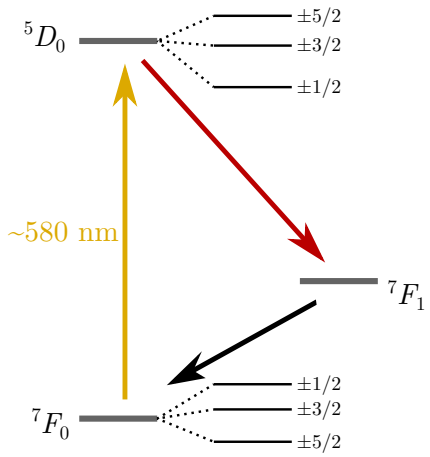

Figure 1-1: Energy level diagram of europium ions. Both the $^7F_0$ and $^5D_0$ states have hyperfine structure.

Ions Shelving through the Hyperfine Structure

By pumping the Eu^{3+}:Y_2SiO_5 crystal with yellow light (around 580 nm), ions in the $^7F_0$ state will firstly be excited to a higher energy level to one of the $^5D_0$ states, following with a spontaneous transition predominantly to the $^7F_1$ state accompanied by the emission of an orange fluorescence which wavelength is around 620 nm. Then, the ions will drop to the $^7F_0$ states with some of them off the resonance and are shelved on the other hyperfine state. The number of on-resonant ions will become less and less, leading to the crystal becoming transparent to the yellow light and providing necessary conditions for frequency-selection.

The cryogenic temperature allows ions in the dark state to have longer lifetime, which is the key point by which the spectral hole pattern can be printed and studied, and essentially providing frequency reference for achieving ultra-stable lasers.

Once the ions are in the dark states, the number of the involved ions will have influence on the contrast of the transition as the absorption spectrum is an average behavior of an ions ensemble. Therefore the crystal doping level, which determines the dopant ions number in a certain crystal, will directly affect spectral holes transmittance. In this thesis, the Eu^{3+}:Y_2SiO_5 (Eu:YSO) crystal used in all measurements has a doping level of 0.1%.

1.2.2 Photo-imprinted Spectral Pattern

Inhomogeneously Broadened Absorption Profile

The ideal perfect crystal would let all the Eu^{3+} ions have the same crystal environment, making the absorption frequency be the same for each individual ions (Fig. 1-2 left bottom). Therefore the absorption spectrum of a perfect Eu:YSO crystal will be the overlapping profile of several ultra narrow spectra with identical resonant frequency as it shows in Fig. 1-2 left top. The estimated linewidth of the spectral hole can be as narrow as 122 Hz under certain conditions inferred from the reference [30].

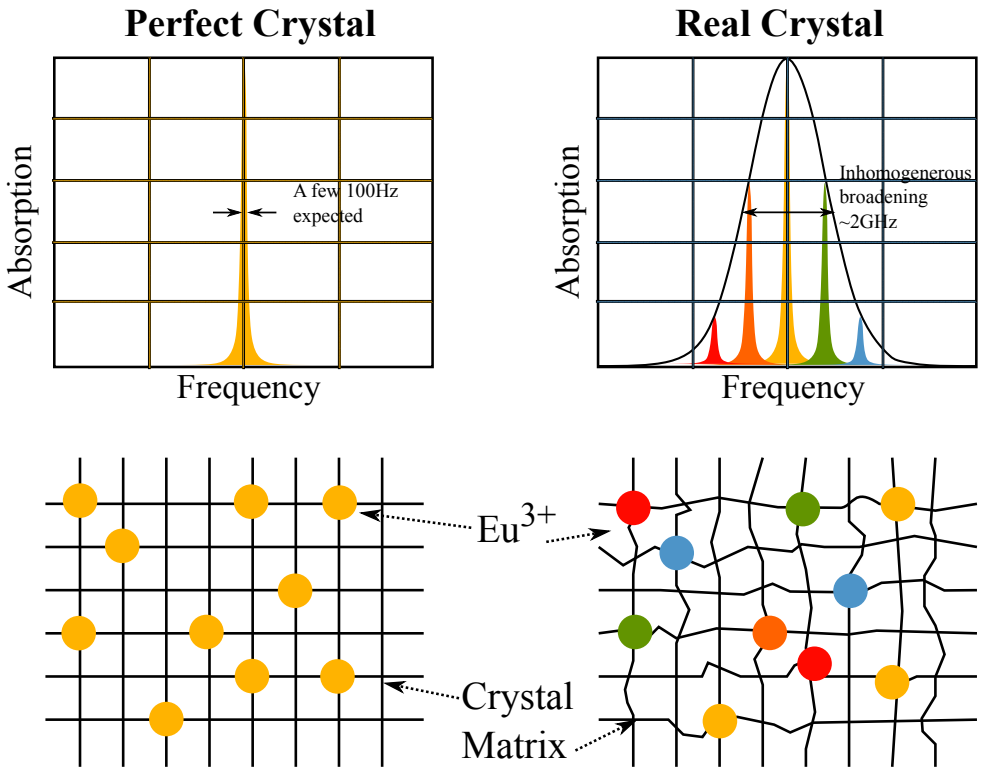

Figure 1-2: The diagram of Eu^{3+}:Y_2SiO_5 crystal matrix. The left top graph shows the absorption spectrum of Eu^{3+} ions in a perfect crystal where every individual ions have the same matrix environment as shown in the left bottom graph. The graphs on the right present the real situation where individual Eu^{3+} ions have different environment in the crystal matrix because of the randomness nature of doping (right bottom graph) and slight crystallographic mismatch between doping ion and substituted element. As a result, the absorption spectrum varies from location to location, making the overlapped spectrum have an inhomogeneously broadened linewidth of around 2 GHz (right top graph).

However, in the real case, because the europium ion is larger than the yttrium ion, subsequent to the doping of Eu^{3+} ions into the YSO host matrix, the crystal matrix is deformed in an irregular manner. Consequently, the resonant frequency of optical transition for each individual ions varies from location to location (see the dots in Fig. 1-2 right bottom). The absorption spectrum of the real crystal is therefore the envelop of these different absorption peaks in frequency coming from the ions with different crystal environments, making the whole crystal having an inhomogeneously broadened absorption spectrum, as the envelope curve shown in Fig. 1-2 top right. The linewdith of the inhomogeneously broadened absorption spectrum varies with the crystal substitution sites (see details in Sec. 1.2.3). The measured linewidth $\Gamma_{\text{Inhomogeneous}}$ for our 0.1% doped Eu:YSO crystal is 2.18 GHz for site 1 and 1.53 GHz for site 2 [38].

Creation of the Photo-imprinted Spectral Pattern

Once the crystal is pumped with a narrow-band laser, the inhomogeneously broadened absorption spectrum will be modified as a result of optical transition. The resulting transparent light to the crystal will act as a 'hole' in the absorption spectrum, forming the photo-imprinted spectral pattern shown in Fig. 1-3.

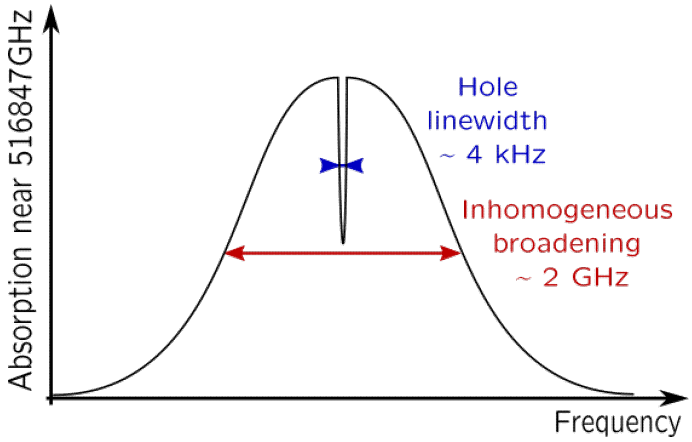

Figure 1-3: An illustration of a narrow photo-imprinted structure within the inhomogeneous absorption spectrum using the example of site 1.

The linewidth of the narrow spectral hole depends on the consistent behavior of

an ion ensemble. Therefore, the number of dopant ions will affect on the spectral hole linewidth. For our 0.1% doped Eu:YSO crystal, the typical width of spectral hole is around 4 kHz at Full Width of Half Maximum (FWHM). The possible effective factors of the hole linewidth includes the experimental parameters such as the burning power and time. Detailed discussions about the creation of the spectral hole will be expended in Sec. 1.4.1.

Moreover, we have observed that the crystal temperature affects the lifetime of the spectral hole [38]. Lower temperature allows to have longer life time of the spectral hole. When the crystal is below 4 K, the spectral hole's life time can be more than 10 hours. According to that, in our experiment, the crystal temperature is set below 4 K.

1.2.3 Eu^{3+}:Y_2SiO_5 Crystal Properties

The crystal used in our experiments is a 8 ×8 ×4 mm^3 quasi-parallelepiped. Yttrium orthosilicate belonging to the monoclinic system, it has 3 different crystallographic axes. The b axis, which coincides with the direction of propagation of the interrogation laser beam, is perpendicular to the other two axes (a and c) as shown in Fig. 1-4. Only the two faces which are perpendicular to the b axis are polished.

The Eu:YSO crystal has three principal dielectric axes names as D_1, D_2 and D_3, and they are perpendicular to each other. The D_3 axis is along the same direction as the b axis. As it is shown in Fig. 1-4, our crystal is cut along the dielectric axis making it convenient to identify the crystal axis in the experiment.

Substitution Sites of Eu^{3+} Ions

In the yttrium orthosilicate (Y_2SiO_5) crystal, there are two non-identical positions that yttrium ions are located in, which is named as site 1 and site 2 respectively. The surrounding ion number are 7 for site 1 and 6 for site 2 [39]. The vacuum wavelengths

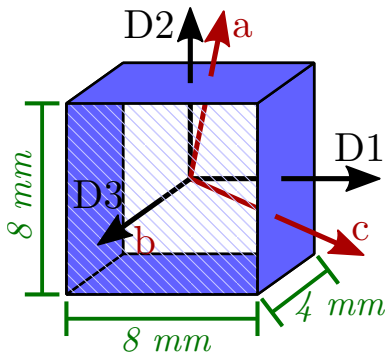

Figure 1-4: An illustration of the Eu^{3+}:Y_2SiO_5 crystal used on our experiment, with its physical dimensions, the dielectric axes D_1, D_2, D_3 and the crystalline axes a, b, c.

of Eu^{3+} ions for site 1 is 580.04 nm and 580.43 nm for site 2 (corresponding frequency is 516847.5 GHz for site 1 and 516696.2 GHz for site 2). When doped into the YSO crystal, the europium ions substitute the yttrium ions in these two substitution sites. In the investigation of spectral holes properties, the two sites are both considered.

1.3 Experimental Set-up

This section is to present the experimental set-up that we used in spectral hole burning experiment, including the propagation and processing of photoelectric signals, characterization of the stabilized frequency and spectral hole burning environments.

1.3.1 Optical Path Design

Figure 1-5 is a simplified schematic of our experimental set-up. Two commercial diode lasers at 1160 nm with the emitting power of 65 mW (Toptica DLPro) are used and referenced as master laser and slave laser. Both the master and slave lasers are frequency doubled through PPLN (Periodically Poled Lithium Niobate) wave-guides, arriving at 580 nm where the Eu^{3+}:Y_2SiO_5 material exhibits a ${}^7F_0 \rightarrow {}^5D_0$ transition of particular interest. Since the doubling process is not perfect, both of the two lasers can be separated by dichroic mirrors in order to have the infrared part and yellow

part in the use of optical path.

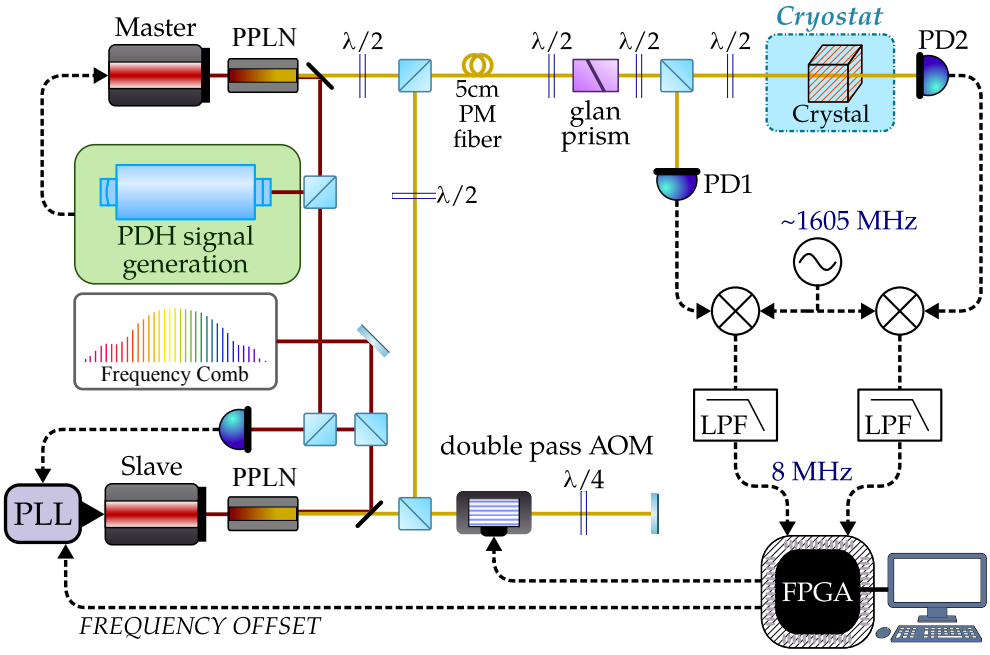

Figure 1-5: Schematic of experimental setup in spectral hole burning experiment with the crystal of Eu^{3+}:Y_2SiO_5 at cryogenic temperature.

Infrared Optical Path

In the infrared part, the master laser is frequency locked to a high finesse Fabry-Perot cavity through the PDH (Pound–Drever–Hall) technique, achieving a pre-stabilization. In order to quantify the laser frequency stability, a frequency comb which benefits from the accuracy of the primary frequency standards at SYRTE, is employed to measure the relative frequency change and absolute frequency values. The specific comb measurement for our laser is presented in Sec. 1.3.3.

Yellow Optical Path

In the yellow part of slave laser, a double pass Acousto-Optic Modulator (AOM) is used and driven by appropriate RF wave pattern. Therefore, an arbitrary spectral pattern with adjustable optical power can be created through the AOM according to the needs. Two types of arbitrary spectral patterns are used throughout this work. In the first type, one or more cw modes with fixed frequencies can be turned on

simultaneously at the required position in the optical spectrum. In the second type, a single optical mode with scanned frequency can be generated. This second type can be used, in particular to record a spectrum over a frequency range of a few hundreds of kHz in our experiments.

The master laser and slave laser are geometrically combined on a PBS (Polarizing Beam Splitter) in free space. For the purpose of getting cleaner spatial mode, a short fiber with 15 cm in length is used in the pass of master-slave beatnote propagation. The beam at the output of the short fiber, after collimating optics, goes through an adjustable diaphragm, which allows the beam size to be restricted further, followed by a $\lambda/2$ plate and a Glan polarizer for adjustable attenuation. A second $\lambda/2$ wave plate followed by a second Glan prism allows the beam to be split into two parts with controllable relative intensities. The utilization of Glan prisms instead of more standard (and somewhat easier to use) cube beam splitters was found to be important for best results in terms of measurement stability. This, we believe, comes from to their much reduced temperature-dependence, in terms of beam splitting ratio and output polarization.

Subsequent to the separation of the second Glan prism, half of the light (reference beam) goes directly to a photodiode (reference photodiode) and the other half (interrogation beam) goes through the Eu^{3+}:Y_2SiO_5 crystal located in the cryostat and collected by another identical photodiode (signal photodiode). The typical used photodiode in the measurements mentioned in this thesis is EOT-2030A, and the use of other photodiode will be specially marked. The comparison between the signal detected by these two photodiode provides direct information about the absorption of the crystal where a spectral hole pattern was previously imprinted (by comparison of the amplitudes of the signals). Furthermore, it also gives access to the dispersion properties of the crystal (by comparing the phases of the signal on the two photodiodes). This last information is particularly useful as it provides a convenient error signal which can be directly used for locking the probing laser to the spectral hole pattern.

Optical Pumping of Eu:YSO Crystal

Since both of the master laser and slave laser go through the crystal, to let the hole be burnt with less optical perturbation, the frequency of master laser is tuned outside or near the edge of the absorption spectrum of Eu^{3+} ions, while the slave laser is close to the maximum absorption of the ${}^7F_0 \rightarrow {}^5D_0$ transition in the Eu^{3+}:Y_2SiO_5 crystal. Therefore, in the experiment, only the slave laser is used for the spectral hole structure creation.

As there is a sufficient offset in frequency, the master laser has almost no effect on the spectral profile near the center of the absorption peak where the slave laser is. In this configuration, an error signal can be deduced based on the phase dispersion induced by the spectral hole on the two lasers. Such error signal can then be used to lock the slave laser frequency onto the spectral hole by experimentally monitoring the beatnote between the master laser and the slave laser. The obtained laser frequency stability is discussed in Sec. 1.4.

1.3.2 Digital Signal Processing

The beatnotes detected by the two photodiodes are then processed by a demodulation chain, including power amplification, frequency mixing and signal filtering. It is important to keep the various elements of the demodulation chain away from power saturation. One such example of saturation issue can be seen in Fig. 1-6 (a) for an un-optimized frequency chain. As a matter of fact, for operation with single RF beatnote (i.e. single mode in the interrogation laser), it may seem acceptable to partially saturate the RF frequency chain. However, as soon as one wants to explore multi-RF beatnote operations, such saturation will induce intermodulation tones between the modes through non-linearity, rendering the signal unsuitable for high precision measurement.

Subsequent to the replacement of the inappropriate devices, the problem of power

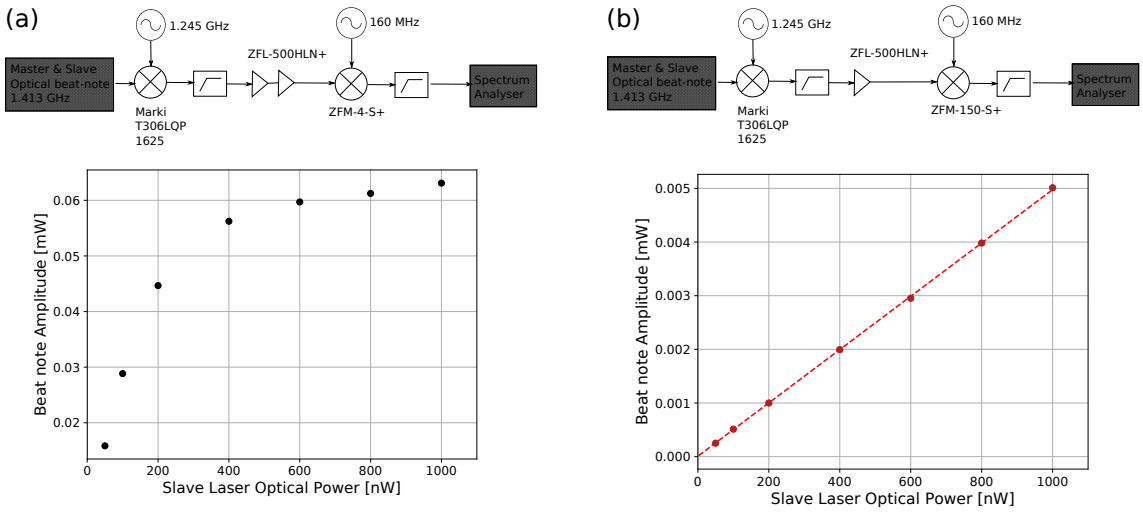

Figure 1-6: (a) The non-optimized demodulation chain previously used in our experiment (top graph), with which the signal had a power saturation problem as the bottom graph shows. The saturation test is done by changing the optical power of the detected signal (x-axis), which is the beatnote between master laser and slave laser, and then after the signal going through the elements in the top graph the beatnote is detected by a spectrum analyzer and the amplitude of the peak is noted then (y-axis). (b) Demodulation chain optimized to operate in the linear regime (top graph). In the bottom graph, the dashed line is the linear fit, which shows within the 1 μW optical power of slave laser, the power of the beatnote is in the linear regime.

saturation is solved. One example of the non-saturated curve is shown in Fig. 1-6 (b), where the power of the demodulated signal is in the expected linear regime. The final optimized demodulation chain is presented in Fig. 1-7, which shows after demodulation, the signal has a 8 MHz carrier frequency. The 8 MHz signal obtained after demodulation exhibits a signal to noise ratio above 70 dB with the resolution of 1 kHz.

The 8 MHz signal is then sent to a Ettus Research X310 platform, which comprises Analog to Digital Converters (ADC) (as well as Digital to Analog Converters - DAC - used to generated controlling signals for the experiment) and a Field-Programmable Gate Array (FPGA). After digitization in the reception channel, it is further demodulated to baseband by a Digital Down Conversion processing implemented in the FPGA, and then streamed *via* ethernet connection to a controlling computer, where the data is processed (on-the-fly) by a home-made program utilizing a Soft-

ware Defined Radio framework called GNU Radio. The signal processing program is composed of various tasks, making the signal to be filtered, functioned and transferred according to our need. Each task corresponds to a processing block in GNU Radio and the ensemble of blocks and their connections with each other form a "flowgraph" that determines the way our data treatment works. Software modifications of the flowgraph provides a convenient way to investigate different processing methods.

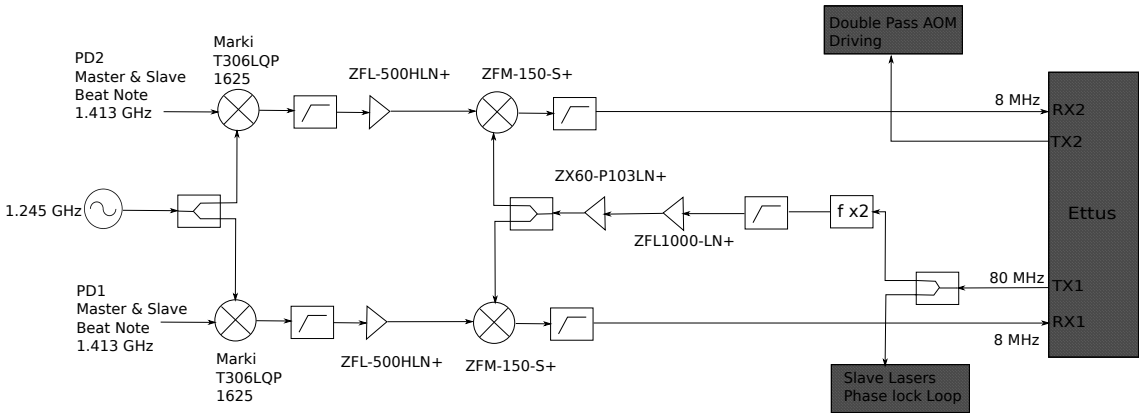

Figure 1-7: The diagram of the full demodulation chain used for processing signals detected by the two photodiodes to the RX input of the Ettus device. The usage of the electronic devices is to firstly filtering the spectrum and secondly mixing down the signal to the detectable frequency range and power range.

The SDR platform is a fully-digital system which is used for controlling the whole apparatus. It allows, firstly, the processing of the signals coming from the photodiode, based on which we can monitor the crystal's absorption and dispersion. Secondly, it allows the driving of the double pass AOM so that the arbitrary wave pattern can be created and sent through the crystal. Thirdly, it allows producing a correction to the optical frequency of the laser system that allows to keep the slave laser at resonance with the spectral hole.

1.3.3 Frequency Characterization Using an Optical Frequency Comb

Motivation

Since our laser is pre-stabilized by locking to the Fabry-Perot cavity, the drift of the cavity will have influence on the laser and can be seen as shift in spectral hole frequency. Even though the cavity drift is small, in order to perform a high precision measurement, the cavity induced laser frequency change needs to be removed. Therefore, an optical frequency comb, which is referenced to the primary clock providing high precision, is employed in our measurement.

Comb Measurement

A beatnote is realized between our laser and one tooth of the comb and counted by a frequency counter (K+K Messtechnik FXE). The comb measurement has a counting and recording rate of 1 Hz as the dot points presenting in Fig. 1-8.

De-drifting of the SHB Laser Frequency

With the intention of removing the cavity induced laser frequency drift, in the comb measurement, the desired information is the laser frequency change in time. So the counted beatnote frequency is then plotted as a function of time (see Fig. 1-8), and analyzed by a linear model to obtain the laser frequency drift over time. The linear fitting function is defined as

$$\Delta f = a \times \Delta t + b,$$

where Δf is the laser and comb counting teeth beatnote frequency variation, Δt is time in the unit of second, a is the desired linear slope of laser frequency drift and b is the frequency offset. Figure 1-8 is an example showing a drift slope around 0.04 Hz.s^{-1}. In all the measurements of electric field experiment, the cavity induced

laser frequency shift is less than 0.1 Hz.s^{-1} in absolute value. The sign of our laser frequency drift (increase or decrease) is verified by the comb team with methods allowing absolute frequency measurement.

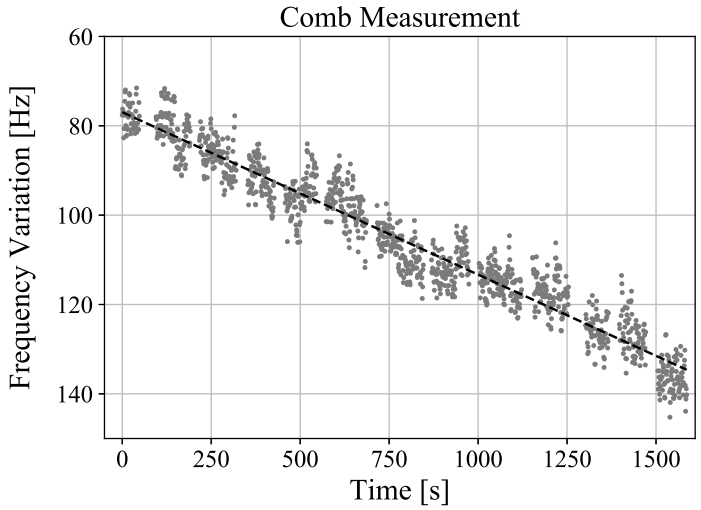

Figure 1-8: Comb measurement of the beatnote between the slave laser and one teeth of the comb. The gray points are the counted beatnote frequency variation. The black dash line is the linear fit of these points. This figure is one example showing the linear frequency drift coming from our reference cavity, and the linear slope from the fitting is -0.04 Hz.s^{-1} for the presented curve. The linear coefficient of the fit is then used in removing the cavity induced laser frequency drift in time.

In the measurements discussed in the following chapters, burning time t_{burn} and probing start time t_i are recorded for every scan. Considering the probing speed is 100 kHz.s^{-1} for a few hundreds hertz range scan, so the scan time for one spectrum is less than 10 seconds. In this case the cavity induced frequency shift will have negligible impact for peaks in the same spectrum (as measurements uncertainties are always larger than a hundred Hz). In each measurement consisting in scanning one spectrum, the scan start time can be used as the time reference for de-drift calculation. In this case, the laser frequency drift effect can be removed in the data treatment, in order to achieve the required high-precision measurements, which are presented in the following chapters.

1.3.4 Cryogenic Environment

The cryogenic environment allows the spectral hole has long life time, thus the spectral hole burning process are carried out around 4 K in our measurement. The commercial closed cycle (pulsed-tube) cryo cooler (Optidry 200 from MyCryofirm), makes it possible to cool down the Eu:YSO crystal with lower vibration noise compared with the other commercial devices (e.g. Cryostation from Montana Instruments). The science chamber consists of three layers. The outside vacuum chamber (OVC) is at room temperature, and is capable of supporting a high vacuum down to 10^{-9} mbar. The middle chamber, technically a thermal shield, is in thermal contact with the first cooling stage of the pulsed-tube, reaching about 50 K. The inner vacuum chamber (IVC), where the crystal is mounted, is in thermal contact via a $\sim$ 30 cm long copper plate with the second cooling stage of the pulse-tube, reaching around 4 K as it shown in Fig. 1-9.

Temperature Monitoring and Stabilization

Three temperature probes (Carbon Ceramic Sensors from Temati) are installed in the cryostat, giving access to the temperatures at three locations : next to the cold head of the first and second cooling stages of the pulsed tube, and at the base of the IVC. A heater (a 25 Ω resistor) is installed next to the IVC temperature probe, allowing for stabilization of the temperature using a commercial controller (Lakeshore 350). The typical temperature values reached by the cryo in free running is around 50 K, 3.2 K, and 3.8 K respectively. For the 4 K stage, the typical stability is about 10^{-4} K at 1 s, and the servo loop (typical time constant of about 10 s) removes long-term temperature drift but does not improve the stability at 1 s.

Crystal Temperature

Since the crystal is put on top of a cylindrical pedestal in copper and is in the thermal contact with the IVC, one would ideally need to stabilize the temperature read by the IVC probe. This is indeed the case for most of the experiments described

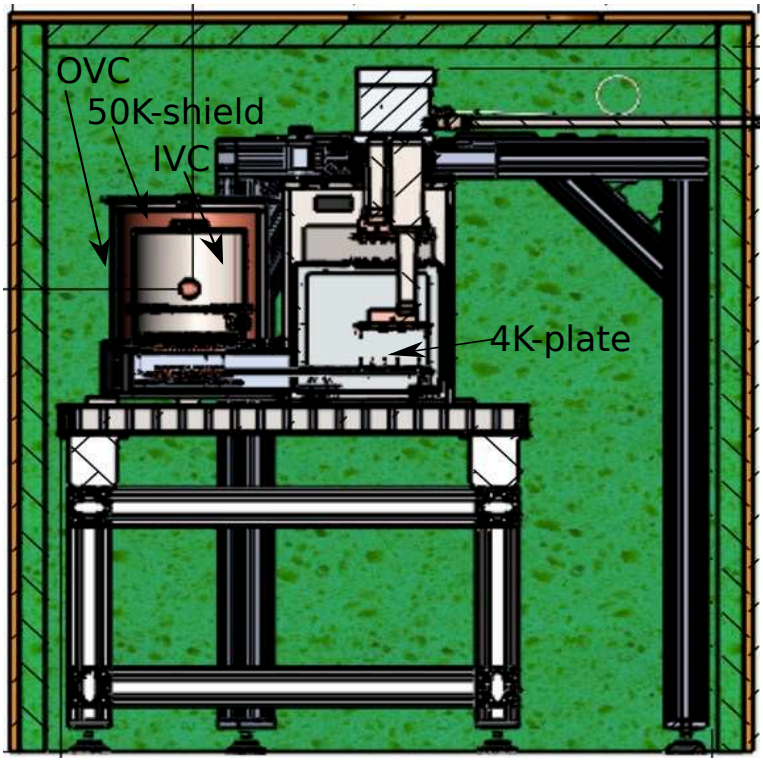

Figure 1-9: Schematic of our cryostat which has three chambers with decreased temperature, named as OVC, 50K-shield and IVC. In the meanwhile the cold plate can be thermalized around 4 K. The crystal is put inside the IVC chamber.

in this chapter. However, there were electrical contact issues on the IVC temperature probe during most part of 2019-2020, where most of the experiments described in Ch. 2 and Ch. 3. The temperature measured by the probe next to the 4 K cold head was then used for stabilization. The contact issues were fixed in August 2020, allowing for reliable measurement of the temperature next to the IVC and its stabilization since then.

1.4 Spectral Hole Burning For Ultra-stable Lasers

This section is to present the application of spectral hole burning technique in ultra-stable lasers in the Eu:YSO system. The spectral hole profile will be affected by the experimental parameters such as the burning time and power and probing time and

power, so the related parameters are discussed here. The detection scheme is also presented in this section which allows us to record the spectral profile and deduce the error signal of laser frequency locking. Our laser is finally frequency locked to the narrow spectral pattern and has its resulting frequency stability characterized, showing an improvement compared to the case where no stabilization to the spectral hole pattern is done.

1.4.1 Burning and Probing the Spectral Hole

As mentioned before, only the slave laser is used for burning or probing spectral holes, while the master laser keeps constant (and mostly away from the absorption spectrum) during the operation. So the power of the slave laser will directly affect the spectral hole burning or probing process. Moreover, the duration of the application of the laser for the hole burning also has a direct effect on the hole transmittance.

Burning Process

The burning process of the narrow spectral hole can be achieved using one single frequency of slave laser, which can be frequency scanned thanks to the double pass AOM. Theoretically, by pumping the crystal with the slave laser, the ions that are resonant with this certain frequency will all be shelved in the dark states, making a narrow spectral hole pattern in the absorption spectrum. The burning parameters will directly affect the spectral hole shape, for instance the weak power or too short burning time will cause a weak signal to noise ratio of the hole. The typical used burning parameters are 53 μW.cm^{-2} for the power intensity and 0.5 s for the burning duration, resulting as a narrow spectral hole with the linewidth around 4 kHz at FWHM.

An example of the burning process is shown in the Fig. 1-10, which is obtained by recording the amplitude of the obtained signal continuously. The increasing transmission in Fig. 1-10 is an indication of the shelved ion number, based on which we

can know how much the crystal is transparent to the light with employed burning frequency. The typical burning to the end process will show the transmission curve arrives at a constant value. However, in realistic experiment, because all the probing operation of the hole is also a ions pumping process, in order to avoid over burning of the spectral hole, the initial holes in our experiment are not burnt to the end (see Fig. 1-10).

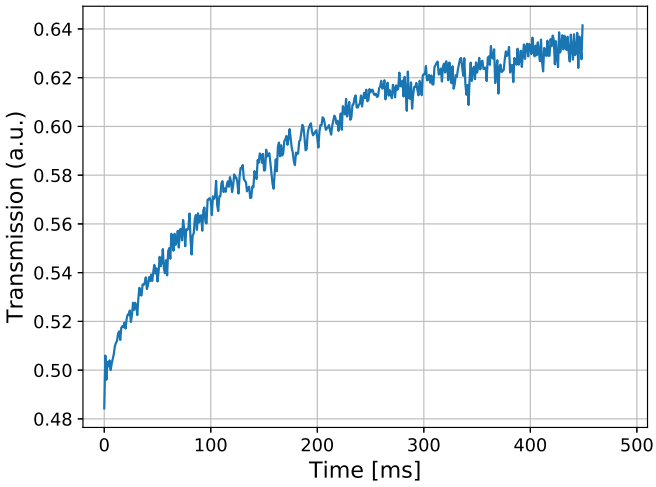

Figure 1-10: An example of the burning process showing the transmission as a function of burning time. For the presented curve, the burning parameters are 53 μW.cm^{-2} (15 μW beam with the diameter around 6 mm) for the optical power, and the burning duration is 450 ms.

In addition, the double pass AOM allows one mode (possibly frequency scanning) or multiple modes generation of slave laser. The scannable frequency can optically pump the ions resonant with a range of a frequency. As a result, it shows up as a square hole which has constant transmission for used scan range of frequency. The multiple modes generation make it possible to have multiple narrow holes imprinted in the absorption spectrum.

Probing the Spectral Hole

The spectral hole structure can be recorded by scanning the absorption spectrum of the crystal with the slave laser by controlling the double pass AOM which allows

a up to 1 MHz scan range in frequency. The typically used probe or scan power is around 0.35 μW.cm^{-2} (optical beam with the power of 100 nW and the diameter of 6 mm) for a single mode probing . Moreover, for a fixed sampling rate, the scanning speed determines the amount of data recorded in a fixed period of time, therefore affecting the resolution of the spectrum. The typical used scanning speed in the results presented in this manuscript is 100 kHz.s^{-1}. This scanning speed was found to be a good compromise, allowing to reach a sufficient resolution of the hole structure (the resolution is improved for slow scans), and, at the same time, avoid the over-burning problem which arises when the laser is spending too much time at each frequency.

1.4.2 Locking the Laser to the Spectral Hole

Once the spectral hole pattern is burnt, we can lock the laser on the spectral hole. Since the typical phase profile for a narrow spectral hole is linear in the center region, the laser can be frequency locked to the center of the spectral hole by referencing to the zero-crossing of the phase data, which corresponds to the extremum of the peak's transmission .

The slope given by the dephasing of the probe laser across the spectral hole works as a discriminator which can convert the phase measurement into an information about the frequency offset between the probing laser and the center of the hole. The larger the discriminator's slope, the narrower (and/or deeper) the hole. Conversely, low discriminator's slope correspond to wide (and/or shallow) holes, less suitable for locking as they require higher locking gain and are more sensitive to technical noise.

The error signal in the servo loop comes from differential dephasing measured by the two photodiodes. Depending on the detection scheme, the error signal can be different based on how many modes are detected in the photodiode. The details are presented in the following section with more discussions. The constant equal

to zero error signal means that the laser frequency is locked on the center (peak transmission) of the hole. The fluctuation of the error signal in time reflects the stability and efficiency of the lock. Therefore, error signal analysis can tell us firstly the detection noise level, and secondly the locking performance.

Since the slave laser is locked onto the master laser with a tunable frequency offset, one correction signal is obtained by tracking the offset frequency, so that the slave laser will be modified according to the hole locking feedback, forming a locking servo loop. Once the laser is locked to the spectral hole, the correction signal will give the information of frequency drifting with time, and the laser frequency value can be simultaneously measured by the optical frequency comb.

1.4.3 Differential Heterodyne Detection Scheme

The detection method is an important part in the establishment of ultra-stable laser, because the detection noise gives the technical lower limit of achievable laser frequency stability. On our experiment, since the probe laser power is limited, we use a master laser as the optical local oscillator for heterodyne detection. The first try with only signal photodiode shows a high detection noise as it presented in Fig. 1-11. Therefore, a differential measurement is carried out by adding a reference photodiode as the simplified setup in Fig. 1-12.

Two photodiodes (signal photodiode PD2 and reference photodiode PD1) used in the experiment can help to perform a differential measurement in order to eliminate various noise. We firstly tried with single heterodyne detection method, followed with the more optimized double heterodyne detection method. The details are discussed in the following section. The results presented here is the pure detection noise, which means that the optical beam is directly detected by the photodiode without going through the cryostat as it shown in Fig. 1-12. The detection noise with cryostat and crystal, will add extra parasitic Fabry-Perot noise, resulting a 2 to 3 times higher

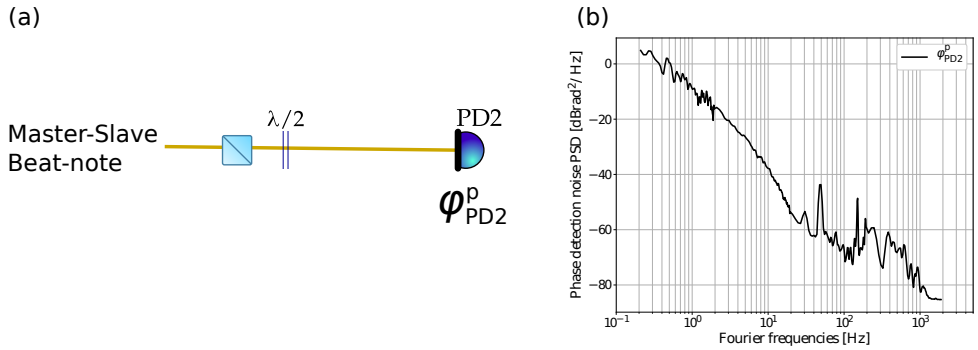

Figure 1-11: (a) The diagram of the single mode and single photodiode detection. The optical beam is not going through the crystal. (b), The corresponding pure detection noise which has high noise for both high Fourier frequency and low Fourier frequency. In all that follows, we consider the discriminator as 0.18 mrad.Hz^{-1} (typical value for a spectral hole of FWHM of 4 kHz) to convert the phase data into frequency data.

than the pure detection noise as seen later in the discussion of multi-hole detection in Sec. 1.5.3

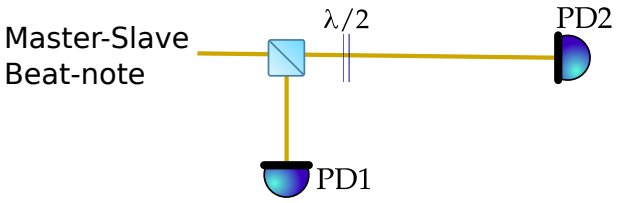

Figure 1-12: The diagram of the heterodyne detection for pure detection noise measurement when there is no crystal and cryostat concerned.

Single Heterodyne Detection

The detection scheme is firstly built with single frequency mode emission for both slave laser and master laser, therefore there is only one beatnote between master laser and slave laser. So this method is named as 'single heterodyne detection'. The slave laser is positioned near the center of one narrow hole, while the master laser is put outside of the absorption spectrum as it shown in Fig. 1-13 (a).

By probing with the optical beam, the reference photodiode should record a signal with constant amplitude and phase, while the signal photodiode will be modified by the spectral hole structure. By dividing the amplitude of the signal detected from

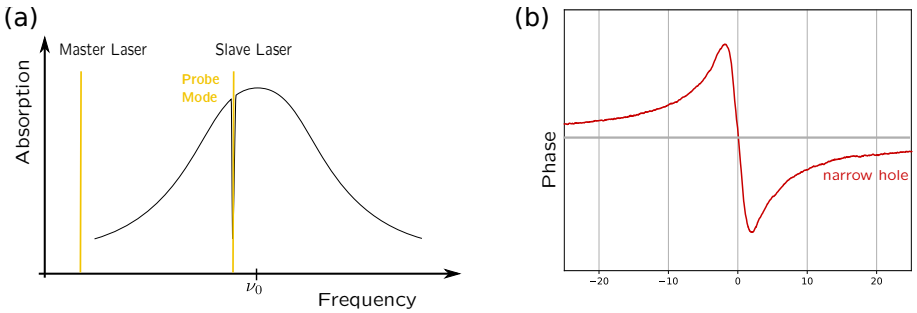

Figure 1-13: Single heterodyne detection. (a) the slave probe mode is used for probing the narrow hole, the master mode is probing the out position of the absorption spectrum. (b) the dispersion of the phase of the two modes probing.

the two photodiodes, one obtain the absorbtion spectrum of the crystal. By making the phase difference between the signals of the two photodiodes, one have access to the dispersion induced by the (spectral hole in the) crystal. The dephasing through a single narrow spectral hole is shown in Fig. 1-13 (b). Since it is linear and crosses zero at the center of the spectral hole, it can be used as an error signal for laser frequency stabilization.

The dispersion-based error signal can be derived from the two photodiodes. The Eq. 1.4.1 shows the mathematical method to get the error signal $\phi^{\text{Single}}_{\text{Error}}$, where $\phi^{\text{p}}_{\text{PD2}}$ is the phase data from the signal photodiode and $\phi^{\text{p}}_{\text{PD1}}$ is the phase data from the reference photodiode. The error signal $\phi^{\text{Single}}_{\text{Error}}$ is then used in the frequency locking of the laser, and the details of the stability will be presented in the Sec. 1.5.

$$\phi^{\text{Single}}_{\text{Error}} = \phi^{\text{p}}_{\text{PD2}} - \phi^{\text{p}}_{\text{PD1}} \,, \tag{1.4.1}$$

The detection noise based on the single heterodyne detection is shown in Fig. 1-14 (a), showing the detection noise by dividing the signal from two photodiodes. The projected laser frequency stability is also deduced by considering the phase discriminator as 0.18 mrad.Hz^{-1}, which is the typical value of the spectral hole in our measurement. The corresponding stability curve is shown in Fig. 1-14 (b), which is above our perspective level at short time scale.

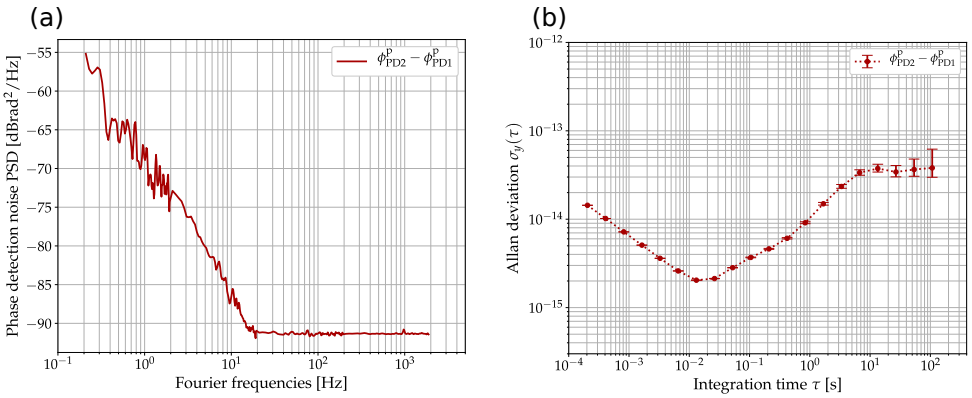

Figure 1-14: (a) the single heterodyne detection noise and (b) the projected laser frequency stability (discriminator = 0.18 mrad.Hz^{-1}).

Double Heterodyne Detection

Based on the results in Fig. 1-14, with the single heterodyne detection scheme, we found the detection noise limits the final obtained frequency stability of the laser. Therefore, a novel detection method is investigated by adding one more mode of slave laser, making the detected beatnote between master and slave laser becomes two for both photodiodes, which is then called 'double heterodyne detection'. The two modes of slave laser are named as probe mode and monitor mode respectively, as it shown in Fig. 1-15 (a). The probe mode is used to burn and probe the narrow hole, which is the same as single heterodyne detection method. The monitor mode of the slave laser is frequency positioned in the middle of a large square hole. The digital data treatment technique for generating a double mode on the slave laser was described previously in [34, 38], it will be described briefly in Sec. 1.5.2.

The heterodyne detection allows us to remove the systematic noise generated before the beam splitter as it shown in Fig. 1-5. While in the arm of beam propagation through the crystal, there is still some parasitic noise (etalon effect for example) coming from the cryostat. The monitor mode of slave laser is made for removing this kind of parasitic noise. So the monitor mode is used to probe a flat square hole, which is supposed to have a constant amplitude. The curves in Fig. 1-15 (b) shows the dephasing of the narrow hole and the square hole, in which the square hole is

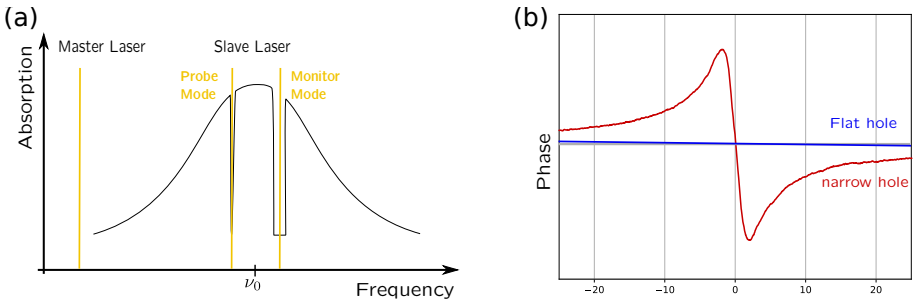

Figure 1-15: Double heterodyne detection. (a) one of the slave probe mode is used for probing the narrow hole and the other is probing the square hole. (b) red curve is the dispersion phase between the narrow hole structure and master laser probed structure. The blue curve is the dispersion phase between the flat hole structure and master laser probed structure, which could help to remove more parasitic noise in the system.

expected to have very small value in dispersion. By subtracting the noise referenced by the square hole, some parasitic noise (which is largely common mode between the probe and monitor mode) can be removed accordingly.

Therefore the error signal becomes like the Eq. 1.4.2, where $\phi^{\mathrm{p}}_{\mathrm{PD2}}$ and $\phi^{\mathrm{p}}_{\mathrm{PD1}}$ are the probe mode phase data of signal photodiode and reference photodiode respectively, and $\phi^{\mathrm{m}}_{\mathrm{PD2}}$ and $\phi^{\mathrm{m}}_{\mathrm{PD1}}$ are the monitor mode phase data from the two photodiodes.

$$\phi^{\mathrm{Double}}_{\mathrm{Error}} = (\phi^{\mathrm{p}}_{\mathrm{PD2}} - \phi^{\mathrm{p}}_{\mathrm{PD1}}) - (\phi^{\mathrm{m}}_{\mathrm{PD2}} - \phi^{\mathrm{m}}_{\mathrm{PD1}}) \tag{1.4.2}$$

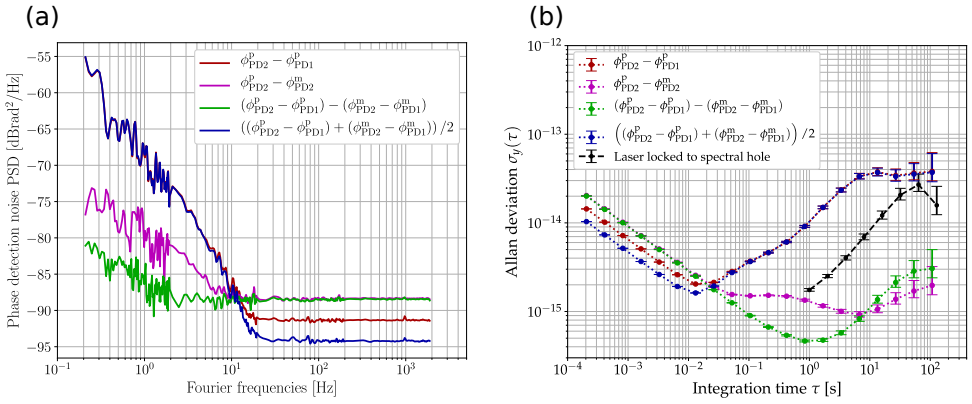

Figure 1-16: (a) Detection noise with different detection method. (b) Projected laser frequency stability corresponding to the detection method.

The one photodiode two modes detection is also shown in the curve labeled as $\phi^{\mathrm{p}}_{\mathrm{PD2}} - \phi^{\mathrm{m}}_{\mathrm{PD2}}$ (see Fig. 1-16), in which the white phase noise in high Fourier frequency is about 3 dB higher than the single heterodyne (two photodiodes one mode) detection.

The detection noise is a combination of additive noise at high Fourier frequencies and multiplicative noise at low Fourier frequencies as is presented in Fig. 1-16 (a). Comparing with the single heterodyne detection, the double heterodyne detection noise has lower multiplicative noise, while the additive noise is a bit higher (around 3 dB). The calculated laser frequency stability by converting the phase data into frequency taking the coefficient as 0.18 mrad.Hz^{-1} shows the upper limit of the stability level that could be obtained in the system, and the corresponding projected frequency stability level is shown in Fig. 1-16 (b). The double heterodyne detection gives the deduced stability level below 5 $\times 10^{-16}$ with 1 s interrogation time.

Since we focus on the frequency stability at around 1 s, the double heterodyne detection scheme is tested in the laser frequency stabilization by locking to the holes. The final obtained laser frequency stability, as the black curve shown in Fig. 1-16 (b). So the detection noise is not a limiting factor then.

Simulation of Multiple Narrow Holes

The double heterodyne detection described above, where the phase of a monitor mode is subtracted from that of a probe mode had slightly higher noise level at high Fourier frequency than the single heterodyne detection. It is interesting, however, to see what would happen if instead of subtracting the phases, one would add them together. The rationale for that is to see how the detection noise would behave if, instead of probing 1 narrow hole (single heterodyne) or 1 narrow and 1 large holes (double heterodyne with substraction), one would probe 2 narrow holes of which the error signals are combined (double heterodyne with addition). The blue curve in Fig. 1-16 (a) shows the simulation result of such a scenario. The result confirms that more narrow holes will make the white phase noise become lower (and the low Fourier frequency noise is unchanged compared to single heterodyne), giving us confidence

that increasing the number of narrow holes to probed in parrallel simultaneously is a valid approach to further reduce the detection noise at high Fourier frequencies. The corresponding work is expended in Sec. 1.5.3.

1.5 Optimization of the Laser Frequency Stability

Based on the results above (in Sec. 1.4.3), subsequent to the optimization in detection scheme with double heterodyne, the limiting factors for achieving an ultra-stable laser with higher level of frequency stability are the environmental conditions such as the temperature. The optimized experimental conditions will be helpful to get a narrower linewidth of the spectral hole and let the spectral hole be insensitive to external disturbances, therefore contributing to the optimization of laser frequency stability when lock onto the spectral hole. Once it resolved the next limiting factor will be the detection noise. Our work about the optimization of laser frequency stability is carried out in this direction.

1.5.1 Temperature and Pressure Coupled Environment

The temperature fluctuations of the crystal will turn into frequency fluctuations of the center of the spectral holes. They will therrfore degrade the frequency stability of a laser locked to a spectral hole pattern. As mentioned before, our crystal is put in a cold chamber and mounted onto a pedestal, making the temperature of crystal depends on the temperature of the cryostat. In order to check if the temperature is a limiting factor, our study starts with the thermal sensitivity of the spectral hole. After the experimental measurement and theoretical calculation, a new setup is then employed to get a system insensitive at first order, by using an environment where temperature and pressure effect on the spectral hole cancel each other.

Thermal Sensitivity of the Spectral Hole

In Eu^{3+}:Y_2SiO_5 system, the spectral hole temperature sensitivity can be analyzed by a model of $\delta f_T \propto T^4$ [40], where δf is the temperature caused spectral hole frequency shift and T stands for the absolute temperature of the crystal. The reported temperature sensitivity is 166 Hz.K^{-4} for site 1 and 313 Hz.K^{-4} for site 2, which give a point of comparison for our measurement.

With our set-up described in Sec. 1.3, it has been observed that the spectral hole will have a frequency shift when the temperature is changed. The thermal sensitivity of the spectral hole is then measured when the crystal is under vacuum. By changing the temperature set point in the servo loop of temperature stabilization, the temperature for the vacuum chambers and cold plate will be modified, so the crystal temperature will changes accordingly. Figure 1-17(a) shows an example of the change of spectral hole frequency caused by such step-wise change of temperature setting, where the laser is locked onto a 4 kHz wide spectral hole, and the change of the laser frequency is monitored by the frequency comb. The data points in Fig. 1-17 (a) is reported with a sample rate of 1 Hz, based on which the frequency variation could be measured and time constant for getting to the thermalized state can be deduced through a exponential model ($\delta f = A \exp[-t/\tau] + \text{offset}$). Typical data sets yield a time constant $\tau \sim 7$ s, which is consistent with that shown by the temperature probes. The data, however, often indicate a second, slower time scale, shown by the discrepancy between data and fit model between $t = 5$ s and $t = 40$ s, possibly coming from the mechanical relaxation of the silver lacquer that is used for fixation with good thermal contact, but adds a strain-induced frequency shift, which varies more slowly than the temperature variation.

The initial spectral hole is burnt with temperature T_0, providing a reference spectrum. By increasing the temperature up to T_i, the spectral hole will have a positive frequency shift. Typically, for a temperature difference ($\delta T = T_i - T_0$) of 2 K, a waiting time of two minutes is needed for the hole to reach the steady state (the frequency position no longer moves). After this waiting time, the spectral hole frequency shift δf_T can be measured with respect to the temperature change δT.

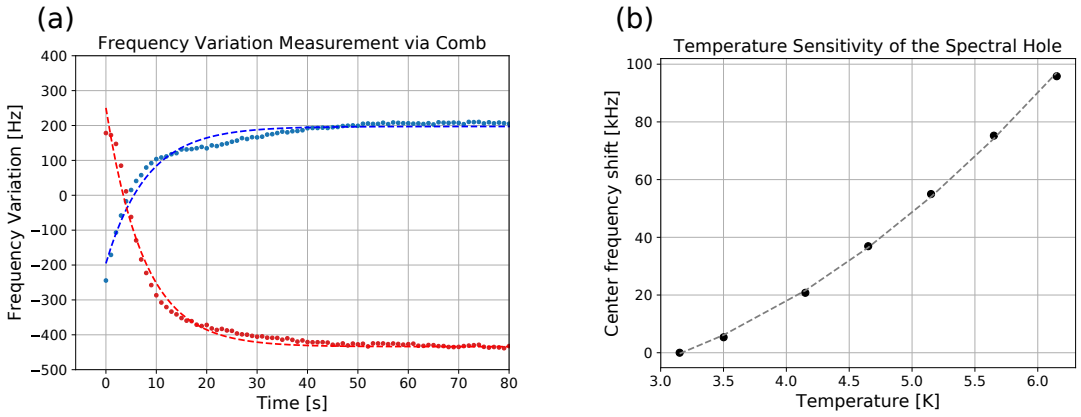

Figure 1-17: The spectral hole thermal sensitivity of site 1 when the crystal is in a vacuum chamber with the stabilized temperature at 3.2 K. The crystal is attached to a cold copper plate using silver lacquer. In (a), the data points are the frequency variation of our laser which is locked onto the hole. When the temperature is changed, the spectral hole has a frequency shift making the laser frequency change. The dashed curve is the fitting exponential model. In (b), the data point presents the measured frequency shift of the spectral hole at steady state when the temperature is changed and stabilized. The dashed line is the fitting of the data with a quadratic model.

The Fig. 1-17 (b) is the measured spectral hole center frequency shift as a function of temperature change. For the crystal in a vacuum chamber, the measured thermal sensitivity is 9.08 kHz.K^{-1} at 3.2 K. In previous work at NIST [41], the authors reported a temperature sensitivity of 10 kHz.K^{-1} at 3.2 K, which is close to our own measurement.

With the measured temperature sensitivity, a laser frequency stability of the order of 10^{-15} in fractional frequency requires a temperature stability of 6 $\times 10^{-5}$ K, which is in any case very demanding for our cryogenic system shown in Fig. 1-5. The following work is to find a way to minimize the thermal sensitivity of the spectral holes.

Temperature and Pressure Coupled Environment

It is known that isotropic pressure will affect the spectral hole's behavior and cause a frequency shift depending on the pressure [41]. Building upon that, a temperature insensitive environment can be achieved by coupling the isotropic pressure effect and the temperature effect on the spectral hole, forming a compensation of those two,

therefore the average effect on the spectral hole could be minimized.

Since the original IVC could only act as a 4 K shield but has never been hermetic to Helium gas at cryogenic temperature, it was replaced, at the beginning of 2021, with a smaller chamber, which is a cylindrical cell with the diameter of 52 mm and height of 10 cm as the photo is Fig. 1-18 (a), with which we are now able to use cold Helium gas to apply an isotropic pressure on the crystal as it shown in Fig. 1-18 (b).

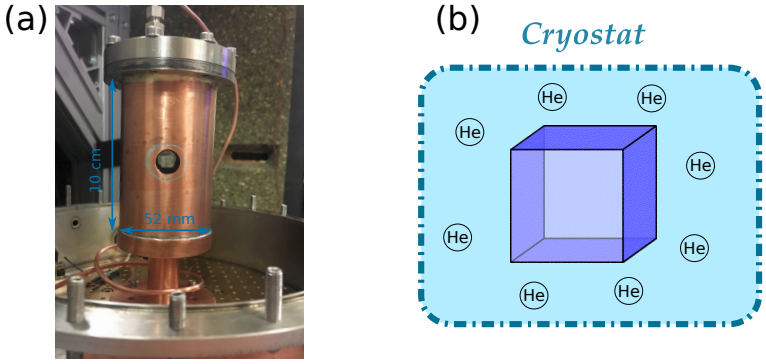

Figure 1-18: The IVC chamber for achieving the temperature and pressure coupled environment. The photo of the IVC cell is shown in (a), in which there is a tube allowing the injection of helium gas, forming an isotropic pressure on the crystal. The diagram for showing the crystal environment with a surrounding helium gas is in (b).

On the top of this new IVC, there is a pipe connecting the inside of the cell and the outside of the cryostat, allowing the gas injection or vacuum pumping of the cell through two manual valves at room temperature.

Under usual operation conditions, both valves are closed so that the total amount of the injected helium gas (in number of moles) is constant. The total volume of the gas is also fixed by fairely rigid tubings and the IVC, though a temperature gradient persists between the valves at room temperature and the IVC at nearly 4 K. If the temperature set point (near 4 K) is changed, the gas pressure will be changed too, according to the ideal gas law, conserving the total amount of the helium gas. The pressure gauge, which is positioned close to the injection point at room temperature, gives an indication of the quantity of the gas inside the IVC, provided that the IVC is

kept at a given temperature and sufficient time is allowed to chill the newly injected gas and form a steady isotropic pressure on the crystal. We therefore take the pressure value when the IVC is thermalized at 3.4 K as a reference for the measurements with different amount of gas (see Fig. 1-19).

Note that the crystal is put on a plastic post (which is thermally isolating) inside the IVC, so the temperature of the crystal directly comes from the thermal radiation from the surrounding environment and the contact with the surrounding gas, and not through thermal contact with the pedestal.

In order to find the 'magic environment', we first pump the IVC down to vacuum, then input some helium gas into it, making an isotropic pressure P applied on the crystal. We then measure the frequency of the spectral hole at different temperature set point in order to obtain the thermal sensitivity with respect to this *initial* pressure P (at 3.4 K). During the measurement, we take enough waiting time to let the crystal thermalize. For a relative lower pressure, because the number of gas molecular is less causing the thermal transfer efficiency lower, the waiting time will be longer. Moreover, some verification scan have also been done to visualize the crystal temperature change through the behavior of spectral hole. In other words, if the hole get a fixed frequency position, that means the crystal temperature is stable at that time.

The spectral hole thermal sensitivity is measured with different gas pressure applied on the crystal at a reference temperature of 3.4 K. In Fig. 1-19, all the points with the same color show the measurement with the same amount of gas. It is observed that the spectral holes sensitivity will change the sign with different pressure applied, depending on whose influence is dominant (temperature or pressure), as the curves shown in Fig. 1-19. By balancing the effect of temperature and pressure on the spectral hole, we could find a effect compensated situation which is then called as 'magic environment'. The magic environment achieves the first order global cancellation by coupling those two effect. In the thermal sensitivity measurement shows in the dark red curve in Fig. 1-19, the magic shows up in the case where the slope of the

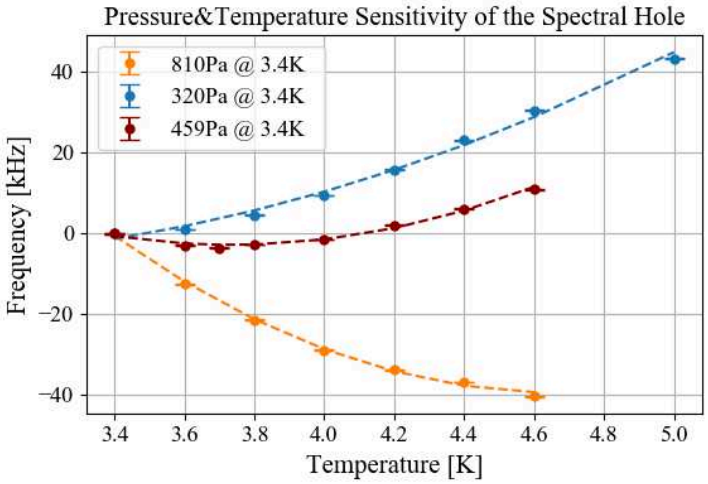

Figure 1-19: When the crystal is surrounded by the helium gas, the spectral hole thermal sensitivity is measured for different initial pressures. They are all modeled by a quadratic model shown in the dash lines. In the dark red curve, one of the magic environment can be found where the temperature and pressure effect on the spectral hole is compensated.

curve equals to zero, providing, one of the magic environment of 526 Pa at 3.7 K. The corresponding second order sensitivity is on the order of 20 kHz.K^{-2}, obtained from a quadratic fit model. This translates the typical temperature stability of 10^{-4} K at 1 s to a fractional frequency stability of 4×10^{-19}, well below noise from other sources currently identified on our experiment.

The spectral holes will benefits from the coupled environment and have a reduced sensitivity to the temperature fluctuations of the cryostat, which is hopefully helping the optimization of laser frequency stability. Alternatively, one could reduce the thermal sensitivity (which scales as T^4) by cooling the crystal down to dilution temperatures, thereby also reducing temperature induced frequency noise. This is planned on our experiment, with the cryostat being currently upgraded to include a dilution stage, but is beyond the scope of my PhD project and will not be discussed further.

1.5.2 Improvements on Digital Signal Generation and Processing

With the help of the magic environment for the spectral hole to be burnt, the next direction for the laser frequency stability to be improved is to further decrease the detection noise. Our work starts with improvement of the flowgraph, in which the different ways of signal processing are tested by modifying the arrangement and functions of data treatment blocks (as it discussed in Sec. 1.3.2). A strong specificity of the SHB experiment at SYRTE is that it explores the probing of multiple holes *simultaneously*. This is in stark contrast with previous work such as that presented in [28,41], where, although multiple holes are probed, the probing was in fact done consecutively making that the order of the holes being probed is done pseudo-randomly. We believe our approach may help identifying more easily technical limitations because it removes extra time constants and random process in the hoping from hole to hole, and hopefully allow reaching a lower detection noise.

Signal Generation

A first challenge, when addressing this subject of simultaneous probing of spectral holes, is related to the emission of a spectral pattern on the slave laser composed of several modes. Our approach is based on decomposing the spectrum in regularly spaced channels, where the digital control system allows turning on or off light with adjustable amplitude and phase in each of these channels following the test or application in mind.

Previous channelization was done using a Fast Fourier Transform (FFT) approach. An array of complex value, in which the value corresponds to amplitudes and phases and could be set dynamically in the control program, was considered to be representing the spectrum. An Inverse FFT (IFFT) was done to generate time samples from this spectral representation, which were up-converted by the Software Defined Radio (SDR) systems in the Ettus X310 device, to the carrier frequency (80 MHz)

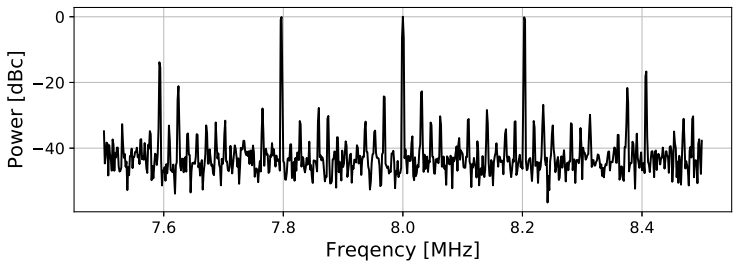

Figure 1-20: The spectrum to show the result of IFFT-based generation for 3 equally spaced modes (appearing at 7.8 MHz, 8 MHz, and 8.2 MHz on the spectrum). The control signal is applied to the double pass AOM controlling the slave laser. The beatnote between the master laser and the slave laser is photo-detected and demodulated down to a carrier frequency of 8 MHz before being observed on a spectrum analyzer. The desired three modes are surrounded with a forest peaks.

controlling the slave laser AOM, and the process was repeated continuously. This approach was found experimentally acceptable when working with one or two modes. However, when we tried to increase further the number of modes used simultaneously, many parasitic peaks were seen making the system not really usable (see Fig. 1-20). This is attributed to the fact that, in the most general case, there is no continuity between the time series of samples generated by an IFFT calculation and that generated by the next IFFT calculation. Extra interpolating and filtering would be necessary to obtain such time-continuity, which may become highly consuming in terms of computational-resources.

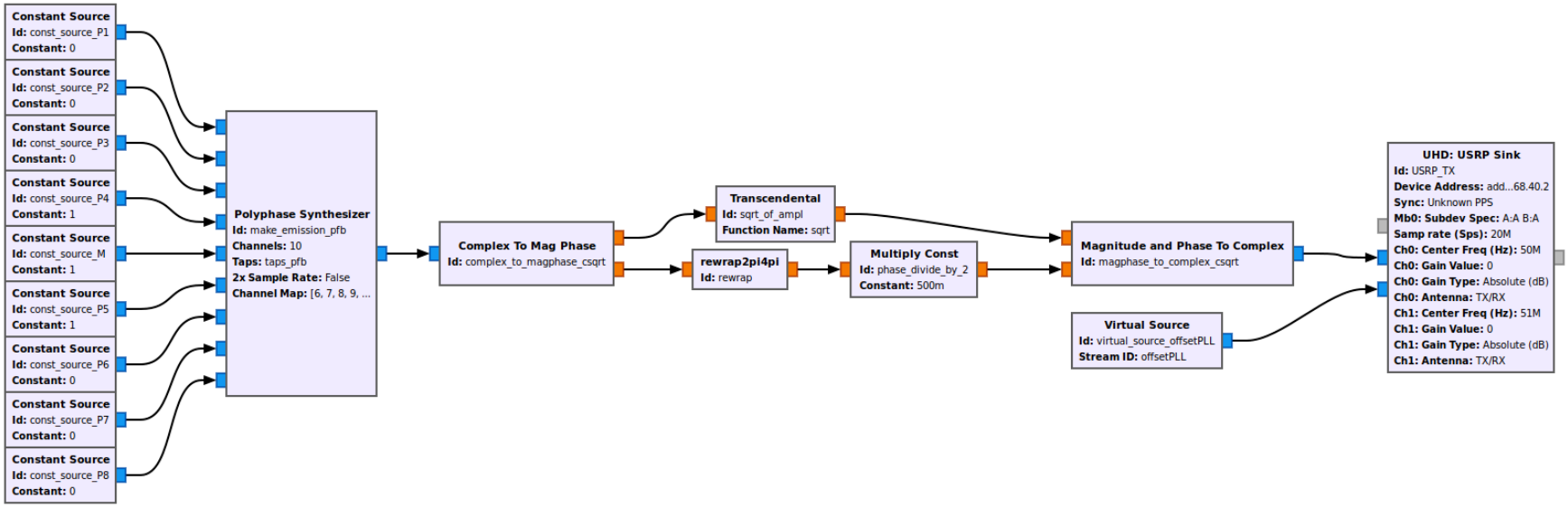

Figure 1-21: The flowgraph of signal generation and emission through the function of polyphase filter bank synthesizer block. This example flowgraph allows up to 10 modes to be emitted in 10 evenly spaced narrow-band channels. The "Constant Source" blocks generate a constant value data stream at the center of each of these narrow band channels. A value of zero effectively means that no light is emitted in this channel. The "Polyphase Synthesizer" combines these 10 narrow-band channels into 1 wide band channel (in practice, we operate at 2 Mega Sample per Second -MSPS- after the synthesizer). The following blocks are used to calculate on-the-fly the square-root of the complex values generated. The data stream is split between amplitude and phase ("Complex To Mag Phase" block). The square-root of the amplitude is taken ("Transcendental - Function name = sqrt"). The phase is rewrapped in the interval of $[-2\pi, 2\pi]$ ("rewrap2pi4pi" block) and divided by 2 ("Multiply Const - constant = 0.5"). Finally, the resulting modified amplitude and phase are recombined into a complex value ("Magnitude and Phase To Complex" block). The final "UHD:USRP Sink" block is responsible for controlling the hardware and generating the RF signal that drives the double-pass acousto-optic modulator. Note that this block has 2 inputs and, in fact, controls 2 RF signals. The second input/RF signal (simply shown as "Virtual Source" here) is used to control the offset frequency between the master and the slave laser, which can be constant, or real-time controlled when we lock the laser to the spectral hole burning pattern.

A better approach is to use a method known in the digital radio world as "polyphase filter bank" [42, 43] (see Fig. 1-21), which is implemented in "gr-filter" library of the GNURadio framework. This method uses a computationally efficient algorithm, which is based on a IFFT combined with under sampling of a finite impulse response low-pass filter, to combine several narrow-band streams of data into a single wide-band and phase-continuous stream where each narrow-band input stream is shifted to a given and regularly spaced spectral channel of the output stream. This function is called "polyphase filter bank synthesizer block" in the GnuRadio framework. In practice, for our application where we only want CW modes on or off in each of the channels, the narrow-band signals are only composed of constant values (possibly zero for the relevant mode being off). We have successfully used this approach to generate much cleaner multi-mode spectra than with the previous IFFT-only approach (see Fig. 1-22).

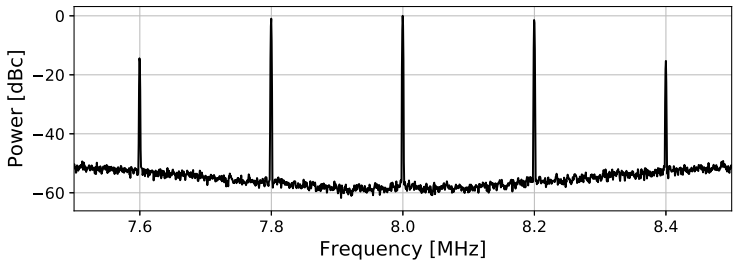

Figure 1-22: The spectrum of the polyphase filter bank - based generation, with an example of three-mode generation. The control signal is applied to the AOM controlling the slave laser. The beatnote between the master laser and the slave laser is photo-detected and demodulated down to a carrier frequency of 8 MHz before being observed on a spectrum analyzer. The three desired modes are the peaks at 7.8 MHz, 8 MHz, and 8.2 MHz, showing the cleaner spectrum that can be obtained via the IFFT-based generation method.

A further challenge comes from our implementation the slave-laser-controlling Acousto-Optic Modulator (AOM) in a double-pass configuration. This comes from the fact that we want to drive it with several different frequencies, over a relatively large spectral range (1 MHz or more), and an acousto-optic modulator is well-known to not only shift the frequency of the incoming beam by an offset related to the

driving radio frequency signal, but also to deflect it by an angle that depends on the radio frequency as well. Such geometrical effects would induce frequency-dependent inhomogeneities in the illumination of the crystal, which we wish to avoid. In the double-pass configurations, these geometric effect are canceled.

However, when driving a double-pass AOM with more than one carrier RF frequency signal, a complication occurs through intermodulation between the different carriers involved. In fact, the RF waveform that is required by the double pass AOM in order to obtain the desired optical waveform is *not* the simple sum of the CW signals which would produce each spectral components. This can be seen mathhematically when writing in appropriate form the effect of a double-pass AOM on an optical field. Given a CW input laser field $A_{\text{opt}} \exp[i2\pi\nu_0 t]$, we obtain, after experiencing twice a diffraction in the first order, a field

$$A_{\text{opt}} \exp[i2\pi\nu_0 t] \cdot \exp[i2\pi f_0 t] \cdot A_{\text{RF}}^2(t) \exp[i2\pi \cdot 2\phi_{\text{RF}}(t)],$$

where the driving RF field has the shape $A_{\text{RF}}(t) \exp[i2\pi\phi_{\text{RF}}(t)] \cdot \exp[i2\pi f_0 t]$, composed of an amplitude ($A_{\text{RF}}(t)$) and phase ($\phi_{\text{RF}}(t)$) modulated signal around a carrier whose frequency is f_0. Note that this simple expression requires the AOM to operate in its *linear regime*, which is in fact pretty unusual, as, most often, AOMs are driven with an RF power intended for *maximal diffraction efficiency*, which corresponds to a saturation point substantially above the linear regime. Since we need only a very low optical power for probing the spectral holes, and we have several mW of optical power available at 580 nm for the slave laser, we can, however, stay in the linear regime with low diffraction efficiency, and still have enough optical power for our application.

As can be seen, the double-pass AOM has an effect on the spectrum that scales as the *square* of the modulating field $A_{\text{RF}}(t) \exp[i2\pi \cdot \phi_{\text{RF}}(t)]$. This implies that RF fields composed of several spectral modes will be subject to very strong intermodulation effects. This observation, however, reveals a method to suppress this intermodulation: if, prior to generating the physical RF field which drives the AOM, we take the *square*

root of the digital samples, the squaring effect of the double pass AOM will be exactly canceled [44, 45]. Note that we need here to use a complex-number implementation of the square root function. To do that, we have chosen to decompose a (complex number) input sample in its amplitude and phase, divide the phase by 2, take the (real number) square root of the amplitude, and finally recombine the resulting values to obtain the complex-square-root of the input sample. This approach was successfully implemented in previous work in the SHB team at SYRTE [34, 38].

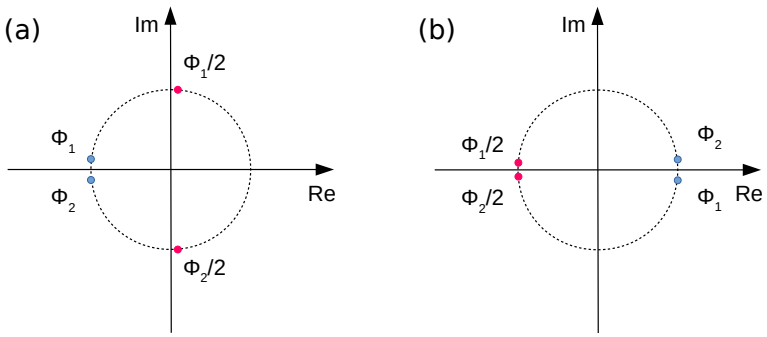

Figure 1-23: Phase samples in the complex plane. (a) Without the re-wrap function, an initially continuous signal with the phase crossing from $\phi_1 \sim \pi$ to $\phi_2 \sim -\pi$ will have a sudden jump after the square root function, since the phase is divided by 2. (b) After adding the re-wrap function, the phase crossing from $\phi_1 \sim 2\pi$ to $\phi_2 \sim -2\pi$ will remain continuous after the square root function.

However, with more complex spectral pattern being desired for experimentation, an extra subtlety appeared. The phase data in a digital system is typically wrapped in the range of $-\pi$ to π. This makes sense, because after digital to analog conversion there is no physical difference between a digital sample $A\exp[i\pi]$ and a digital sample $A\exp[-i\pi]$. However, in our data treatment, after passing through the complex square root function, the phase value will become half of the original one, which will be in the range $-\pi/2$ to $\pi/2$. In the complex plane, two successive samples $A\exp[i(\pi-\epsilon)]$ and $A\exp[i(\pi+\epsilon)] = A\exp[i(-\pi+\epsilon)]$, which are continuous in phase for very small ϵ, will therefore produce, after complex-square-rooting, two successive samples $A\exp[i(\pi/2-\epsilon/2)]$ and $A\exp[i(-\pi/2+\epsilon/2)]$. Although the squaring effect of the double pass AOM is canceled out, the physical signal produced will exhibit a *sudden jump in phase* at this point (except if the amplitude happen to

be exactly zero at that moment). See graph in Fig. 1-23 (a). In reality, the AOM acts as a low-pass filter, and this sudden phase jump cannot be realized perfectly well. The resulting optical spectrum will therefore exhibit parasitic peaks corresponding to this imperfection. See the purple plot in Fig. 1-24 for an example.

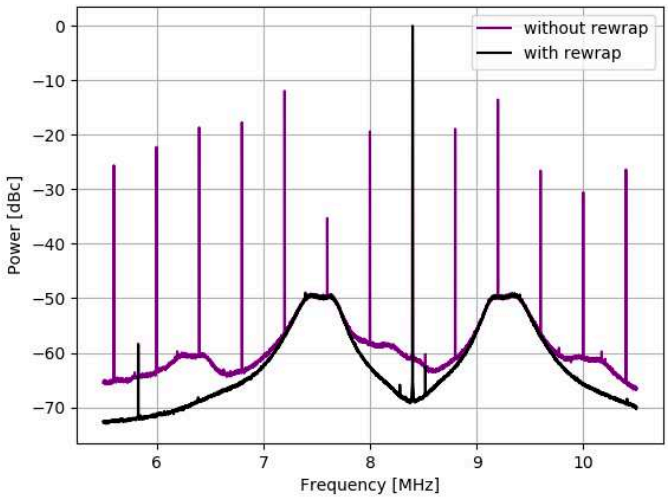

Figure 1-24: The spectrum of the slave laser light, with (black plot) and without (purple plot) using the re-wrap function, in the case of the generation of a single mode at a frequency offset from the carrier frequency. The control signal is applied to the AOM controlling the slave laser. The beatnote between the master laser and the slave laser is photo-detected and demodulated down to a carrier frequency of 8 MHz before being observed on a spectrum analyzer. The re-wrap function, together with the polyphase filter bank synthesizer generation helps getting a cleaner spectrum in the experiment.

To overcome this problem, a "phase re-wrap" function is added. Thanks to this function, the phase data wrapped in the $-\pi$ to π interval is re-wrapped in the range of -2π to 2π, prior to the division of the phase by two in the calculation of the complex square root. With this modification, the continuity of evolution of the phase samples in the complex plane is recovered, and sudden jumps of phase are avoided as it shown in Fig. 1-23 (b). This leads to cleaner spectra, in particular when trying to realize spectra which are not symmetric with reference to the central frequency (for spectra which are symmetric, the sudden jump in phase between $-\pi$ and π occurs when the

amplitude of the signal is close to zero, making this problem much less stringent). See Fig. 1-24 for an example.

Signal Reception and Error Signal Extraction

Similarly to the case of the signal emission, originally, the signal reception was using a simple FFT approach to isolate the different channels, extract the phase difference between the 2 photodiodes (before and after passing through the cryostat and the crystal) for the modes that were turned on (*i.e.* in which channels light was actually emitted by the signal generation part) and combine these information together to create an error signal appropriate for locking the slave laser on the spectral hole pattern. A standard windowing technique was used to minimize cross-talks between the channels in this approach. The input stream of data corresponding to each photodiode was segmented in successive chunks of samples. These chunks of samples, forming an array of successive data points, were multiplied by an apodization function (Hanning window) before being processed by a FFT algorithm. For both photodiodes, the array elements of the FFT data corresponding to channels for which light was generated by the signal generation part were extracted. For each relevant channel, the complex values obtained for the two photodiodes were divided, making the phase of the ratio extracted, and an error signal was then generated by appropriate combination of these phase data.

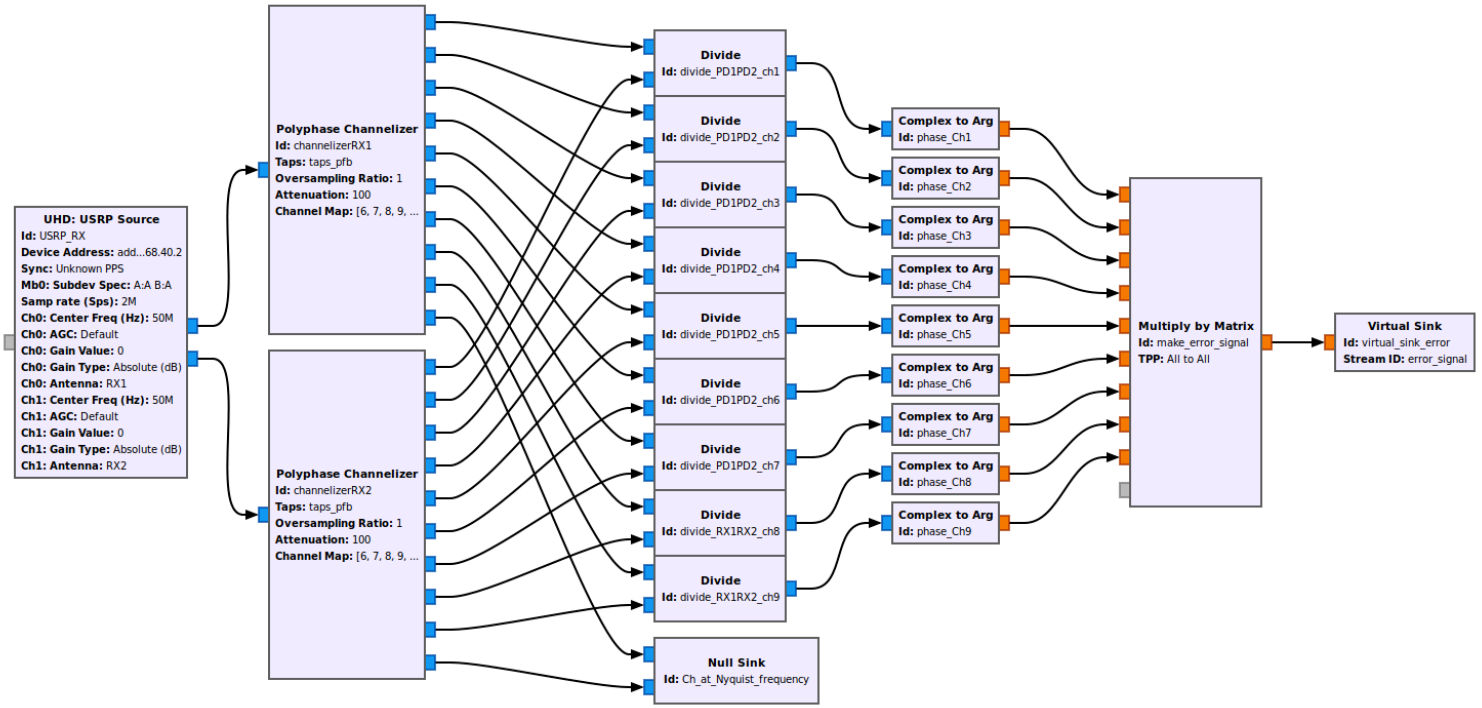

Figure 1-25: The signal reception part in the flowgraph, which uses the polyphase filter bank approach. The "UHD:USRP Source" Block is controlling the external hardware and provides the 2 streams of complex data coming from the two photodiodes before and after the crystal. The "Polyphase Channelizer" blocks split this wide band signal (we typically use a data rate of 20 Mega Sample per Second (MSPS) in 10 narrow-band signals (at 2 MSPS each) regularly spaced in the initial spectral range. In practice only 9 channels are used, the one corresponding to the Nyquist frequency is discarded ("Null Sink" block). The series of "Divide" blocks make a pair-wise division in each of these narrow-band channels of the samples coming from the two photodiodes, and the "Complex to Arg" blocks calculate the phase of these ratios, effectively realizing the phase difference, for every channels, of the beatnote detected in this channel by the two photodiodes. Finally, the "Multiply by Matrix" block realizes a programmable linear combination of these phase data (typically setting a coefficient 0 for channels where no mode is turned on, and a positive or negative value (depending on the detection regime being utilized) coefficient for the others. The "Virtual Sink" final block is just a place holder representing that the resulting error signal can subsequently used in a servo-loop process.

With the use of polyphase filter bank for emission, it also makes sense to use a similar approach for reception. As a matter of fact, in the line of the "polyphase filter bank synthesizer block", an other related function exists, called the "polyphase filter bank channelizer block" in the GnuRadio framework (see Fig. 1-25). This block does the reverse operation, *i.e.* take a wide-band stream of data and split it into several narrow-band streams, each centered on a regularly spaced spectral channel. Compared to the simpler FFT-based approach described above, this allows finer control of the filtering process that prevent cross-talk between channels, without much computational overhead, owing to the polyphase technique. We used this approach successfully for the multiple heterodyne detection study described in the next section.

As a conclusion, based on the modification of the flowgraph, including the utilization of the inverse FFT generation, re-wrap function, and also the polyphase filter bank blocks, we can first, get a cleaner spectrum with continuous phase samples, and second, generate multiple modes of slave laser paving the way of multiple heterodyne detection.

1.5.3 Multiple Heterodyne Detection

Depending on our simulation of two narrow hole detection (in Sec. 1.4.3) and the improvement of the digital signal processing flowgraph, the investigation of laser frequency stability follows with multiple holes detection, which is expected to further improve the detection noise, thus increase the stability level.

The detection noise presented in this section include both the pure detection noise as the diagram shown in Fig. 1-26 (a) when the light is directly detected by the photodiode without going through the crystal, and also the real detection noise as it shown in Fig. 1-26 (b) when the light goes through the cryostat and crystal adding parasitic Fabry-Perot effects in the system.

Triple Modes Generation

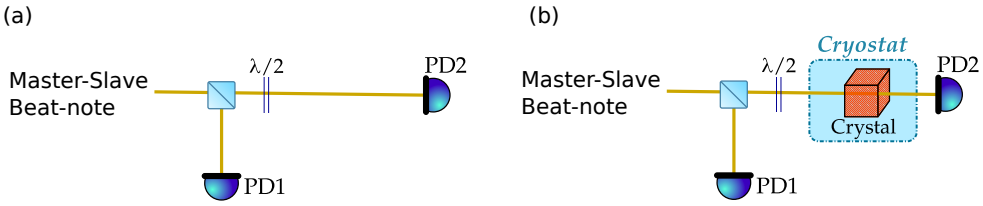

Figure 1-26: The diagram of the heterodyne detection for both pure detection noise measurement in (a) when there is no crystal nor cryostat concerned, and real detection noise measurement in (b) when the optical beam goes through the cryostat and the crystal.

Since the novel digital flowgraph allows the generation of multiple modes in slave laser, the first try of multiple heterodyne detection starts from triple modes detection (the spectrum in Fig. 1-22). The three modes of slave laser are separated by 200 kHz from each other, but with the same power. The error signal in the triple modes detection is shown in the Eq. 1.5.1, which assumes two probe modes (p1, p2) and one monitor mode (m) in the detection that are expected to get better signal to noise ratio.

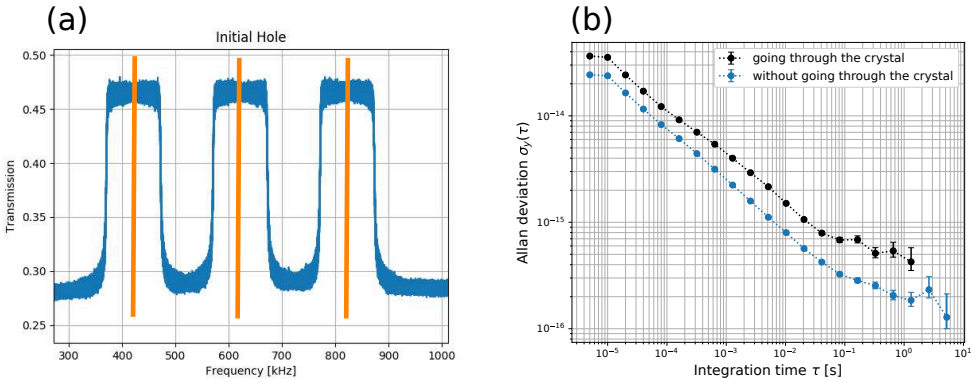

Figure 1-27: The detection method of three modes probing method. Three square holes are burnt as it shown in (a), in order to do the detection noise measurement by probing the structure with constant amplitude. (b) is the corresponding detection noise converted to the frequency stability by using the typical discriminator of 0.18 mrad.Hz^{-1}. The black curve is calculated with the data by probing the square holes when the optical beam going through the crystal, while the blue curve is the pure detection noise when the optical beam does not go into the cryostat meaning no holes burnt.

$$\phi_{\text{Error}}^{\text{Triple}} = [(\phi_{\text{PD2}}^{\text{p1}} + \phi_{\text{PD2}}^{\text{p2}})/2 - \phi_{\text{PD2}}^{\text{m}}] - [(\phi_{\text{PD1}}^{\text{p1}} + \phi_{\text{PD1}}^{\text{p2}})/2 - \phi_{\text{PD1}}^{\text{m}}] \tag{1.5.1}$$

To measure the detection noise with triple modes, three square holes are burned with 100 kHz width as it shown in Fig. 1-27 (a), which are supposed to have flat amplitude in structure thus small phase dispersion, therefore can be used for detection noise measurement. The employed setup is presented in Fig. 1-26 (b). By probing the center of those square holes burnt in the crystal, the obtained detection noise arrives at the level of 5 $\times 10^{-16}$ at 1 s as the black curve shown in Fig. 1-27 (b).

Moreover, to compare with the cryostat and crystal carried parasitic noise, another detection noise measurement is also done by putting the signal photodiode in front of cryostat, which means the optical beam does not go through the crystal or even the cryostat as the setup shown in Fig. 1-26 (a). The pure detection noise without the crystal is at the level of 2 $\times 10^{-16}$ at 1 s as the blue curve shown in Fig. 1-27 (b), which is better than our previous result [33] but is expected to be a further lower value.

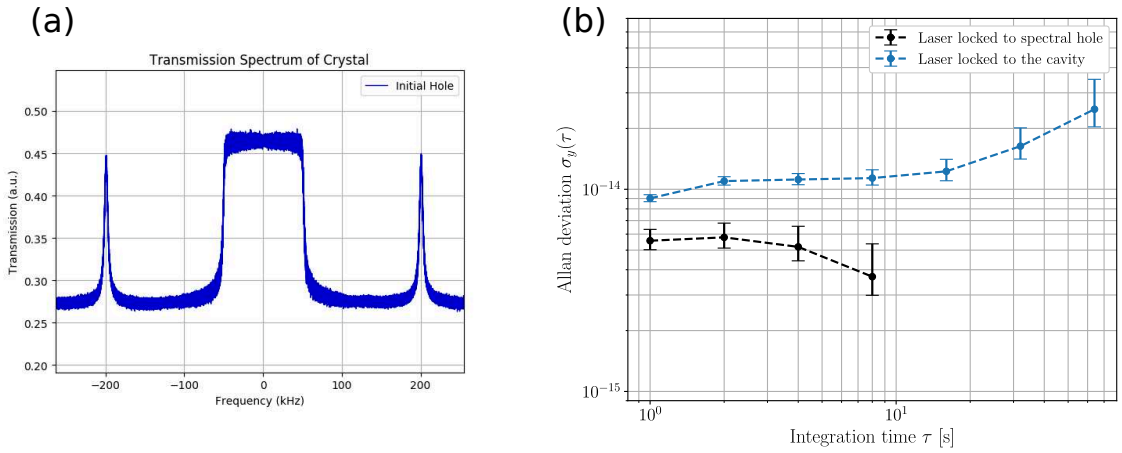

Figure 1-28: (a) the spectral structure used for three mode probing method. Two narrow holes are created and frequency positioned on the left and right of the spectrum. One square hole is burned with 100 kHz width, and it's in the center of the spectrum. (b) the laser frequency stability when locking onto the cavity only as it shown in the blue curve, and post-locking onto the holes as it shown in the black curve.

As a quick test to see if the triple-mode detection improves the laser frequency stability, the spectral pattern is created as two narrow holes located at the left and right of the spectrum and one square hole in the middle. Starting from a prestabliza-tion cavity at 9 $\times 10^{-15}$ at 1 s and by locking the laser onto the two narrow holes, the final obtained frequency stability is 5 $\times 10^{-15}$ at 1 s, as it shown in Fig. 1-28. Comparing with the results using double heterodyne detection, this value is, disappointingly higher.

This test was carried out at the end of a long period (more than 6 months) where the cryostat was in continuous operation, and we noted that the lowest temperatures achieved have meanwhile increased to 62 K, 4.2 K, and 5.8 K at the 50 K stage, the 4 K stage, and the IVC respectively. It was an indication of poisoning of the Helium circuit in the pulsed-tube cryocooler, leading to a broader spectral hole (FWHM 6 kHz for the narrow holes) and a reduced discriminator (0.14 mrad.Hz^{-1} instead of 0.18 mrad.Hz^{-1}). Also, the prestabilization cavity is not at its best, possibly due to the lack of power stabilization, residual amplitude modulation in the electrooptic modulator for the Pound-Drever-Hall lock, *etc.* We have decided therefore not to pursue the improvement of laser frequency stability further before other improvements related to the multi-mode generation are carried out.

Indeed, the off-set phase lock between the master and the slave lasers has a bandwidth of about 800 kHz. Detecting each frequency mode in the slave laser through a beatnote with the master laser necessarily replicates the beatnote spectrum with a servo bump around $\pm$800 kHz. This means a dramatic reduction of the signal to noise ratio once more than 3 modes are generated, as some of the servo bumps would superpose with some desired modes. This problem can be mitigated by removing the master laser (optical local oscillator at about 1.6 GHz away) and generate using the slave laser, in addition to the polyphase synthesized modes, an optical local oscillator at only a few MHz away. Incidently, such an implementation would remove the heating effects from the 1 mW optical power of the master laser. It would however require a faster AOM for signal generation, and more sensitive photodiodes for detection.

These changes are currently implemented and characterized on the experiment by the team and preliminary results seem to indicate a detection noise floor in the 10^{-17} range at 1 s, paving the way towards better laser frequency stabilities in the future.

1.6 Summary and Discussion

The spectral hole burning technique in rare earth ions doped crystal may provide competitive application in the ultra-stable laser, because of the lower thermal noise and better quality factor of the crystal compared with the lasers stabilized by locking onto the Fabry-Perot cavities. In this chapter, the experimental set-up used for spectral hole burning technique is described. The spectral holes burnt in the Eu^{3+}:Y_2SiO_5 crystal are characterized, and finally used as frequency reference in the application of laser stabilization.

The differential detection method allows us to get lower detection noise (below 5×10^{-16} at 1 s tested without the crystal and the cryostat), resulting in a final laser frequency stability of 1.7×10^{-15} at 1 s using the double heterodyne detection scheme. This result is comparable with the most advanced ultra-stable lasers achieved via spectral hole burning technique. Considering the large space for improvement in our system, this result encourages us to further improve the performance of our laser.

The environmental condition is firstly improved by finding a global cancellation point where the temperature and isotropic pressure effect on the holes can be compensated, leading to a minimized perturbation in the environment for the spectral hole to be burned or probed. Future work about reaching dilution temperatures and further reducing the thermal sensitivity of the spectral holes is ongoing.

The multi-channel detection method lays the ground work for the creation of multiple holes, which in theory should get lower detection noise, and therefore better frequency stability. The first attempt at triple modes detection proves that a lower

detection noise than before is reachable, thanks to the novel flowgraph utilizing the polyphase technique. The ongoing work is to add more modes in the detection, carefully characterize the optimal operation condition and hopefully improve the laser frequency stability in the near future.

Chapter 2

Stark Effect of Europium Ions in Yttrium Orthosilicate Matrix

This chapter presents the Stark effect measurements of europium ions in Eu^{3+}:Y_2SiO_5 (Eu:YSO) crystal at cryogenic temperature (3.2 K). Ultra-high precision measurements are carried out to study the spectral hole's response to an external electric field. The statistical analysis of the spectral lines provide Stark coefficients, which are interesting for applications of the Stark effect in laser frequency stabilization using spectral hole burning techniques. The main results in this chapter have been published in a peer-reviewed article [32].

2.1 Introduction

The Stark effect describes the phenomenon of splitting and shifting in spectral lines due to the modification of ions' energy level with an externally applied electric field. The presence of external electric field will affect the ions' behavior by modifying the orbitals and internal energy levels of the ions.

Stark shift of spectral lines can be characterized by the ions Stark coefficients. The

experimental study of the Stark coefficients characterizes the response of rare-earth ions optical transition in terms of transition frequency change, in the presence of an external electric field.

For ultra-stable lasers, it is crucial to know potential noise sources which may cause laser frequency shifts, thus providing insight about ways to remove or minimize such effect. For ultra-stable laser referenced on an atomic transition of rare earth ions, the stark effect provides a mechanism by which external parasitic electric fields may affect the laser's frequency and degrade its fractional frequency stability.

The Stark effect of spectral holes has been previously studied in the Eu^{3+}:Y_2SiO_5 system for one of the crystallographic sites (site 1), with limited precision and only focusing on linear symmetric effects [46, 47]. In this chapter, we investigate both sites and higher order of Stark effect with spectral holes burnt in the Eu^{3+}:Y_2SiO_5 crystal in a high precision experimental system. The more precisely measured Stark coefficients are provided. Moreover, both symmetric and asymmetric behaviors of spectral holes frequency shift have been studied in our system.

2.2 Experimental Set-up and Applied Electric Field Uncertainties

2.2.1 Experimental Set-up

The details of the whole experimental set-up is presented in Chapter 1. This section will focus specifically on presenting the generation of the electric field which is not used in the other experiments presented in this thesis.

The set-up for studying the electric field effect on spectral holes burnt in the europium doped yttrium orthosilicate crystal is shown in Fig. 2-1 (a). Two circular copper plates are used as electrodes. A voltage U is applied to the top copper plate,

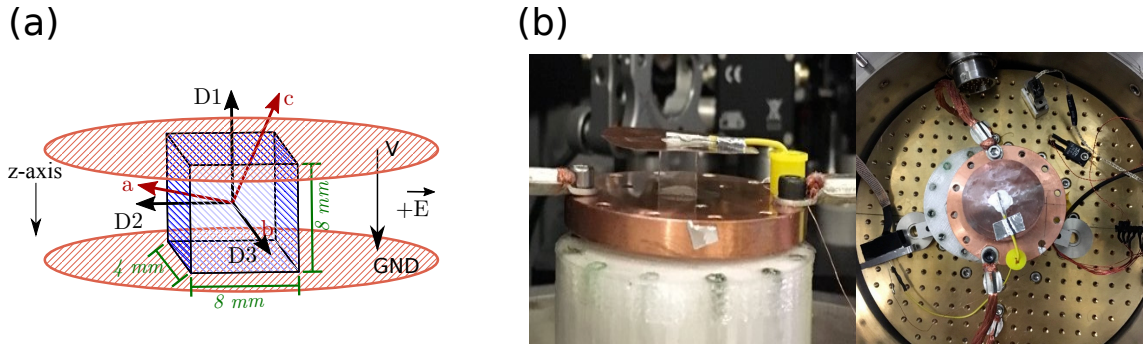

Figure 2-1: (a) The model of the E-field experiment set-up, showing that a three-dimensional parallel plate capacitor with the Eu^{3+}:Y_2SiO_5 crystal between the plates. (b) The photo of the experimental set-up from the in front view and top view. The whole set-up is positioned in a cryostat where temperature is stabilized at 3.2 K with high vacuum environment 1 $\times 10^{-9}$ mbar. The dielectric constant of the crystal is approximately 10, and 1 for the vacuum environment.

and the bottom copper plate is grounded. The two electrodes are positioned parallel to each other. The 8 mm $\times$8 mm $\times$4 mm Eu:YSO crystal is sandwiched in the center of electrodes.

In the construction of experiment set-up, initially two identical copper round plate were planned to be used as electrodes. But because of technical challenges in the installation, the final chosen electrodes are different in size as it shown in Fig. 2-1 (b). The top electrode has diameter of 31 mm, while the bottom electrode is around 41 mm in diameter. The electric field in the crystal is then verified by a numerical simulation which presents in Sec. 2.2.3. Based on the simulation, we can conclude that within a certain range, the size difference between the two electrodes almost has no effect on the E-field distribution within the volume of beam propagation.

Considering dielectric permittivity of the crystal is about 10 times larger than that of vacuum, gaps between the crystal and electrodes, which will lead to uncontrollable inhomogeneity of the applied field, need to be avoided.Therefore, two layers of silver lacquer (thickness is estimated to be below 0.1 mm) are used on the top and bottom of the crystal, thus making the crystal contact the charged electrodes directly.

The two electrodes are perpendicular to D_1 or D_2 axis, depending on how we

choose to orient the crystal, allowing the generated E-field to be applied along the direction of D_1 or D_2 axis. The main factors which affect the E-field accuracy are the applied voltage, crystal dimensions and the alignment of the two copper electrodes. The relevant electric field uncertainties are discussed in the following subsections, and all of them are considered in deducing the uncertainty of the obtained Stark coefficients.

2.2.2 Voltage Source Calibration and Crystal Dimension

The voltage source (model: TENMA 72-2685) used in this experiment is a single channel adjustable power supply with 4 digits display (maximum output voltage: 30 V). The output voltage between the anode and the cathode terminal is verified with a SI-traceable calibrated LCD digital multi-meter (model: IDM 981V) with the reading uncertainty below 0.09% according to the instrument manuel. The applied voltage on the electrode has a less than ± 0.01 V uncertainty. This uncertainty is considered in the analysis of electric field linear and quadratic effects.

Since our crystal has four un-polished faces, and the optical beam cannot propagate through the unpolished crystal faces, so in all our measurement the E-field is only applied along D_1 or D_2 axis. Therefore the E-field uncertainties are only considered for the D_1 and D_2 axis.

The investigated crystal is a 8 mm $\times$8 mm $\times$4 mm Eu^{3+} doped Y_2SiO_5 single crystal with 0.1% doping level, which is grown by the Czochralski method with natural abundance of the two isotopes ^{151}Eu and ^{153}Eu [48]. The crystal cutting uncertainty is less than $\pm\ 0.5^\circ$ on the orientation of the dielectric axis, as set by X-ray diffraction and precision machining. Thus the E-field which is expected to be parallel to the D_1 axis will have a residual component on the D_2 or D_3 axis with a factor of $\sin(0.5^\circ)$ coming from the crystal dimension cutting uncertainty. This uncertainty is then considered as the systematic errors in the applications of E-field. In our measurements, the

systematic uncertainty of the E-field can then be expressed as $\Delta E_{\mathrm{D2}} = E_{\mathrm{D1}} \times \sin(0.5^\circ)$ and $\Delta E_{\mathrm{D1}} = E_{\mathrm{D2}} \times \sin(0.5^\circ)$.

2.2.3 Theoretical Simulation of the Electric Field

In our experiments, the electric field is assumed to be purely along the vertical z direction ($\|$ D_1 or $\|$ D_2) without x or y component. However, to verify that these components are indeed negligible, theoretical simulations need to be carried out. In addition, we also need to estimate the effect on the electric field resulting from, firstly, the imperfect alignment of the two electrodes or, secondly, the mismatch in their size. Therefore, numerical simulations were performed by finite element analysis using the COMSOL Multiphysics program.

When the two parallel plates are connected to a power supply with the applied voltage of U, they become charged and an electric field is established between them. In the simplest case, the electric field strength can be calculated as $E = U/d$ with the unit of $\mathrm{V.m^{-1}}$, where d is the distance between two electrodes.

For the dielectric materials, the permittivity describes the electric polarizability of the material. When there is an external electric field, the high permittivity material will polarize more than the low permittivity material. In the simulated model, the vacuum environment has a relative permittivity of 1 and the copper plates have an infinite relative permittivity. Based on the work of Tobar 2015 [49] which treats YSO as a mono-clinic biaxial crystal, with the measured temperature of 6 K, the real part of its relative permittivity can be written as:

$$\epsilon_r = \begin{pmatrix} \epsilon_x & 0 & 0 \\ 0 & \epsilon_y & 0 \\ 0 & 0 & \epsilon_z \end{pmatrix} = \begin{pmatrix} 9.36 & 0 & 0 \\ 0 & 10.90 & 0 \\ 0 & 0 & 10.21 \end{pmatrix} .$$

The electric field distribution is shown in Fig. 2-2. In order to quantitatively study the electric field distribution in the physical region where the spectral hole is burnt, a cylindrical volume V_{spot} (diameter 2 mm, depth 4 mm, centered on the crystal) is employed to represent the probe beam propagation volume inside the crystal. By integrating the electric field in the cylindrical volume V_{spot}, we could compare the x, y and z components of electric field and calculate their ratio.

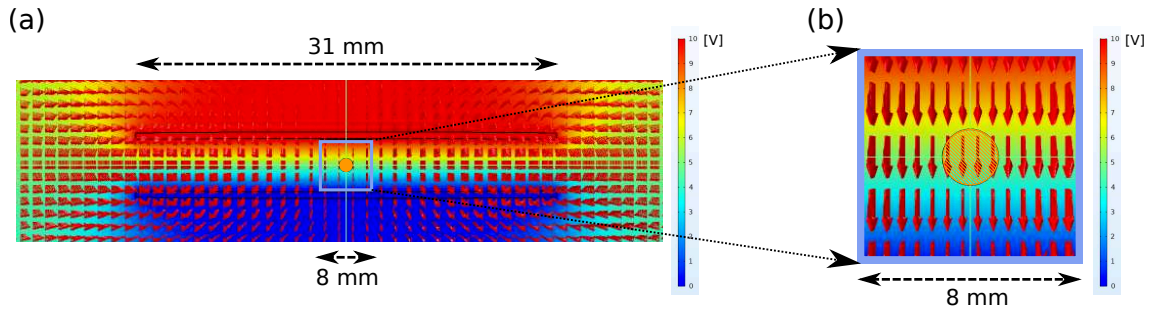

Figure 2-2: The three-dimensional model projected on a 2D plane when applying a 10 V voltage on the top electrode, and the bottom electrode is grounded. The color map shows the potential from 0 V (blue) to 10 V (red). Red arrows show the E-field direction and strength. The small yellow spot is the probe beam which is passing through the center of the crystal. (a) shows the electric field distribution in the entire environment, and (b) is a zoom in plot of the E-field distribution inside the Eu:YSO crystal.

More precisely we define three factors to estimate the distribution of E-field. The first factor F_1 is the square root of the mean square (RMS) of E-field z component in the selected volume V_{spot},

$$F_1 = \sqrt{\frac{1}{V_{spot}} \int_{V_{spot}} E_z^2 \, dV} \, .$$

Then the fractional standard deviation of E_z is evaluated in F_2,

$$F_2 = \frac{\sqrt{F_1^2 - \left(\frac{1}{V_{spot}} \int_{V_{spot}} E_z \, dV \right)^2}}{F_1} \, .$$

Moreover, since the E-field is expected to be along z direction, we investigated the

leakage in xy plane by taking the ratio between the components in the xy plane and the E_z component.

$$F_3 = \frac{\sqrt{\frac{1}{V_{spot}} \int_{V_{spot}} \left({E_x}^2 + {E_y}^2 \right) \, dV}}{F_1}$$

This factor F_3 can also help to understand the spectral hole's broadening from the perspective of E-field leakage (see Sec. 2.6).

In the simulation, the bottom electrode keeps in the center, with a constant diameter of 31 mm. When gradually shifting the top electrode along x (or y) direction by 1 mm to simulate the misalignment of the electrodes, the E-field z component distribution showing in F_1 factor has less than 0.002% change. The standard deviation of E_z showing in F_2 is in the order of 10^{-3}, and is almost constant (difference $<$0.007%) when the top electrode moved by 1 mm. If the top electrode has a misalignment up to 10 mm, F_1 and F_2 also almost have no change ($<$0.01%).

Moreover, we also simulated the case of asymmetric geometry of the pair electrodes which may cause the asymmetric distribution of the generated E-field. For instance, when increasing the diameter of the top electrode to 41 mm, in volume V_{spot}, both F_1 and F_2 have less than 0.01% change.

One may notice that under different configurations the E_x and E_y will have tiny change, but since E_z is much stronger than E_x, E_y field by a factor of more than 10^4 (see the ratio value showing in the F_3), we conclude that the different configuration of the electrodes have negligible effect on the application of electric field in our experiments.

2.3 Symmetric Linear Stark Effect

With an external electric field applied along the crystal D_1 or D_2 direction, the spectral hole will firstly split into two peaks positioning left and right relatively to the initial

Position [mm]	Diameter [mm]	F_1 [V.m^{-1}]	F_2	F_3
x = 0 ; y = 0	31	1249.9633	1.5318E-3	1.1501E-5
x = 0 ; y = 1	31	1249.9842	1.5317E-3	4.5840E-6
x = 0 ; y = 10	31	1250.0061	1.5317E-3	4.5368E-5
x = 1 ; y = 1	31	1249.9906	1.5317E-3	2.9536E-6
x = 10 ; y = 10	31	1250.0258	1.5322E-3	1.6119E-4
x = 0 ; y = 0	41	1250.0202	1.5317E-3	4.7812E-6
x = 1 ; y = 1	41	1250.0156	1.5318E-3	8.8432E-6

Table 2.1: Summary of the numerical simulation results. The position and diameter in the first and second column is for top electrode only, meaning that in the simulation only the top electrode variables are changed to see the E-field distribution difference with evaluation factors of F_1, F_2 and F_3. The bottom electrode is kept centered, and with a constant diameter of 31 mm.

hole center frequency position. The gradually increased E-field will cause the hole center frequency shift. This section will discuss the holes' symmetric response to the applied E-field for both site 1 and site 2, starting with the YSO crystal symmetry operation. Then the data analysis procedure is defined and finally the symmetric linear Stark coefficient of the europium ions is obtained from the data.

2.3.1 The Symmetry Operation of YSO Crystal with External E-field

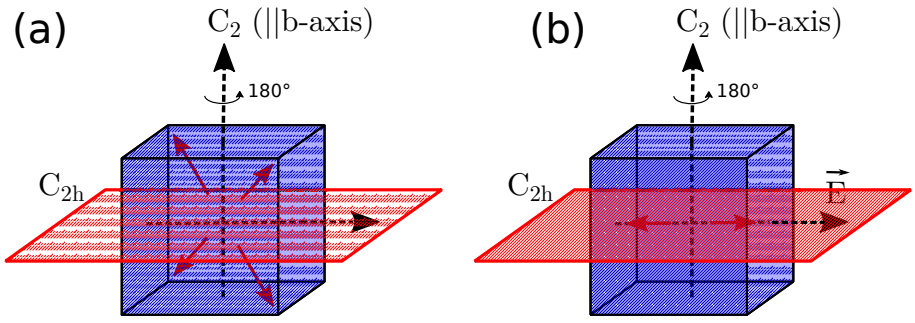

Figure 2-3: The symmetry operation of YSO crystal. The C_2 rotation axis is parallel to the b axis which is in the same direction of D_3 axis. The horizontal plane C_{2h} is the mirror symmetry plane. Eu^{3+} ions in the YSO crystal have four dipole moment components with an arbitrary E-field showing in (a), and 2 components when the E-field is applied perpendicular to the C_2 rotation axis presenting in (b).

The Y_2SiO_5 (YSO) crystal is mono-clinic and exhibits a C_{2h} symmetry. The two nonequivalent crystallographic sites of the Eu^{3+} ions are both of C_1 symmetry. In the general case of the presence of an E-field with an arbitrary direction, showing in Fig. 2-3 (a), the crystal symmetry gives rise to four possible non-equivalent orientations of the electric dipole moment difference between the ground and excited states ($\delta\vec{\mu}_i$, i=1,2,3,4) for each site, coming from the order of the crystal symmetry group (4), divided by the order of the symmetry group of the crystal site (1). In other words, for each Eu^{3+} ion in a given crystallographic environment which sets its dipole difference in one of the allowed direction, there will be, statistically, 3 other Eu^{3+} ions at other places in the crystal which have their dipole difference in the other allowed directions. As we average the measurement over a large number of ions (a spectral hole represents approximately 10^{13} Eu^{3+} ions), this gives rise to four components of the dipole moments with the presence of an arbitrary electric field. Thus, in the general case, the presence of an arbitrary electric field will split a spectral hole into 4 components [50].

The external applied E-field will modify the electric dipoles depending on the E-field direction and strength. In all the measurements mentioned in this chapter, the applied E-field is parallel to either the crystal D_1 or D_2 axis as illustrated in Fig. 2-3 (b), both of which are perpendicular to the crystal b-axis (or D_3 axis) which is in the same direction of C_2 rotational symmetry axis. As the mirror symmetry plane of the crystal is perpendicular to the C_2 rotation axis, the component of a given electric dipole moment perpendicular to mirror plane will not be influenced by our E-field. Therefore, the spectral hole only splits into two components in our measurements.

To investigate the E-field induced spectral holes response in Eu:YSO crystal, the initial hole is firstly burnt with the absence of the E-field, then its spectrum is recorded as a reference. With an external electric field applied along the D_1 direction, the initial spectral hole will split symmetrically into two peaks referred to as the positive and negative frequency branches. The crystal's transmittance is plotted as a function of frequency difference in Fig. 2-4.

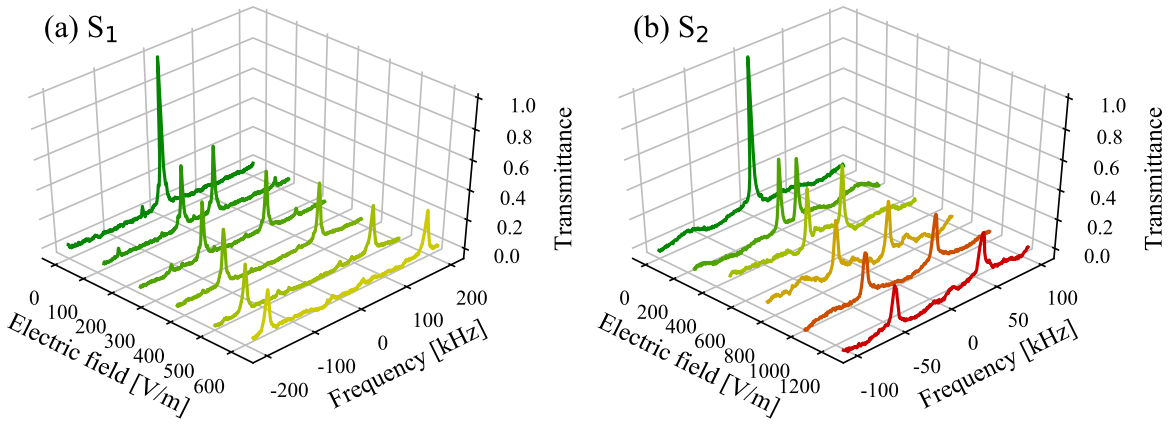

Figure 2-4: Transmittance of an Eu^{3+} doped crystal containing a spectral hole as a function of the electric field applied along the D_1 axis for (a) site 1 and (b) site 2. Gradient colors used in plotting individual spectrum show the increase in electric field strength which is also illustrated in the corresponding electric field axis with the unit of $V.m^{-1}$.

The initial hole center frequency position corresponds to the burning frequency, and is taken as the reference frequency position, meaning $f_0 = 0$. With the gradually increased E-field, the holes will shift further away from the initial hole center position, in addition to a broadening of the peaks, which will be analyzed in Sec. 2.6. The spectral holes' behavior is then studied quantitatively with a data treatment procedure in next section.

2.3.2 Center Frequency Position of the Spectral Holes

In order to quantify the linear Stark coefficient, the E-field induced spectral holes frequency shift is analyzed based on the spectral fitting. The initial hole is a single-peaked spectrum, so its transmittance is fit by a Lorentzian function as Eq. 2.3.1,

$$T_0(f) = A + \frac{B}{1 + \frac{4(f - f_0)^2}{\Gamma^2}} \tag{2.3.1}$$

where f_0 is the center frequency of the initial hole, and Γ is the full width at half maximum (FWHM) of the peak. A and B take into account the offset and normalization of the transmittance $T(f)$.

The holes subjected to an external E-field have a double-peaked spectrum. We realized that within a relative low electric field, the left and right peaks have similar linewidth (difference <10%) and transmittance (difference <5%). Therefore, in the double-peaked Lorentzian model, the left and right peaks are assumed to contain the same transmittance ($B_+ = B_- = B$) and linewidth ($\Gamma_+ = \Gamma_- = \Gamma$).

$$T(f) = A + \frac{B}{1 + \frac{4(f - f_+)^2}{\Gamma^2}} + \frac{B}{1 + \frac{4(f - f_-)^2}{\Gamma^2}} \tag{2.3.2}$$

The Equation 2.3.2 is then carried out to fit the spectrum in order to determine the new center position for both left and right peaks. f_+ and f_- are the newly defined peak centers for positive and negative branches respectively.

2.3.3 Symmetric Linear Center Frequency Shift of the Spectral Holes

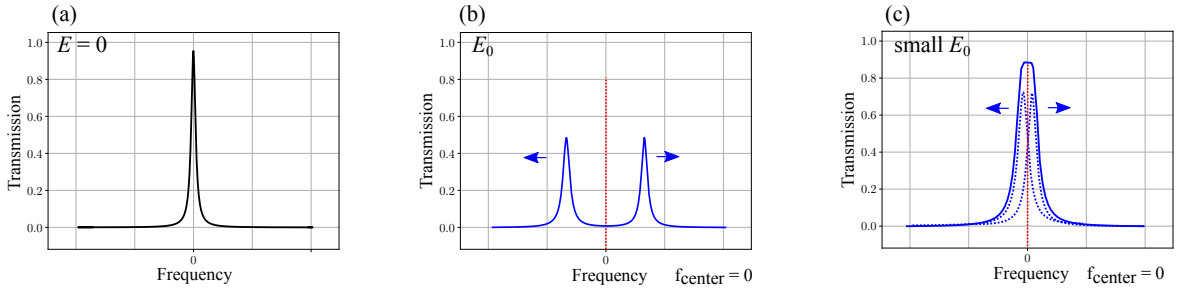

Figure 2-5: Symmetric effect of the spectral holes when (a) there is no E-field, (b) an external E-field E_0 is applied in the Eu:YSO system, and (c) a low E-field is applied on the crystal. The red lines in (b) and (c) show the relative center of the spectrum, symbolized as f_{center}. The symmetric behavior of the spectral lines will not change the center of the peaks, but will only broaden the holes in their linewidth, resulting in a flatter curvature in the center.

Figure 2-5 shows the symmetric behavior of the holes when an external electric field E_0 applied on the crystal. Arrows in the Fig. 2-5 (b) present that peaks move in the opposite direction. The red dash line is to show the spectrum center, which is assumed to be in the center in the calculation of this section.

The average of the frequency offset in positive and negative branch can be written as

$$\delta f_1^2 = (f_+^2 + f_-^2)/4.$$

As we are interested here by the symmetric linear Stark coefficient, and no significant non-linearity is observed, δf is then modeled by a pure linear function $\delta f_1 = A_1 \times E$ to determine the symmetric linear Stark coefficients, which we denote as A_1.

Figure 2-6 shows the linear frequency shifts as a function of E-field. Each data point in Fig. 2-6 is the average value from two or three separate measurement sequences. Each spectrum is estimated individually to get the center frequency of the hole, because the noise floor is different from scan to scan causing the variation in the data baselines and adding the uncertainties in defining the center frequencies of each spectrum.

The error bars of the data points in Fig. 2-6 come from, firstly, the fitting algorithm which is the standard deviation of the peak center position estimation in the Lorentzian function fitting process, and secondly, the repeatability of multiple independent measurements, which is the obtained spectral hole center position standard deviation in different independent measurements under same experimental conditions.

Table 2.2 shows the symmetric linear Stark coefficients obtained by the pure linear model with the unite of Hz.V.$^{-1}$, corresponding to the curves in Fig. 2-6. The uncertainties of the symmetric linear coefficients include two components: the statistical uncertainties and the systematic uncertainties.

The statistical uncertainties include, firstly, the fitting uncertainty which is the standard deviation of the linear slope A_1 in the linear model, and secondly the re-

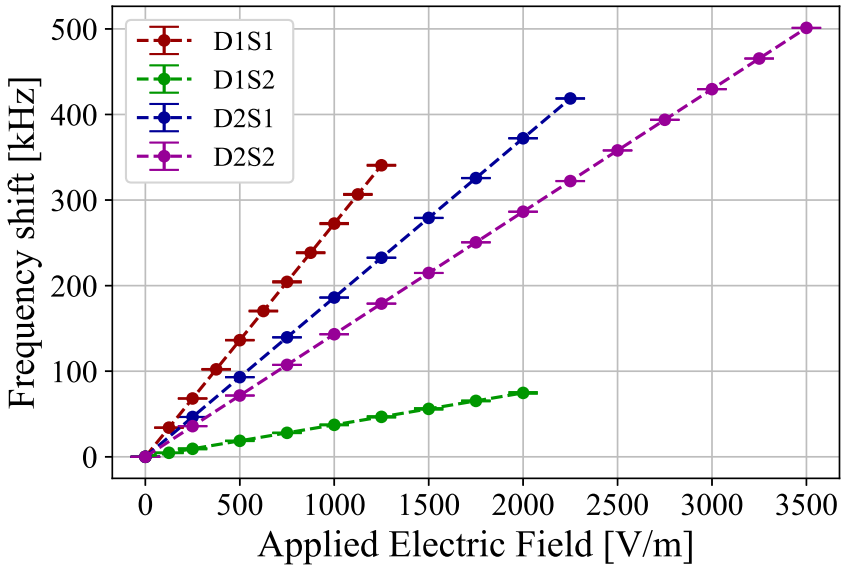

Figure 2-6: Symmetric linear center frequency shifts of the spectral holes in the Eu:YSO system with the presence of an external E-field along D_1 or D_2 axis for the two substitution sites, site 1 and site 2.

peatability of the experiments which means considering the standard deviation of the linear coefficients in several independent measurements.

The systematic uncertainties in the linear coefficients come from the crystal geometry, which will add uncertainty in the orientation of the dielectric axis (see the illustration in Sec. 2.2.2). If an E-field is assumed to be applied along the D_1 axis, because of the cutting uncertainty in crystal geometry, the applied electric field will have a small angle with the D_1 axis resulting in a small component of electric field along the D_2 axis or b (D_3) axis.

Considering the crystal cutting uncertainty is less than $\pm 0.5°$, the D_1 axis Stark coefficients will be affected by the coefficients along D_2 where the cutting uncertainty induces a kind of E-field leakage on D_1 axis. For instance, the linear coefficient of Site 1 D_2 is 186.1 $\pm$0.4 Hz.m.V^{-1}, and it will add the systematic uncertainty in the symmetric linear coefficient of Site 1 D_1 as 186.1 $\pm$0.4 Hz.m.V^{-1} times sin(0.5°) which is around 1.6 Hz.m.V^{-1}. The symbols $\pm$ and $\mp$ in the Tab. 2.2 is to present

the systematic errors in D_1 and D_2 axis going in opposite directions.

Site	Axis	Symmetric Linear Stark Coefficient	Statistical Uncertainty	Systematic Uncertainty
1	D_1	271.8	$\pm$ 0.5	$\pm$ 1.6
1	D_2	186.1	$\pm$ 0.4	$\mp$ 2.4
2	D_1	37.4	$\pm$ 0.5	$\pm$ 1.2
2	D_2	143.2	$\pm$ 0.5	$\mp$ 0.3

Table 2.2: Linear Stark coefficients of the spectral holes in Eu:YSO in the unit of Hz.m.V^{-1}. The systematic error bars of the linear Stark coefficients come from the crystal cutting uncertainty, which is illustrated in the Sec. 2.2.2

In the Tab. 2.2, the Site 1 D_1 is the most sensitive case which is 271.8 Hz.m.V^{-1}, and Site 2 D_1 contains the less sensitive symmetric linear Stark coefficient 37.4 Hz.m.V^{-1}. The symmetric linear Stark coefficient obtained here is consistent with the less accurate measurement in the reference [47], which reported in Eu:YSO system the electric field linear coefficient is 0.27 kHz.m.V^{-1} for Site 1 D_1 without error bars in the coefficient. Our measurement is done when the E-field is applied along D_1 or D_2 axis for both Site 1 and Site 2 with an unprecedented accuracy.

2.4 Asymmetric Linear Stark Effect

The symmetric linear Stark effect describes that the left and right spectral holes will move to the opposite direction with the E-field, while the center position of the spectrum does not change (see Fig. 2-5). Therefore, when the laser frequency is locked on the narrow spectral hole, considering the symmetric linear Stark effect, the presence of the E-field will only broaden the spectral hole but does not change the frequency. So only the locking gain needs to be optimized according to the hole linewidth, but the locking frequency remains unchanged. To investigate the potential impact on the laser frequency stability, it is necessary to study the asymmetric and higher order Stark effect. Therefore, high precision measurements need to be carried out.

2.4.1 Asymmetric Behavior of the Spectral Hole

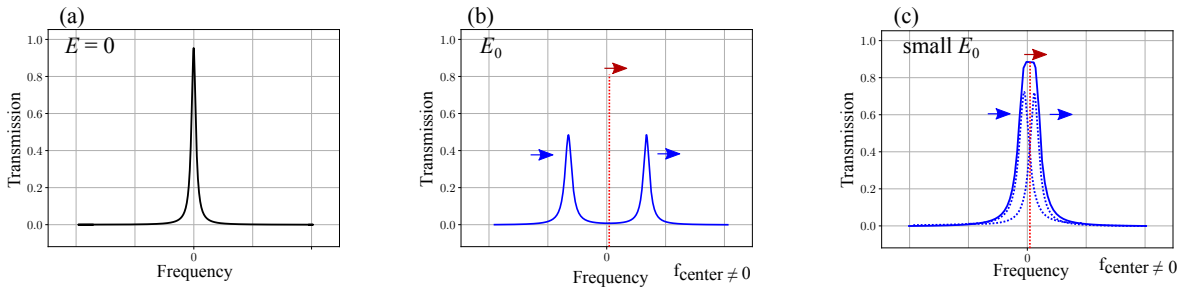

Figure 2-7: Asymmetric effect of the spectral holes. (a) The initial hole burnt with no E-field shows, (b) the case with an external E-field E_0 shows, and (c) the low E-field conditions. The red lines in (b) and (c) show the relative center of the spectrum, symbolized as f_{center}, which has a tiny offset in frequency. Thus the asymmetric behavior of the peaks will have an influence on the laser frequency stability, when the laser is stabilized by taking the center frequency of such holes as a frequency reference.

The asymmetric behavior means that the left and right peaks shift in one direction, resulting a tiny frequency fluctuation in the average center of the spectrum, which is named as f_{center} in Fig. 2-7. So the asymmetric linear Stark effect will have influence on the laser frequency stability, thus it needs to be studied. The obtained asymmetric linear Stark coefficient will provide useful information for optimization of laser frequency stability, when the ultra-stable lasers are achieved by locking on the narrow spectral holes. The comb measurement needs to be taken into account here to analyze this small frequency shift phenomenon.

Our laser is prestabilized by a high finesse Fabry-Perot cavity. Then the laser is stabilized by locking to the narrow spectral pattern burnt in the Eu:YSO crystal at cryogenic temperature. The spectral hole linewidth is around 3 kHz to 5 kHz in FWHM. These enable us to make high precision measurements.

In order to obtain an accurate measurement of the laser frequency, an optical frequency comb is used to provide a frequency reference. So that the probing laser can be referenced by a high precision measurement in frequency. The small center frequency shift of the spectral hole can then be observed and analyzed in our system.

The details about the comb dedrifting measurement are presented in the Sec. 1.3.3. The counted laser frequency can be fitted by a pure linear model with the linear slope of a. Then the frequency drift can be calculated by multiplying the laser frequency drift slope a times the time interval between the initial hole burn time and the i_{th} scan time:

$$f_{\text{drift}} = a \times (t_i - t_{\text{burn}}) = a \times \delta t,$$

where i is the serial number of the scan (corresponding to the i_{th} recorded spectrum), and $\delta t = t_i - t_{\text{burn}}$ is the elapsed time since hole burning. Therefore the spectral holes center frequency f_- and f_+ can be subtracted by this de-drifting factor. Eventually the de-drifted spectral hole center frequency F_+ can be written as

$$F_+ = f_+ - a \times \delta t$$

for instance of the peak in positive branch.

With the help of comb measurements, after de-drifting the cavity induced laser frequency drift, the small frequency shift of the spectral holes due to the E-field can be deduced and analyzed. The asymmetric linear frequency shift, which is a small value in frequency, is investigated and presented in this section.

2.4.2 Asymmetric Linear Center Frequency Shift of the Spectral Holes

In the data analysis, the average of the left and right peak centers $(f_+ + f_-)/2$ is taken to subtract the laser frequency drift coming from the reference cavity according to the comb measurement. The asymmetric linear component can then be written as

$$\delta f_2 = (f_+ + f_-)/2 - a \times \delta t,$$

where f_+ and f_- is the left and right peak center coming from the aforementioned double Lorentzian fitting model in Eq. 2.3.2.

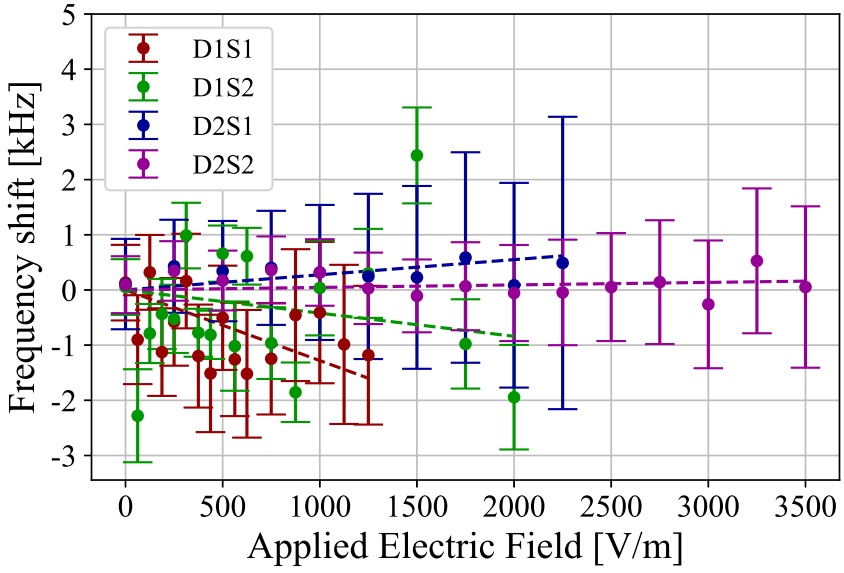

Figure 2-8: Asymmetric linear center frequency shifts of the spectral holes in the Eu:YSO system with the presence of an external E-field along D_1 or D_2 axis for the two substitution sites, site 1 and site 2.

The asymmetric linear components are plotted as a function of the applied electric field, showing in Fig. 2-8. Each data point in the curves is the averaged value of asymmetric linear components δf_2 from two or three independent measurements.

The spectra fitting process will provide the uncertainty of fitting parameters, from which we can deduce the standard deviation of spectral hole center frequency, which is named as Δf_{fit} in the following calculation.

The optical signal is detected by the Thorlabs' avalanche photodiodes (model: APD 410A/M) and their phase information is recorded by a control system driven by the Software Defined Radio (SDR) device from Ettus Research with the model of USRP X310 (Universal Software Radio Peripheral). We investigated the timing jitters in the recorded data, which is the uncertainty in frequency from the spectrum alignment of the starting point [34]. In this experiment, the spectrum alignment

has an uncertainty less than 100 Hz, which is statistically calculated as the standard deviation of the misalignment of the spectrum starting point and stopping point. This spectrum alignment uncertainty is included in the data analysis as

$$\Delta f_{\text{alignment}} = 100\,\text{Hz}\,.$$

It contributes to the data point error bars and the statistical uncertainty of Stark coefficients.

In addition, in each set of measurement, the initial hole is first recorded as a reference spectrum, and then after multiple scans, the initial hole is scanned again at the end of each measurement to verify the frequency drift from other noise sources. This kind of uncertainty in frequency is less than 100 Hz, meaning it is covered by the spectrum alignment uncertainty $\Delta f_{\text{alignment}}$.

The spectral holes with the presence of the electric field have a linewidth (FWHM) ranging from 3 kHz to 5 kHz. Multiple probing of the holes will lead to a slightly broadening of the hole. The spectral hole broadening will somehow affect the center position determination. In the spectra fitting process, we found the broadening induced center position uncertainty is less than tenth of the hole width. So the tenth of the spectral hole linewidth (10%Γ) is considered as the broadening induced center frequency determination uncertainty in the error bars of the data point δf_2.

The error bar in the data point in Fig. 2-8 is then defined as the maximum of the hole center position fitting uncertainty Δf_{fit}, and the spectrum alignment uncertainty $\Delta f_{\text{alignment}}$ combined with tenth of hole width 10%Γ (see Eq. 2.4.1).

$$\Delta f_2 = \sqrt{\max(\Delta f_{\text{fit}}, \Gamma \times 10\%)^2 + (\Delta f_{\text{alignment}})^2} \tag{2.4.1}$$

2.4.3 Asymmetric Linear Coefficients

The asymmetric linear component is then modeled by a pure linear function

$$\delta f_2 = A_2 \times E.$$

Table 2.3 shows the asymmetric linear Stark coefficients corresponding to the curves in Fig. 2-8. The data analysis is in the same way as mentioned in Sec. 2.3.3. The statistical uncertainty of the coefficients include the linear coefficient fitting uncertainty and the independent measurements repeatability. The systematic uncertainty in the linear coefficients is from the crystal cutting uncertainty.

Site	Axis	Asymmetric Linear Stark Coefficient	Statistical Uncertainty	Absolute Value Upper Limit
1	D_1	-1.28	$\pm$ 0.46	$\pm$ 5.0
1	D_2	0.27	$\pm$ 0.41	$\pm$ 5.0
2	D_1	-0.42	$\pm$ 0.20	$\mp$ 5.0
2	D_2	0.05	$\pm$ 0.13	$\mp$ 5.0

Table 2.3: Asymmetric linear Stark coefficients of the spectral holes in Eu:YSO in the unit of Hz.m.V^{-1}.

We add a upper limit for the absolute value of the asymmetric linear coefficients, which can help us estimate environmental requirements. If we consider the upper limit of 5.0 Hz.m.V^{-1} for Site 1 D_1, the desired 10^{-17} frequency stability at 1 s needs the environment has less than 1 mV.m^{-1} E-field fluctuation.

2.5 Quadratic Effect

For the application of ultra-stable lasers using the narrow spectral hole pattern as frequency reference, the higher order Stark effect, especially the one which will introduce the non-symmetric behavior, needs to be studied. With the help of the comb measurement, it is possible to analyze the higher order of Stark effect in our system.

This section presents the data analysis used to quantify the quadratic effects, in particular the asymmetric quadratic effect, which is the most important in the context of high stability laser frequency stabilization. In the meanwhile the symmetric quadratic effect is also described in this section even though it does not affect the laser frequency stability.

2.5.1 Asymmetric Quadratic Effect

The asymmetric quadratic effect of the hole describes the left and right peaks moving to the same direction under the application of a low E-field, presenting in Figure2-7 (c). As a result, the envelope curvature of the left and right peaks, which will be used for locking the laser frequency, will not only has a broaden linewidth but also has a small shift in the hole center.

The asymmetric quadratic effect caused small shift in hole center, when locking the laser on the hole, makes a possible frequency fluctuation as a result. So the higher order asymmetric Stark effect will give us the information about how the E-field affect the laser frequency stability correspondingly. This is a useful information to quantify maximum E-field fluctuation tolerable for a given frequency stability target.

To investigate the asymmetric quadratic component, we take $(f_+ + f_-)/2 - f_0$ as the relative center position of the positive and negative peaks with respect to the initial hole center frequency, where $f_0 = 0$. The cavity induced laser frequency drift $a \times \delta t$ is also removed according to the comb counting measurement. We then plot the

$$\delta f_3 = (f_+ + f_-)/2 - a \times \delta t$$

as a function of the electric field, see Fig. 2-9. The data points are the average value of asymmetric quadratic components δf_3 obtained from two or more separate measurement sequences.

A purely quadratic function,

$$\delta f_3 = A_3 \times E^2$$

is used to fit the data to obtain the asymmetric quadratic coefficient A_3.

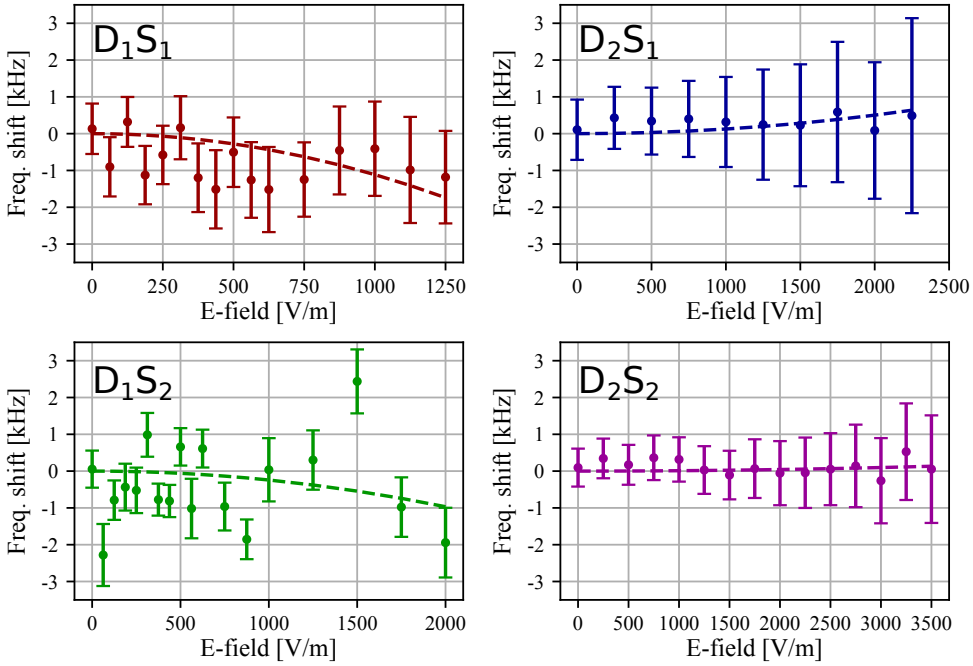

Figure 2-9: Asymmetric quadratic components δf_3 for Site 1 and Site 2 in Eu:YSO system when an external electric field is applied parallel to the D_1 or D_2 axis. The dashed line is a quadratic fit of the data, showing an effect compatible with zero to within the measurement uncertainty.

The asymmetric quadratic coefficients A_3 are given in Tab. 2.4 corresponding to the data in Fig. 2-9 for the two different sites when the E-field is applied parallel to the D_1 or D_2 axis. The uncertainties of the asymmetric quadratic coefficients come from the fit algorithm and the repeatability of several independent measurements, and these are presented in the statistical uncertainties in the fourth column of Tab. 2.4.

These quadratic coefficient can be considered compatible with zero given the measurement uncertainties, and, as conservative estimates, we set the upper limits stated in the last column of the Tab. 2.4. The upper limit of the asymmetric quadratic

Site	Axis	Value	Stat.	Abs. val. upper limit
1	D_1	-11.1×10^{-4}	$\pm 5.0 \times 10^{-4}$	$< 3 \times 10^{-3}$
1	D_2	1.3×10^{-4}	$\pm 2.6 \times 10^{-4}$	$< 1 \times 10^{-3}$
2	D_1	-2.4×10^{-4}	$\pm 1.4 \times 10^{-4}$	$< 1 \times 10^{-3}$
2	D_2	0.1×10^{-4}	$\pm 0.5 \times 10^{-4}$	$< 2 \times 10^{-4}$

Table 2.4: Asymmetric Quadratic Stark coefficients for residues after subtracting the linear component. These coefficients are given in the unit of $Hz.m^2.V^{-2}$. The crystal cutting uncertainty induced systematic error here is negligible compared to the statistic error.

coefficient is provided depending on the axis and sites in our system which is below 1 $\times 10^{-3}$ $Hz.m^2.V^{-2}$. This upper limit is an important information for the laser frequency stabilization study when the E-field induced frequency shift needs to be considered in the system.

For instance, if we want to reach a relative frequency stability of 10^{-17} at 1 s using a spectral hole as a frequency reference, considering the spectral hole is burnt with site 1 frequency which is around 517 THz, an asymmetric quadratic Stark effect <1 $\times 10^{-3}$ $Hz.m^2.V^{-2}$ translates into a requirement of the E-field stability below 2.3 $V.m^{-1}$. Therefore this estimation will be helpful in optimization of the experimental environment.

2.5.2 Symmetric Quadratic Effect

For the spectral holes burnt in the Eu:YSO crystal, the deviation of the linear Stark effect could potentially lead to a quadratic effect which would shift the negative and positive branch in symmetrical directions. This kind of symmetric quadratic effect will still be proportional to the field strength but will be a small value thus is difficult to be observed in the spectrum.

The symmetric quadratic effect is regarded as the opposite shift of the spectrum, which is to say the positive and negative branch are shifting simultaneous in opposite direction as illustrated in Fig. 2-5 (c). Thus we can take average center of the spectrum

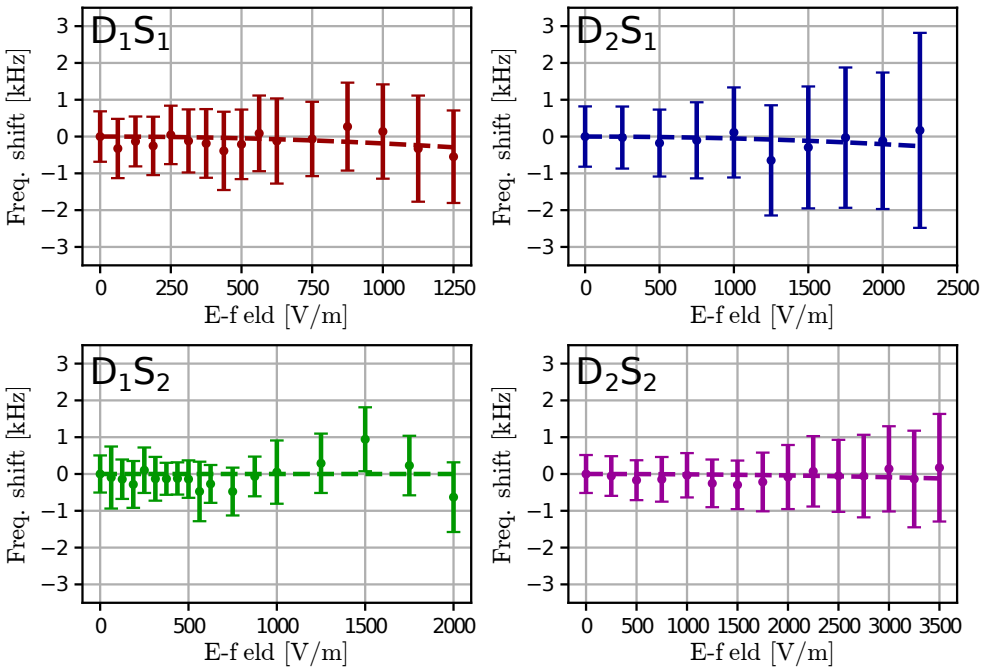

Figure 2-10: Symmetric quadratic components δf_4 for Site 1 and Site 2 in Eu:YSO system when an external electric field is applied parallel to the D_1 or D_2 axis. The data is the same as the one used in asymmetric quadratic effect but with a different treatment method.

to study the symmetric quadratic effect in the system. The symmetric quadratic effect is investigated by subtracting the linear Stark shift component $A_1 \times E$ to get a residual. After that the cavity induced laser frequency drift $a \times \delta t$ is also removed according to the comb measurement,

$$\delta f_4 = (f_+ - f_-)/2 - A_1 \times E - a \times \delta t$$

δt is the time interval between the studied hole probe time and initial hole burning time. Then the drift removed symmetric quadratic component is fit by a pure quadratic function: $\delta f_4 = A_4 \times E^2$ where A_4 is the desired symmetric quadratic coefficient. This is plotted in Fig. 2-10.

In Fig. 2-10, the data point in each curve is the average symmetric quadratic components from two or three measurement sequences. The error bars are defined in the same way as in the study of the asymmetric quadratic effect defined in Eq. 2.4.1

considering both the spectrum alignment and spectral hole width.

Figure 2-10 shows the symmetric quadratic component when an external E-field is applied on the crystal, in which the x-axis is the applied electric field strength and δf_4 is the y-axis value with an error bar of Δf_4. The symmetric quadratic coefficients are extracted from the fit of the data in Fig. 2-10 and summarized in Tab. 2.5. The uncertainty in the coefficients comes from the pure quadratic fit procedure. Un upper limit of the symmetric quadratic Stark shift is also given in the last column of Tab. 2.5.

Site	Axis	Value	Stat. uncertainty	Abs. val. upper limit of the coefficient
1	D_1	-1.3×10^{-4}	$\pm 5.1 \times 10^{-4}$	$< 1 \times 10^{-3}$
1	D_2	-0.7×10^{-4}	$\pm 1.5 \times 10^{-4}$	$< 1 \times 10^{-3}$
2	D_1	-0.5×10^{-4}	$\pm 2.6 \times 10^{-4}$	$< 1 \times 10^{-3}$
2	D_2	-0.1×10^{-4}	$\pm 0.5 \times 10^{-4}$	$< 1 \times 10^{-3}$

Table 2.5: Symmetric Quadratic Stark coefficients for residual frequency shifts after subtracting the linear components. These coefficients are given in the unit of $\mathrm{Hz.V^{-2}.m^2}$.

Even though the symmetric quadratic effect will not have influence on the laser frequency stability when locking the laser on the narrow hole, this information is still interesting for the further study and better understanding of spectral hole burning technique.

2.6 Spectral Holes' Broadening

In Fig. 2-4, when the electric field strength increases, the spectral holes not only have a splitting phenomenon but also have a gradually broadening behavior in the linewidth. Possible reasons that will cause the spectral hole broadening include the over burning of the hole, or inhomogeneous response of an ion ensemble from the perturbation noise, such as the E-field. This section is to investigate the electric field induced spectral holes broadening with experimental method.

2.6.1 Broadening Normalization to the Width of the Initial Hole

We use the same model in the E-field induced spectral hole frequency shift study. So the initial spectral holes linewidth is obtained by the variable Γ_0 in the Lorentzian fitting in Eq. 2.3.1. The i_{th} scanned split holes linewidth are firstly notes asΓ_+ for the left peak and Γ_- for the right peak separately, with the similar fitting model in Eq. 2.3.2.

$$T(f) = A + \frac{B}{1 + \frac{4(f - f_+)^2}{{\Gamma_+}^2}} + \frac{B}{1 + \frac{4(f - f_-)^2}{{\Gamma_-}^2}}$$

Since several independent measurements prove that the width difference between the left and right peak are less than 10%, so in the final data treatment we take the average of left and right peaks FWHM as the investigated hole width and noted as Γ_i.

The broadening normalization is then taken as the ratio between the width (FWHM) of the spectral hole and the width of the initial hole, to see their relationship with the applied E-field. Eq. 2.6.1 is the definition of broadening normalized to the width of the initial hole. Therefore the ratio value Γ_N can be used to see the hole width changes.

$$\Gamma_N = \frac{\Gamma_i - \Gamma_0}{\Gamma_0} \tag{2.6.1}$$

Considering $\Gamma_i = (\Gamma_+ + \Gamma_-)/2$, thus the normalized broadening to the initial hole width can be written as:

$$\Gamma_N = \frac{\Gamma_i - \Gamma_0}{\Gamma_0} = \frac{(\Gamma_+ + \Gamma_-)/2 - \Gamma_0}{\Gamma_0}$$

Figure 2-11 presents the broadening phenomenon in the function of E-field applied

axes and sites. Each data point in the curves are the average value from two or three independent measurement sequences. The averaged initial hole width Γ_0 is 6.7 kHz for D_1 Site 1, 4.9 kHz for D_1 Site 2, 8.1 kHz for D_2 Site 1 and 5.1 kHz for D_2 Site 2 when the cryostat temperature is stabilized at 3.2 K.

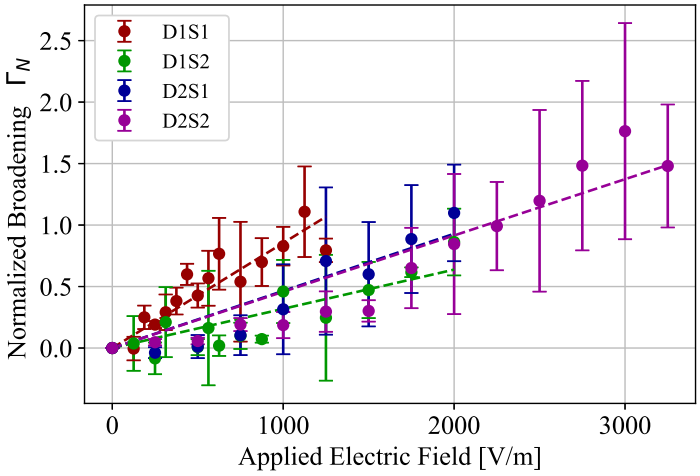

Figure 2-11: Normalized broadening as a function of applied electric field in Eu:YSO system. The normalization is referenced by the initial hole width. The dash line is a pure linear fit of the data.

The error bars in the data point are the hole's width variation from two or three sets of values from different measurements $\delta\Gamma_i$, making the error bars equals to $(\delta\Gamma_i - \Gamma_0)/\Gamma_0$.

2.6.2 Secondary Splitting of the Spectral Hole

Moreover, when an external E-field is applied on the crystal, the spectral hole will first split into two peaks separately, then by gradually increase the applied E-field strength, the split hole center shape will become less sharp showing a multi-hole overlapping structure in both left and right peaks. The spectrum where two peaks are superimposed in the left and right peak is then named as the secondary split spectrum. Since the overlapping structure may comes from the residual inhomogeneity

of the applied E-field, the secondary splitting of the spectral hole is another view of investigating the broadening.

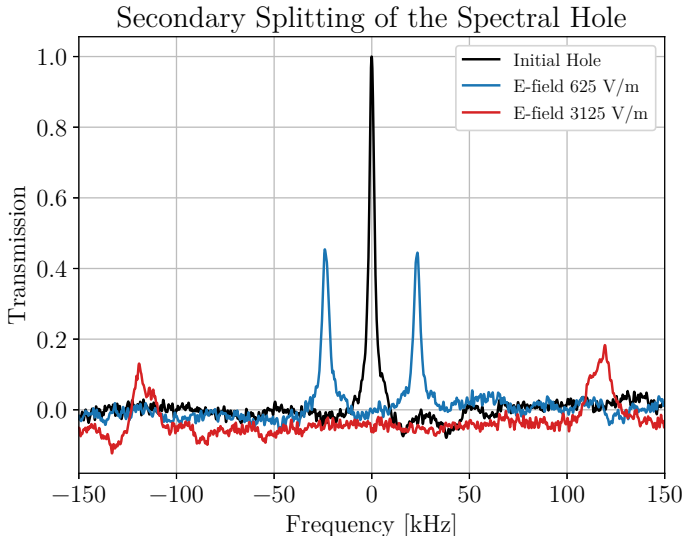

Figure 2-12: Secondary splitting of the spectral hole when the initial hole is burnt with the absence of the field with site 2 frequency. The E-field is applied along the D_1 direction. When the applied E-field is gradually increased, the left and right peak show a more observable secondary splitting phenomenon presenting in the red curve.

Figure 2-12 presents the spectra including the initial hole (black curve), holes with relative low E-field 625 V.m^{-1} (blue curve) and holes with relative high E-field 3125 V.m^{-1} (red curve). The initial hole is a typical Lorentzian peak, while the split holes with 625 V.m^{-1} applied E-field have a slightly asymmetric shape for both left and right peaks. When the E-field increase up to 3125 V.m^{-1}, an observable secondary splitting in the peaks shows up as it presents in the red curve.

Since the applied E-field is not perfectly along the D_1 or D_2 axis, there are always some E-field components along the perpendicular dielectric axes, making a tiny hole (side hole) nearby the desired narrow spectral hole pattern. When the E-field is increased, those inhomogeneity induced side holes shift gradually then making the multi-hole overlapping structure more and more show up. Therefore, the secondary splitting in the left and right peak can then be help to explain the broadening phenomenon of the spectral hole caused by the residual inhomogeneity of the E-field.

Future study of spectral hole E-field sensitivity along the b axis will be helpful to understand the spectral holes broadening behavior.

2.7 Conclusion

We have studied the Stark effect of spectral holes in Eu^{3+}:Y_2SiO_5 in a high precision measurement. The presence of an external electric field will make the spectral hole exhibit a symmetric splitting first, then with the gradually increased E-field strength the split peaks will shift to opposite direction.

The linear frequency shift of the spectral holes provides the symmetric and asymmetric linear Stark coefficients for both sites when the external electric field is applied along the D_1 or D_2 axis. The D_1 site 1 is the most sensitive axis with the symmetric linear coefficient of 271.8 Hz.m.V^{-1}. Our result is consistent with the previous measurement and provide a higher precision in the linear Stark coefficient.

The asymmetric quadratic effect is the most important study that describes how the fluctuation of E-field will affect the laser frequency stabilization when the laser is stabilized by locking on the narrow spectral pattern. An upper limit is added in the obtained asymmetric quadratic Stark coefficient, which makes it possible to estimate the desired experimental environment in spectral hole burning technique. A relative frequency stability of 10^{-17} at 1 s then requires the E-field instability to be below 2.3 V.m^{-1}. In metrology applications, the asymmetric quadratic stark coefficient is an important information when the electric field is a source of noise.

The symmetric quadratic effect is a deviation of the linear Stark effect. Even though it will not have influence on laser frequency stability when the laser is locked on the symmetrically split hole, the symmetric quadratic coefficient is still an useful parameter to characterize the rare earth ions used in spectral hole burning technique.

The broadening behavior of the spectral holes may comes from the E-field residual

inhomogeneity. The future Stark study in b-axis will probably help us to understand more about the broadening phenomenon in D_1 and D_2 axis, paving the way of the further study of rare earth ions characterization.

Chapter 3

The Effect of Uniaxial Stress on Spectral Holes in Europium Doped Crystals

The mechanical characterization of the rare earth ions can not only help obtaining a deeper understanding of the spectral hole burning technique, but also provide idea in optimizing the spectral hole burning environment which is useful in the application of laser frequency stabilization. This chapter describes the spectral hole's response to an externally applied uni-axial stress on the crystal, including the stress generation and distribution, spectral hole linear displacement in frequency and linewidth broadening due to the applied stress. The corresponding results have been published in our recent work [6, 51].

3.1 Stress Sensitivity of Spectral Holes

In the host Y_2SiO_5 (YSO) matrix, europium ions substitute the yttrium ions in two different crystalline sites as described in Ch. 1. Since europium ions have a larger

size than the yttrium ion, after doping the Eu^{3+} stochastically in the host YSO crystal, the crystal matrix deforms in an irregular manner, resulting in a different local environment for each single ion. In this way, by applying an external stress on the crystal, europium ions located in different positions will experience different distortions of their environment due to the stress, resulting in corresponding changes in energy levels. The spectral hole, which is at the resonant frequency of the optical transition from the $^7F_0$ state to the $^5D_0$ state of Eu^{3+} ions, will be affected by the applied stress correspondingly. The spectral hole burned in the Eu:YSO crystal has a long lifetime which allows the recording of the photo-imprinted spectral pattern, making it possible to investigate the europium ions mechanical properties through the spectral hole burning technique.

Motivation

In order to develop ultra-stable lasers through spectral hole burning technique, it is necessary to study the mechanical properties of Eu^{3+} ions, depending on which the effect of mechanical vibration on the laser frequency stability could be minimized. There are indeed some possible vibration noise sources in the system, such as the mechanical vibration caused by the pulse tube of the cryostat. In this chapter, we use measurements of the sensitivity to uniaxial stress to study the mechanical properties of europium ions, which will be described in detail in the following sections. The estimated sensitivity can provide information about the optimization of the crystal mounting with less vibration, shedding light on how to improve laser frequency stability.

Phenomenon

When an external stress is applied to the crystal, the spectral hole will undergo a displacement in frequency compared with the frequency of the initial hole. In our study, we first investigated the relationship between the center frequency shift of spectral hole and the applied stress. In addition, we have also observed that with the gradual increase of the stress amplitude, the linewidth of the spectral hole will

slightly broaden. Therefore, the broadening of the spectral hole has also been studied in this chapter.

Previous Studies

Previous studies about the spectral hole stress sensitivity is described in the work of Thorpe 2011 [28], that uses a set-up in which the Eu:YSO crystal is surrounded by cold helium gas in a vacuum chamber. The control of the applied isotropic pressure can be achieved by changing the gas pressure. The spectral holes centre frequency shift is described as *isotropic pressure sensitivity*, with the linear coefficients of -211.4(4) Hz.Pa^{-1} for site 1 and -52.0(7) Hz.Pa^{-1} for site 2.

For precision measurements, using the narrow spectral hole in the Eu:YSO crystal as a frequency reference, the uni-axial stress sensitivity of Eu^{3+} ions is important for inferring or predicting mechanical vibration caused modifications in the rare earth ions. Therefore, apart from the isotropic stress sensitivity, the *uniaxial stress sensitivity* of Eu^{3+} ions is also important to quantify, so that the frequency fluctuations caused by uniaxial mechanical vibrations can be characterized along different crystal axes. It should be noted that in the previously mentioned publication, Thorpe et al. have given estimation of the sensitivity of their setup to uniaxial acceleration. The work presented in this chapter is, however, fundamentally different, since in their case, they are considering an *effective* sensitivity of the whole setup, which largely depend on the crystal geometry and mechanical mounting they have used, whereas this chapter describes the measurement of an *intrinsic* property of the crystal.

In this chapter, a set of calibrated weights is employed to create experimental uniaxial stress, and the detailed information is given in Sec. 3.2. We also describe techniques to help get a better homogeneity of the applied stress field, such as the applied weights positioning (Sec. 3.3.1) and the application of YSO powder (presented in Sec. 3.3.2). Finally, the uniaxial stress sensitivity coefficients are deduced from experimental measurements (Sec. 3.4), and the broadening phenomenon is also discussed (Sec. 3.5) for each substitution sites and for two of the three dielectric axes of

the crystalline material.

3.2 Experimental Set-up

In this experiment, the cryostat temperature is stabilized at 3.15 K (see details of cryostat temperature stabilization in Ch. 1). As in the previous chapter, the optical beam propagates along the b axis and is polarized along the D_2 axis, which is the configuration exhibiting the largest absorption, and is therefore the most favorable for high precision spectroscopy and laser frequency stabilization [40, 52].

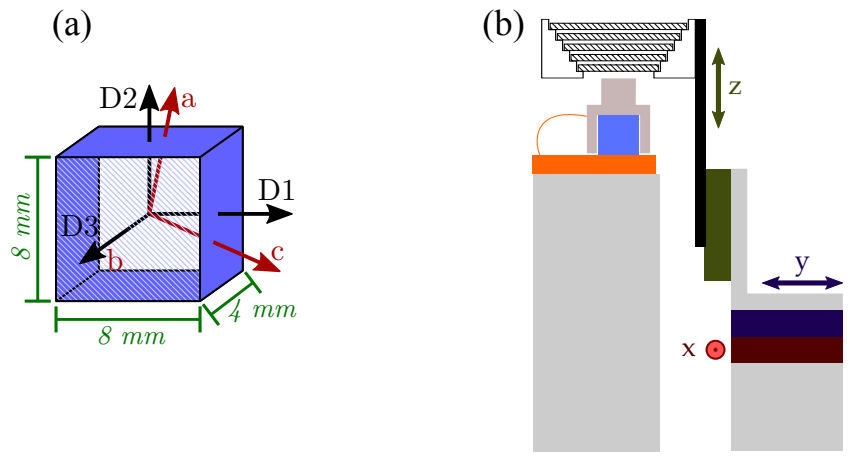

Figure 3-1: Experimental set-up for the stress measurement. In (a) the dimensions of our Eu:YSO crystal are shown. (b) represents the set-up used for depositing the weights on top of the crystal with the help of the motorized piezo translation platforms.

Five calibrated rectangular aluminum plates are employed as weights in our measurements as is shown in Fig. 3-1 (b). The weight of each sheet is 0.39 g with an uncertainty of 10% in the mass. Converting to the applied pressure on the 4 mm $\times$8 mm contact surface area, the corresponding applied pressure for one weight is 120 $\pm$ 12 Pa.

The weights are mounted on an aluminum holder, which is designed in a stair shape with a physical separation distance between each stair. The weights holder is

driven by a motorized piezo translation platform (see details in Sec. 3.3.1), which is movable along x, y, z direction as shown in Fig. 3-1. When depositing the weights along the vertical direction (z direction in Fig. 3-1), the desired number of weights can be applied on the crystal, while the other weights stay on the stair-shaped holder. This way, we can apply a controllable force on the crystal by placing a certain number of weights on top of the crystal. Moreover, the adjustment of weights position can be achieved by moving the weights holder in the xy plane. More details can be found in Sec. 3.3.1.

Our crystal has four unpolished faces (only the beam propagating facets are polished), and one of the unpolished crystal face is the contact interface with the applied weight.

To avoid the stray electric field effects in the measurement, as well as improve the reproducibility of the strain effect when depositing the calibrated weight, an aluminum cover, which is referred to as the "crystal hat", is placed on top of the crystal and electrically grounded. The top surface of the crystal hat is designed to have the same area as the top surface of the crystal. As the weight are deposited on this crystal hat and not on the crystal itself, the surface of the crystal by which the strain is applied is that of the hat, which is a better quality and flatness that can be achieved for the weights.

The homogeneity of the applied stress field is one of the main challenge in this experiment. Some technical considerations, including the optimization of the experimental set-up and operation precautions of the measurements, can be helpful to get better homogeneity of the applied stress field. The details are presented and discussed in the following section.

3.3 Uni-axial Stress Homogeneity

The external uni-axial force applied on the crystal will cause the deformation of the crystal matrix (strain) and form a stress field. From a macroscopic point of view, the spectral hole, which we used to investigate the mechanical properties of europium ions, is the collective behavior of an ion ensemble identified by their resonance frequency. A homogeneously distributed stress field will help to achieve a consistent effect over all the ions which participates in the spectral hole. Therefore, it is crucial to optimize the homogeneity of the stress field, as we will discuss in the following. This section presents the technical considerations related to obtaining a more homogeneously distributed stress field on a macroscopic scale, including the application of calibrated weights, contact surface roughness, probe beam characteristics. It also describes the necessity of checking for thermalization of the crystal, in order to make an accurate measurement not biased by thermal effects.

3.3.1 Applied Weights Positioning

The relative position of the weights with respect to the crystal is important in terms of the stress field homogeneity. The weights and crystal are assumed to be homogeneously distributed in mass, so their center of gravity is equivalent to their geometric center (it is collectively referred to as the center here). If the center of the weight and the center of the crystal are aligned in the vertical direction, then the weight is well centered, which is required for achieving stress homogeneity.

Motorized Piezo Platform

During our first attempts of making such measurements, a one-axis movable weight holder was used, driven by a commercial piezo translation stage from SmarAct (model: MCS2). In that case, the weights could only move along the z-axis, while the xy coordinates are not tunable, depending totally on how the weights are initially set in

the top area of the crystal when establishing the set-up, as it shown in Fig. 3-2(a). With the employment of the one-axis movable platform, the frequency displacement of the spectral hole could be observed but not consistent for a certain value of applied stress, making the results unrepeatable. Moreover, asymmetric spectral holes sometimes would appear, and could be explained by the stress inhomogeneity coming from not-centered weights deposition.

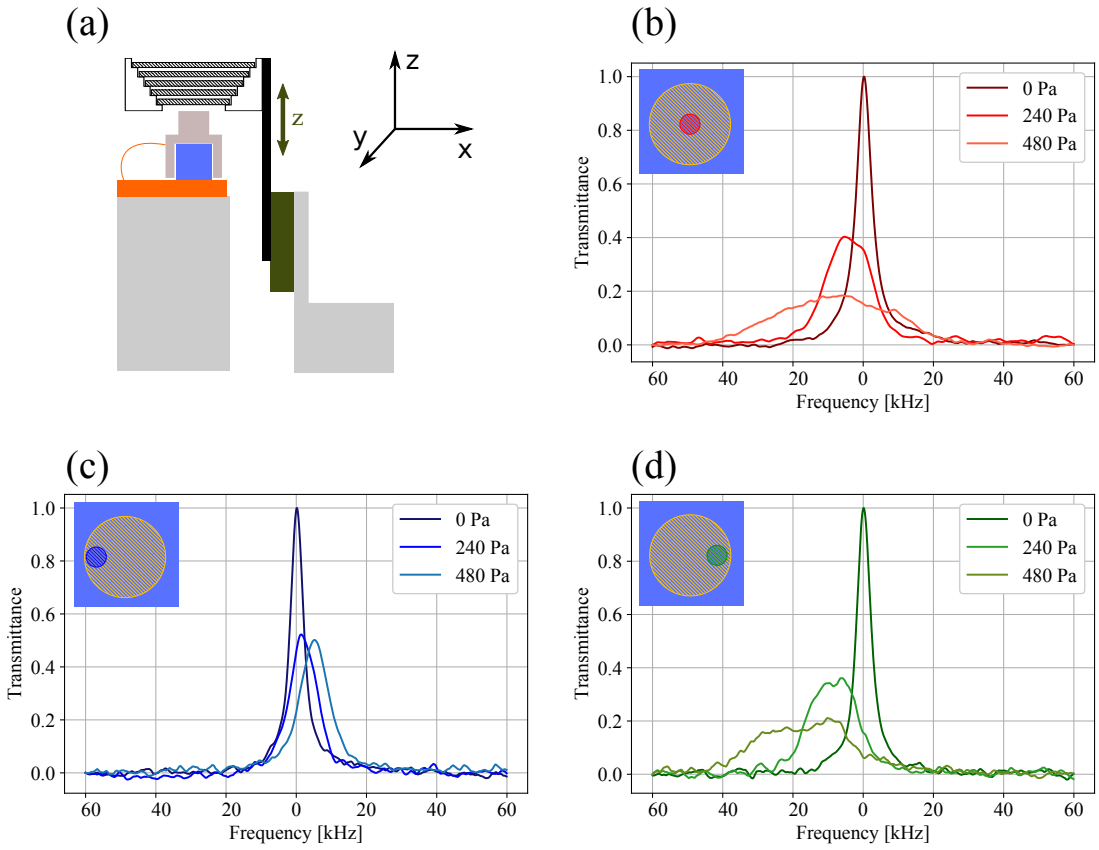

Figure 3-2: The set-up and spectra of a one-axis movable weights mounting. (a) shows the weights deposition along the z direction and center positioning in the xy plane. To investigate the homogeneity of the stress field with one-axis movable set-up, the initial hole is burnt with a large size of optical beam centered on the crystal. Then a small pinhole with diameter of 1.5 mm is employed to check the stress field homogeneity in space. (b) shows when the pinhole is positioned in the center of the crystal. (c) and (d) present the spectra when the pinhole crops the optical beam, making the small beam propagates through the extreme left and extreme right sides of the crystal respectively. The insets of (b), (c), and (d) illustrate the crystal (blue square), the initial beam position (large yellow circle), and the position of the pin hole (small colored circle).

To observe the inhomogeneity of the stress field, we probe different regions in the crystal to see if the spectral holes response differently. The initial hole was burned with a large optical beam, which has a diameter of 6 mm. A commercial iris diaphragm from Thorlabs was used to crop the beam to a smaller size (1.5 mm in diameter). The iris diaphragm then acts as a pinhole. Regardless of where the pinhole is located, a global uniformly distributed stress field will result in consistent spectral hole behavior. Conversely, a non-homogeneously distributed stress field will result in different responses from the spectral holes. By placing the pinhole in the center, left and right positions of crystal, we found that the spectral holes behave differently (see Fig. 3-2). First, with identical applied pressure (240 Pa and 480 Pa), the center frequency shift of the spectral hole varies with the probing position (see Fig. 3-2 (b), (c), (d)). Second, when the pressure is applied, the spectral holes sometimes have asymmetrical shape as it shows in Fig. 3-2 (b) and (d). Third, we observed some hysteresis in the initial shape of the hole when the weight are removed after being deposited, which could be interpreted as minute positioning displacement induced by imperfect centering of the weight. These are proofs of inhomogenity of the stress field, which come from the not-centered weights deposition. In this configuration, it was therefore difficult to obtain high precision reproduce experimental results.

In order to overcome the aforementioned weights centering problem, another two movable axes in translation stage were added, as the Fig. 3-1 (b) shows. A multi-functional piezo controller for closed loop positioner from Attocube (model: ANC350) is employed to move the weights in xy plane with a movement precision of 1 μm. Then the weights' relative position can be centered before depositing, and the well-centered position can be found by shifting the weights along the x or y axis. The signature of a well-centered position is that, first, the shape of the spectral hole is close to the Lorentzian profile in line-shape, and second, the spectral line displacement in frequency is consistent with a certain number of weights applied, and third, the shape of initial spectral hole can be recovered when the weights are reset. Once the result is repeatable, then the experiment can be carried out through the study of spectral

holes behavior in Eu^{3+}: Y_2SiO_5 system.

Effect of the Electrical Charges

In the first attempts at making this experiment, we observed that the spectral hole had irreversible changes,triggered by the movement of the motorized platform (even without actually depositing a weight on the crystal !). Even if the operation of the motorized platform returns to the initial state, the spectral hole still would still be modified compared to the initial Lorentz hole.

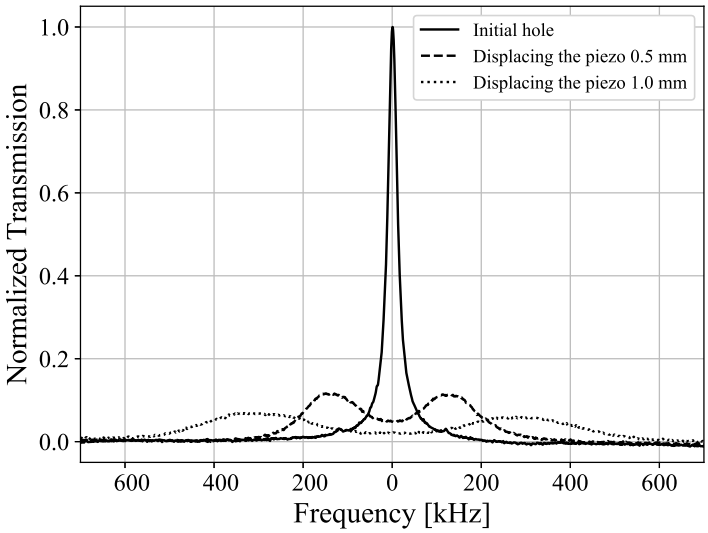

Figure 3-3: Electrical charge effect on the spectral hole profile. The initial hole is burnt without applied pressure (shown in the solid curve). By moving the piezo platform without depositing the weights on the crystal, the initial spectral hole is nevertheless deformed, as shown by the two dashed spectra.

In more detail, we observed that by burning the initial hole with the absence of the applied weights, then move the translation stage in one direction by 0.5 mm or 1 mm but without depositing the weights on the crystal, the spectral hole would afterwards exhibit a splitting structure as is shown in Fig. 3-3. Even if the translation stage is returned to the initial position, the spectral hole would keep the split shape and would not recover the initial shape.

We suspected that this irreversible split hole effect was in fact induced by external electric field created by electric charges emitted by the translation stage during its operation (the SmarAct translation stage operates by stick-slip piezo-actuation of a translation screw, which may be a process from which stray electric charges could be emitted if grounding is not sufficient). Since the spectral holes are not only sensitive to mechanical stress, but also to electric fields (as is described and accurately measured in Ch. 2), the change in the static electromagnetic field will affect the spectral hole.

We implemented several methods to eliminate the effect of uncontrolled electric fields. First of all, all the metal devices were grounded, including the crystal hat, weights holder and the piezoelectric translation stages. Second, a grounded aluminum-foil cover was used to surround the piezo translations stage as the photo shown in Fig. 3-4 (b). This conducting cover works as a shield for static electric fields, and a way to capture stray electric charges that may be emitted by the operation of the translation stage.

We have verified that with these methods applied, the aforementioned electric field uncontrolled effect was effectively suppressed. The verification is carried out, in particular, through the comparison of the spectral hole before and after every measurement run which includes operation of the translation stage. The recoverable hole shape proves that the electrical charge effect is a negligible disturbance after treatment.

3.3.2 YSO Powder Application

As mentioned in Sec. 3.2, the home-made crystal hat is designed and put on top of the crystal to improve stress homogeneity. The measurements carried out with the crystal hat still had some inconsistent hole behavior, such as asymmetrical shape, which are indications of residual inhomogeneity of stress field. Therefore the contact surfaces need to be further improved to get better global homogeneity of the stress

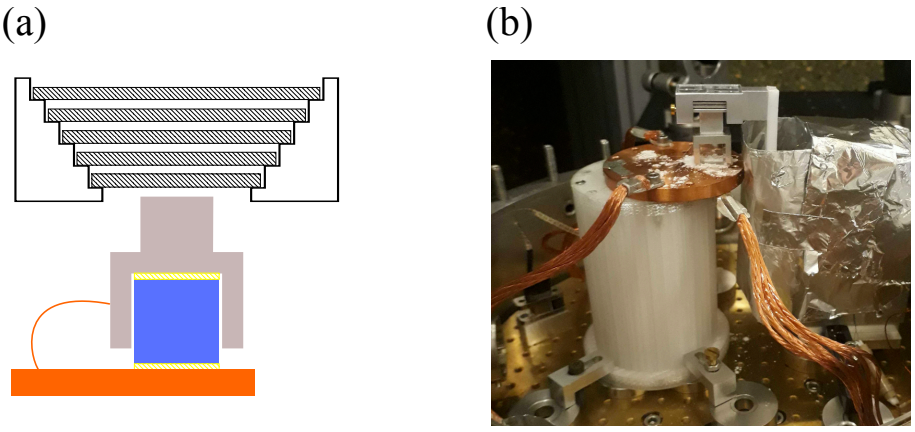

Figure 3-4: YSO powder application in the set-up showing in (a) as the yellow lines on right above and below the crystal. (b) is a photo of our strain measurement set-up, which is inside a vacuum chamber of closed cycle cryostat.

field.

We found that it was necessary to add, at the surface of contact (top and bottom) of the crystal, two thin layers of Yttrium Silicate (YSO) powder, depicted as the yellow lines in Fig. 3-4, which have micrometer-dimension typical grain size. The estimated thickness is below 1 mm (note: the YSO powder is white. The yellow color used here just to highlight the powder position).

The powder acts as a buffer layer, allowing the direct contact of the previous not perfectly flat surfaces to become an indirect contact through YSO powder grains. When two non flat surfaces squeeze each other, the actual contact area is much smaller than the apparent contact area as it shows in Fig. 3-5 (a), making the non-uniformly distributed stress field. The powder fills some of the gap between the contact surfaces as it presents in Fig. 3-5 (b), reducing the errors of planeity (contact surfaces), and making a bigger contact area between the weight surface and top surface of the crystal hat (also the copper plate and crystal bottom facet). Thus the YSO powder layer application can help to make a more uniformly distributed distortion of the crystalline matrix, avoiding the inhomogeneity in the stress field.

Figure 3-6 shows the effect of powder on the spectral hole. If the measurements are done without powder, the obtained spectrum varies from scan to scan. The

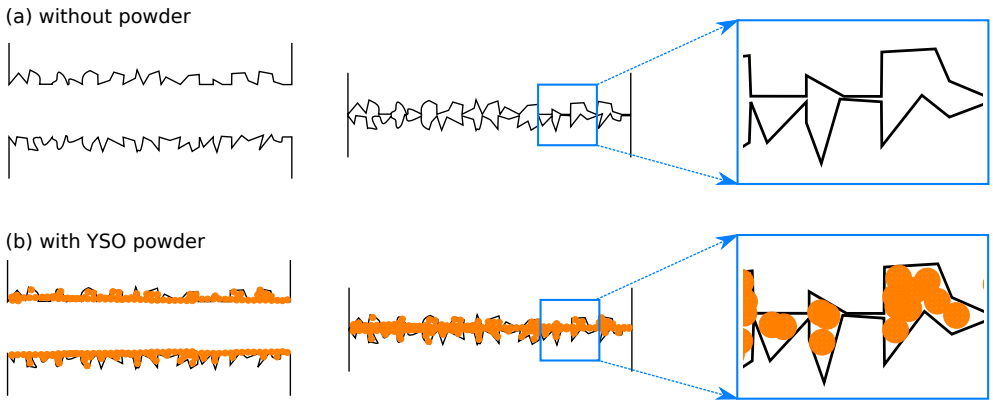

Figure 3-5: Contact surfaces with and without powder. (a) When the two non flat surfaces contact each other, the real contact area is sometimes point-to-point or point-to-gap contact, making the applied pressure nonuniformly distributed in the crystal. (b) The yellow small dots represent the YSO powder grains with micron size. The YSO powder can fill in the gaps in between two surfaces, reducing the errors of planity and lead to a more uniformly distributed pressure.

dashed curve presenting in Fig. 3-6 is one example spectrum of the without powder measurement, in which the obtained spectrum showing a overlapped double-peak structure. If the measurements are done with two thin layers of YSO power applying on the top and bottom of the crystal, the recorded spectrum is Lorentzian, which is expected. When depositing the weights on the crystal, the spectral hole is a center frequency shifted Lorentzian profile, and the shape can be recovered when the experimental condition is restored. In addition, a number of independent measurements have confirmed that under a certain applied pressure, the spectral hole displacement in frequency is constant, making it possible to experimentally study the europium ions mechanical properties in our system.

Thermalization of the Crystal

The Eu:YSO crystal is mounted on the top of a cylindrical copper pedestal in thermal contact with the cold plate. The crystal hat is also in thermal contact with the copper pedestal. The temperature stability of the crystal firstly depends on the environmental temperature change, and secondly depends on the efficiency of thermal transfer. So the heat radiation from the crystal positioning environment and the heat

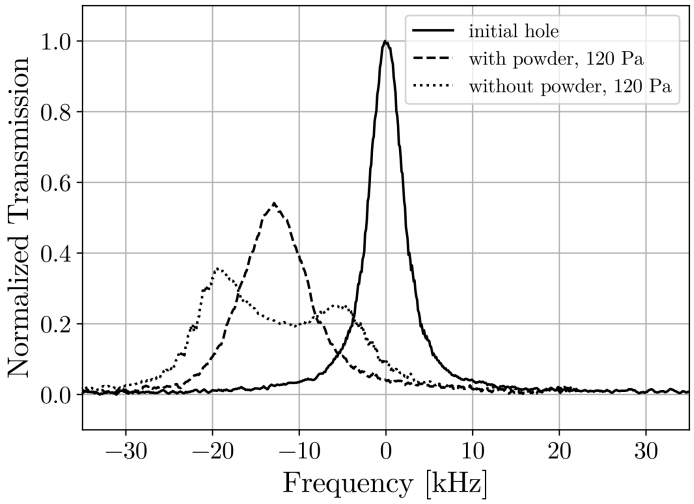

Figure 3-6: Spectra showing the effect of the YSO powder. The solid line is the initial hole burnt with Site 2 frequency without pressure applied. The two dashed lines show the spectra with one weight applied along the D_1 axis of the crystal, corresponding to 120 Pa in pressure.

exchange through the top and bottom YSO powder layers are two main factors that bring the crystal to cryogenic temperatures.

We realized that the silver lacquer, which is typically used to get better thermal contact between the crystal and copper pedestal, will add external stress on the crystal at cryogenic temperature, thus making the stress field unpredictable and spectral holes behavior toward the uni-axial stress unrepeatable. So the silver lacquer is not used in these measurements.

The application of YSO powder does help us improve the stress field homogeneity, but the price paid is that the efficiency of thermal contact between the crystal and the cold chamber of cryostat is low, which makes it take longer for the crystal to reach the target temperature.

Because the resonant frequency of the ions in the crystalline matrix is sensitive to the temperature, if the crystal temperature does not reach a steady state before a measurement, the temperature changes of the crystal will modify the position of

the spectral hole, making a high precision measurement problematic. Therefore, it is necessary to optimize the thermalization of the crystal, in order to let the investigated spectral holes modification be completely derived from the uniaxial stress.

The optical beam used for probing the crystal has a heating effect when propagating through the cryostat. Therefore it is important to employ a proper optical beam power intensity in order to have lower thermal fluctuations. In the first attempts at making this measurements, both our master laser and slave laser were sent to the cryostat passing through the crystal, then the beat-note between the master laser and slave laser was detected by a silicon amplified photo-detector (model: ET-2030A) from EOTECH (see details in Ch. 1). Considering the master laser contains around 1 mW in optical power, in order to minimize the optical beam induced thermal fluctuations, we remove the master laser in the optical path of going through the crystal. The double pass AOM helps us to generate two modes in the slave laser with 100 nW for each mode, separated by 800 kHz, then the beat-note between those two modes is detected by an avalanche photodiode from Thorlabs (Model: APD 410A). Moreover, the power of the beam is stabilized by a homemade servo loop (see details in Ch. 1).

We have measured the time constant for the crystal to get the thermalized state. By blocking and releasing the optical beam, and recording the corresponding spectral pattern for different waiting time, the spectral holes evolution can be recorded. Because of the heating effect coming from the optical beam, the spectral hole has its center shitted, before the crystal reaches a constant temperature. Once the crystal reaches the target temperature, the spectral hole position in frequency domain remains un-changed. The data points in Fig. 3-7 are the measured spectral hole frequency shift as a function of time interval between the beam releasing instantaneous time and the scanning time of the investigated hole. Then the data is fit with an exponential model

$$\delta f = a \times e^{-t/\tau} + \text{offset}$$

where is the corresponding time constant with the unit of second. The fitted time

constant value is around 1 min for the probe laser with 2 mm diameter and 200 nW in power.

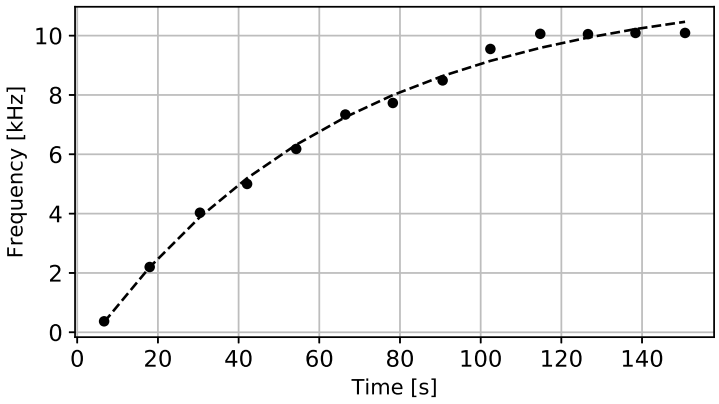

Figure 3-7: Optical Beam heating effect on the spectral hole. The x axis is the duration right after the optical beam is released to go through the crystal. The y axis is the spectral hole center frequency shift compared with the first scan of the initial hole. The time constant to get the steady state is around 1 min.

As mentioned previously, the piezoelectric translation stage used for depositing the weights on top of the crystal also has a heating effect when it is actuated. Combining the optical beam heating effect and translation stage heating effect, the final chosen waiting time in between each measurement is 5 min, which is sufficient for spectral holes to reach the terminal state for each experimental operation.

In addition, a frequency comb is used in our measurement continuously to eliminate the frequency drift from the reference cavity (see details in Ch. 1.3.3), even though it turns out that the reference cavity induced laser frequency drift is negligible in the measurement. A verification scan of the initial hole is done for every set of the measurement, verifying that the relative frequency position of the initial hole is constant and repeatable.

3.4 Spectral Hole Linear Displacement in Frequency due to the Applied Stress

This section focuses on the spectral hole frequency shift due to the external stress. The center shifted spectral pattern is modeled and analyzed for different axes and sites, depending on which the stress sensitivity coefficient is obtained and spectral hole strain sensitivity is then deduced.

3.4.1 Positive and Negative Pressure

In the measurement, the positive and negative pressures are artificially defined to systematically study the spectral hole behavior in Eu:YSO crystal. For the relative positive pressure, the initial spectral hole is burnt without weight deposited on the crystal. Then by adding weights one by one on the crystal, the positive force increases, resulting in a gradual increase in positive pressure.

For the relative negative pressure, the initial spectral hole is burnt when all weights are placed on top of the crystal. By reducing the number of applied weights, a relatively negative force is generated. Thereby, the absolute value of negative pressure can be gradually increased artificially.

For a certain axis along which the weight is deposited, the positive and negative pressure will make the same amount of center frequency shift of spectral holes, but in the opposite direction. For the same magnitude of positive pressure or negative pressure can be gradually increased artificially. Our studies include both positive and negative pressure measurements in the investigation of the mechanical properties of europium ions, and the following sections describe the relevant details.

3.4.2 The Consistency of Spectral Hole Behavior

In our quantitative measurements, it is important to check for the consistency of the spectral holes response under certain conditions, in order to make sure the results are reliable and repeatable. The consistency tests are carried out from two aspects of consideration, including consistence in different crystal positions (spatial consistency), and with respect to different frequencies which means the spectral hole is burned with different frequency making the hole structure print in different positions in the absorption spectrum of europium ions.

Spatial Consistency

Since the stress field distribution in the crystal is not perfectly homogeneous, the spatial consistency test is to see if the spatial inhomogeneity induced effects on spectral holes are negligible in our study. The spectral hole profile reflects the collective behavior of a number of Eu^{3+} ions. If the average response from europium ions located at the different crystalline locations is uniform response toward the applied stress, then the central shift with a certain applied stress is considered to be constant, therefore the sensitivity coefficients can be measured experimentally.

In the spatial consistence test, the initial hole is burnt with a 6 mm diameter Gaussian beam, without applied stress. Then a beam spot with diameter of 2 mm is employed by cropping the optical beam with an adjustable iris diaphragm, which is relatively small compared with the initial hole probing beam size and crystal geometry (beam propagating facet is a 8 mm $\times$8 mm square surface). By depositing one weight on the crystal and changing the position of the probe light, the ions located in different probe volume will give response to the pump laser, reflecting the stress field residual inhomogeneity effect on the holes behavior. Therefore, we can study whether the Eu^{3+} ions in different positions of the crystal react differently to the applied stress.

The spatial consistency measurement of the spectral hole is done by probing the europium ions at 5 different positions in the crystal (center, top, bottom, left and

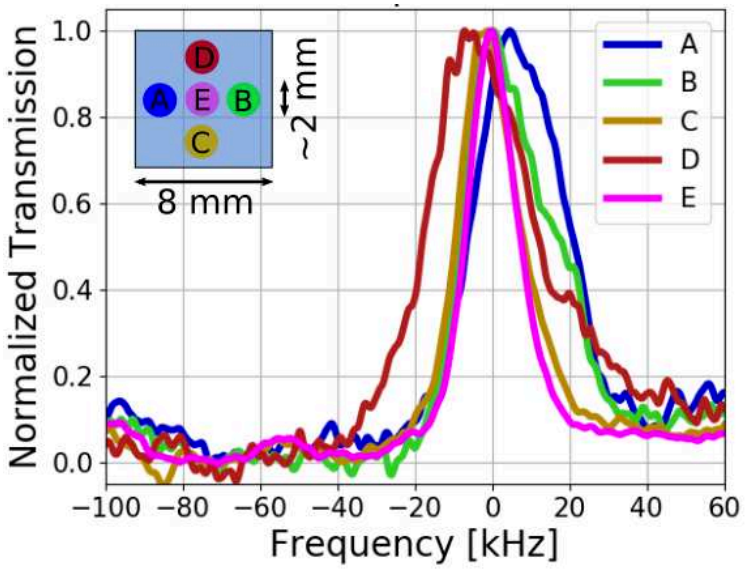

Figure 3-8: Spectral hole profile when the optical beam probes different locations inside the crystal with 120 Pa pressure applied along D_1 axis. The inset shows the position of the incident probe beam on the crystal's xz face, which is perpendicular to the direction of beam propagation.

right). Figure 3-8 is an example of applying 120 Pa pressure on the crystal, the spectral holes have almost the same center frequency position and linewidth in all the 5 cases, reflecting that the resonate frequencies in those 5 spatial positions are almost the same. Moreover, no matter where the probe position is, with a certain applied stress, the frequency shift of the spectral hole is constant within measurement uncertainty. For instance, the 120 Pa allied pressure along D_2 axis will make the initial hole burning with site 2 frequency has around 25 kHz center shift. Therefore, the spatial consistency of the spectral hole behavior with the uniaxial stress can be concluded.

Consistency with Regard to Frequency

As mentioned in Ch. 1, europium ions exhibit an inhomogeneously broadened absorption spectrum with 2 GHz linewidth at FWHM for our crystal (0.1% doping level). In this regard, most of the time, our measurements are carried out when the narrow spectral hole is imprinted in the vicinity of peak absorption. In order to verify the consistency of spectral hole behavior with regard to frequency, our laser frequency

is tuned to the left and right part of the inhomogeneously broadened absorption profile as it shown in Fig. 3-9.

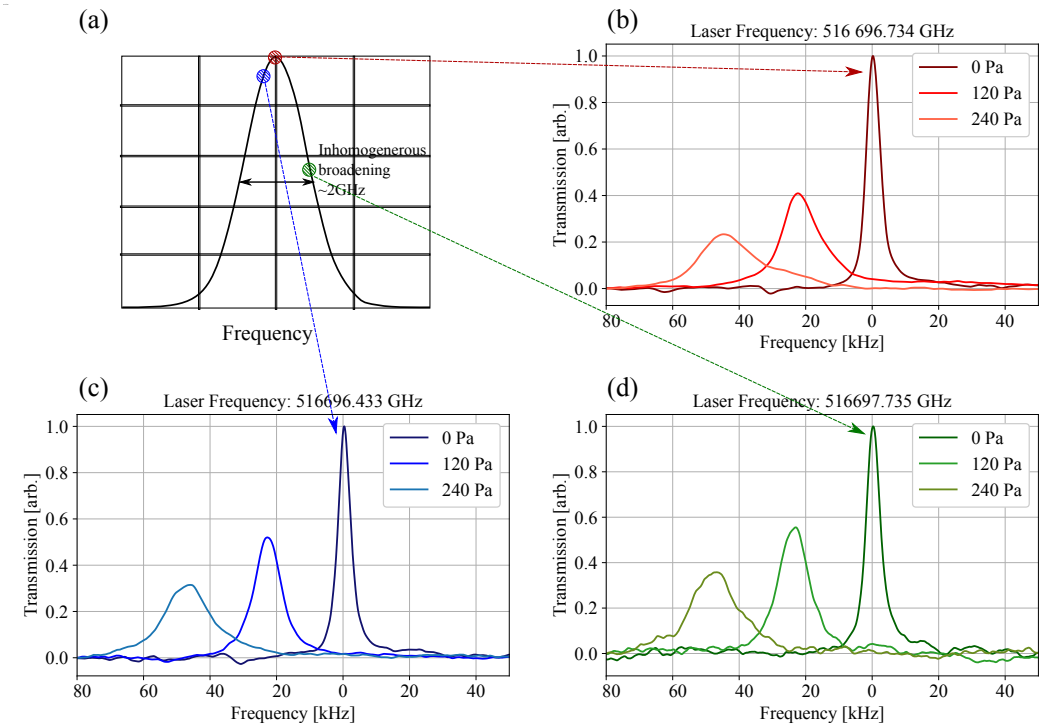

Figure 3-9: Consistency of spectral holes' behavior with regard to frequency. The inhomogeneously broadened absorption spectrum of Eu^{3+} ions around the site 2 frequency is presented in (a). The dots are showing initial hole burning frequencies in this measurement. The initial spectral holes are burnt with different frequency values, shown in (b), (c) and (d) respectively. When the external stress is applied parallel to the D_2 axis, the spectral holes have similar response to the stress. For instance the 120 Pa applied stress will cause a frequency shift around -25 kHz for all three cases.

The different frequencies nearby the site 2 frequency are chosen to perform three sets of measurements. The pump laser frequency is tuned to 516 696.734 GHz, 516 696.433 GHz and 516 697.735 GHz to burn the initial holes, in order to compare stress induced response of Eu^{3+} ions which resonating frequency is at the center, left and right parts of the absorption spectrum.

By depositing a certain number of weights on the crystal, the initial holes have constant frequency shift for all the three cases. This means the stress sensitivity is the same for europium ions resonating with different frequencies for the same site.

As a conclusion, the spectral holes burnt in different parts of the inhomogeneously broadened profile have the same tendency in collective behavior with the applied stress.

3.4.3 Spectral Holes Response toward the Uni-axial Stress

If an external stress is applied on the crystal in the elastic regime, the corresponding deformation in the crystal matrix is proportional to the stress strength. Therefore, the resulting modification of the crystal matrix can be seen through the europium ions absorption spectrum. In our experimental observation, when the external stress is applied, the spectral hole exhibits not only a displacement in frequency, but also a broadening of its linewidth. We first characterize the center shift of the spectral hole. This study is presented in Sec. 3.4.4. In a second step, we study the broadening effect, which is presented in Sec. 3.5.

The measurements along D_1 or D_2 axis were done by turning the crystal by 90°. Considering the two identical substitution sites of Eu^{3+} ions in the crystal, the study also contains the measurements with site 1 and site 2 frequencies. Figure 3-10 is the example spectra of spectral holes responses to the applied stress. Gradient colors in Figure3-10 are used to present the strength of the applied stress and also indicate the positive and negative pressure. The investigation of stress sensitivity of the spectral hole is discussed in the following sections.

3.4.4 Linear Frequency Shift

In the experiment, a frequency comb is used continuously to monitor our laser frequency, in order to remove the reference cavity drift induced laser frequency fluctuation. In addition, at the end of each measurement, a verification scan of the initial hole is done to check for any systematic bias in frequency. With this experimental protocol, we observe that both of these two effects are negligible in the stress

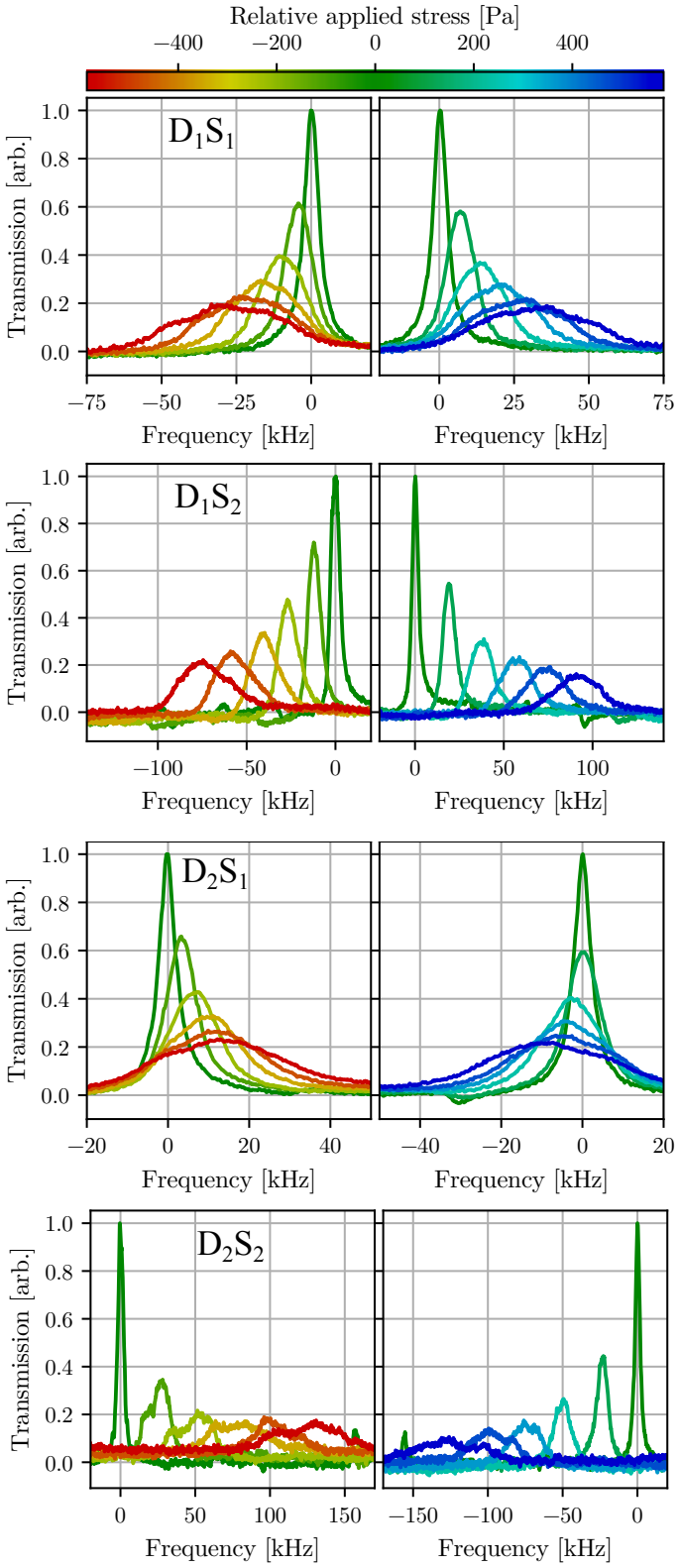

Figure 3-10: Spectral holes profile as a function of applied stress. The initial spectral hole is burnt with site 1 or site 2 frequency when the crystal temperature is stabilized at 3.15 K. The external calibrated force is applied along the D_1 or D_2 axis.

sensitivity measurement compared to the measurement error bar.

Linear Model

The initial spectral hole has a single-peak shape, so it is modeled by a Lorentzian function, and the center frequency position is noted as f_0 which is used as a reference to deduce the relative frequency shift of spectral holes. The experimental sequence of the measurements is noted as i according to the serial number. The center frequency of each spectral hole is symbolized as f_i to redefine the shifted center position. The linewidth at FWHM (Full Width at Half Maximum) is symbolized as Γ_0 for the initial spectral hole and Γ_i for the i_{th} scanned spectral hole. Therefore, each transmission spectrum is modeled by the Eq. 3.4.1.

$$T(f) = A_i + \frac{B_i}{1 + \frac{4(f - f_i)^2}{{\Gamma_i}^2}} \tag{3.4.1}$$

The measurements are carried out by burning the initial hole in the absence of the applied stress and with all the weights applied on the crystal to perform the positive and negative stress measurements respectively, as was mentioned in Sec. 3.4.1. The spectra are shown in Fig. 3-10 for different axes and sites.

With the positive stress applied, the spectral hole center frequency will shift to one direction first. Then the gradually increased magnitude of the positive stress will shift the spectral hole more in that direction. If a negative stress is applied along the same dielectric axis, the center of the initial hole will frequency shift to the opposite direction. As the applied negative stress magnitude increases, the frequency shift value also gradually increases.

Since in the linear regime the deformation of the crystal is proportional to the applied stress, the peak movement exhibits a linear behavior. In the study of spectral hole linear displacement in frequency, the relative frequency shift of each peak $\delta f =$

$f_i - f_0$ is then modeled by a pure linear function

$$\delta f = \kappa \times P.$$

The applied pressure is then presented as P in the fitting model with the unit of Pa, and the acceleration of gravity is taken as 9.807 m.s^{-2} in the calculation of the applied pressure. The linear slope κ is the stress sensitivity coefficient in the unit of Hz.Pa^{-1}.

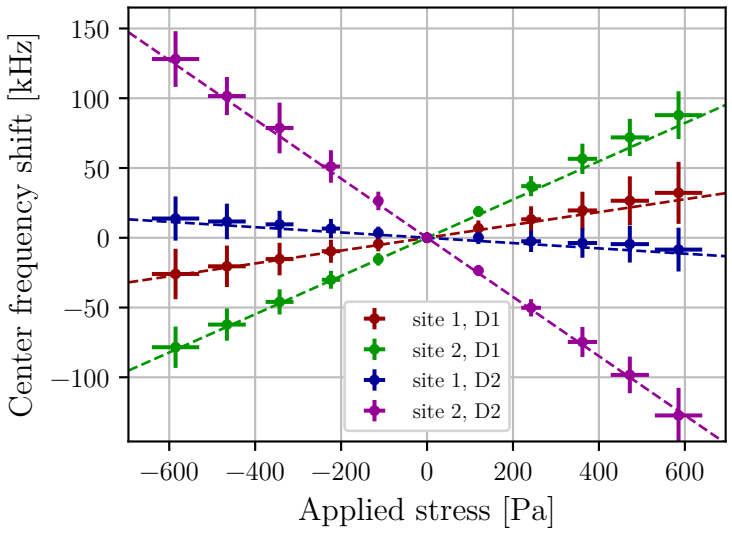

Figure 3-11: Linear frequency shifts of spectral holes as a function of applied stress. The external stress is applied parallel to the D_1 or D_2 axis. The initial spectral holes are burnt with site 1 or site 2 frequency when the temperature is stabilized at 3.15 K.

Figure 3-11 shows the linear frequency shift of the spectral holes as a function of the crystalline axes and substitution sites. Since the positive and negative applied stress measurements are two independent measurements, at the beginning of our investigation, the frequency shift caused by the positive and negative stresses is studied separately. According to the preliminary analysis, the positive and negative applied stress have almost the same trend and linear slope (difference $< 5\%$) in the frequency shift. Consequently, for a given axis and site, frequency shifts caused by the positive and negative stresses are combined into one data sequence and fitted by one linear

model. The dashed line in Fig. 3-11 is the fitted linear model for the combined data.

Error Bars for the Data Points

The error bar of the data point in Fig. 3-11 contains two parts: the vertical and horizontal error bars. The vertical error bars present the frequency shift uncertainty, and are defined as the full width at half maximum of each peak $\delta f_{\text{vertical}} = \Gamma_i$. The fitting uncertainty of center frequency δf_i and the spectrum alignment uncertainty (around 100 Hz) are small compared with the linewidth of each individual peak, so they are negligible in the definition of vertical error bars. We have chosen here to give a somewhat conservative uncertainty equal to the linewidth of the peak. The rationale behind this (partially arbitrary) choice is that the peaks have, in some cases, a discernible change in overall shape, which may be attributed to residual experimental problems (such as otherwise unaccounted for inhomogeneity of the applied stress tensor field). Using a conservative error bar definition accounts for such effects. One may notice that the error bar definition we have used when studying the electric field effect is smaller (we have used there one tenth of the linewidth), reflecting the lower level of hole shape deformation in this separate study.

The horizontal error bars of the data point in Fig. 3-11 presents the applied stress uncertainty, which is mainly coming from the estimated inhomogeneity of the stress field (in direction and amplitude). In addition, uncertainties in the weight mass (δm = 0.01 g) and crystal dimension (cutting uncertainty $< 0.5°$) are negligible here.

Axis	Site	Hz.Pa^{-1}	THz.Strain^{-1}	g^{-1}
D_1	1	46 ± 17	6.2 ± 2.3	(15.3 ± 5.6) × 10^{-12}
D_1	2	137 ± 16	18 ± 2.2	(45.5 ± 5.4) × 10^{-12}
D_2	1	-19 ± 10	-2.6 ± 1.4	(-6.4 ± 3.3) × 10^{-12}
D_2	2	-213 ± 13	-29 ± 1.8	(-70.8 ± 4.3) × 10^{-12}

Table 3.1: Europium ions strain sensitivities in a YSO host matrix, when stress is applied parallel to the D_1 or D_2 crystalline axes, and for crystal site 1 or 2.

Error Bars for the Linear Coefficient

Table 3.1 is the summary of the linear stress sensitivity coefficients corresponding to the curves in Fig. 3-11. The tabulated linear coefficients have two main components in uncertainty. The first is from the fitting algorithm, which is the linear slope uncertainty stems from the combination of the square roots of the relevant diagonal elements of the covariance matrix for each fit. Second is from the repeatability of the measurement (standard deviation of κ from several independent measurements under same condition). Therefore, the stress sensitivity coefficients of our crystal in the unit of Hz.Pa^{-1} are presented in the third column of the Tab. 3.1, which is the direct deduction from the applied pressure.

To compare our results with that obtained for different crystalline materials, it is useful to express the sensitivity in terms sensitivity per strain, which is independent of the stiffness of the crystal. Therefore, the stress sensitivity in the unit of THz.Strain^{-1} is also provided in our measurement using a Young modulus for YSO of 135 GPa. So the stress sensitivity coefficient κ presenting in the third column of Tab. 3.1 are multiplied by 135 GPa.Strain^{-1} and the obtained value is tabled in the fourth column of Tab. 3.1. The stress sensitivity per strain make it possible to compare different systems from a microscopic point of view.

3.4.5 Acceleration Sensitivity of Europium Ions in YSO Crystal

The spectral holes we investigate have an intended application in metrology where they can be used as frequency references for frequency stabilization of ultra-stable laser. In this context, expressing the acceleration sensitivity of the spectral hole in our crystal is particularly relevant as it allows comparisons with that of other systems used as frequency references, such as high finesse Fabry-Perot cavities.

The acceleration sensitivity is often sited in g^{-1}, where g is the acceleration of gravity. In our case, consider the pressure generated by the weight of the crystal

$m_{\text{crystal}}g$ (m_{crystal} = 1.1 gram, g = 9.807 m.s^{-2}), acting on the surface area of S = 8 mm $\times$4 mm, the acceleration sensitivity κ in the unit of Hz.Pa^{-1} can be converted into κ in g^{-1} via

$$\frac{\kappa_{g^{-1}}}{g} = \frac{\kappa_{Hz/Pa}}{f_{\text{laser}}} \times \frac{m_{\text{crystal}}}{\text{S}}.$$

where f_{laser} is the laser frequency. The corresponding coefficients for each axis and site are tabulated in the last column of Tab. 3.1. The obtained acceleration sensitivity of the spectral hole in a 8 mm $\times$8 mm $\times$4 mm crystal is between 7 $\times 10^{-12}$ to 7 $\times$ 10^{-11} per g in terms of the most and least sensitive axis and site.

Therefore, in our system, the acceleration sensitivity of the spectral hole is comparable to the one of typical Fabry-Perot cavity, which is around 10^{-12} per g in the recently reported reference [53]. However, it must be observed that such Fabry-Perot cavities are designed with a highly optimized and well engineered mounting and shape, which produces a comparatively low overall acceleration sensitivity. In our case, the crystal in our system is simply put on top of a copper pedestal with to shape or mounting mechanism optimization. There is a lot of space to improve the crystal mounting, such as holding the crystal along the less acceleration sensitive axis or using first-order sensitivity cancellation mounting designs (by holding the crystal by the middle along a given direction, under the effect of acceleration in this direction, the crystal is insensitive as the compressed and depressed parts of it have cancelling sensitivities. Therefore, we believe the Eu:YSO crystals can be very competitive with existing Fabry-Perot-based systems from that point of view.

In addition, since the deformation of the crystal matrix occurs in the elastic regime, which means no permanent deformation of the crystal happens, the modification of spectral holes is reversible. In other words, the tuning of spectral holes center frequency can be achieved by the applied stress field, shedding the light to the study of optomechanics in a mechanical resonator. Moreover, the ultra-stable laser which is achieved by locking to the spectral hole, can also be frequency adjusted by the

applied stress on the crystal if desirable for some applications.

3.5 Spectral Hole Broadening due to the Applied Stress

When there is an external stress applied on the crystal, the spectral hole not only has a frequency shift, but also has a broadening in the linewidth. The stress field, which may lead to energy level shift, will also cause a spectral linewidth broadening.

This section focuses on the uni-axial stress induced spectral hole broadening for different crystalline axes and sites. Our study starts from the spectral hole linewidth normalization definition, and follows with the quantitative study of the broadening. Finally, the possible reasons which may cause the hole broadening are discussed.

3.5.1 Spectral Hole Linewidth

In the spectral hole broadening study, each spectrum is fitted with the same model as the frequency shift study. The fitting model in Eq. 3.4.1 gives the full width at half maximum for each hole (which is simplified as linewidth in the following discussion), and symbolized as Γ_i in terms of the i_{th} recorded profile.

Uncertainty of the Linewidth

The uncertainty of the spectral hole width in each data point is defined as the reproducibility of the spectral hole in the following discussion, which is the standard deviation of Γ_i from four to six independent measurements. The uncertainty of the width determination coming from the fitting procedure is small, so it is negligible here.

3.5.2 Broadening Normalization to the Initial Hole Width

Initial Spectral Hole Linewidth

The experimental temperature used in our measurements is stabilized at 3.15 K. We also verified that from 3.1 K to 4.2 K the variation of the initial hole width is within the uncertainty of the width determination. Considering the servo loop of the temperature control makes the crystal actual temperature fluctuation to be below 1 mK, the initial width can be considered as constant in each sequence of measurement. This is also confirmed by doing a verification scan at the end of each measurement sequence with all the weights removed, and the recorded spectral hole linewidth is the same as the initial recorded hole linewidth (difference less than 2%).

In our measurement, the width of the initial spectral hole is $\Gamma_0(D_1S_1) = 5.4$ kHz, $\Gamma_0(D_1S_2) = 4.0$ kHz, $\Gamma_0(D_2S_1) = 3.8$ kHz, and $\Gamma_0(D_2S_2) = 4.4$ kHz. The difference of the initial hole width is up to 40%, so we start with removing the initial hole width by normalizing it out in the analysis of the broadening.

Model of Normalization to the Initial Hole Width

For the same magnitude of applied positive and negative pressure, the spectral holes have almost the same linewidth. So here we take the average value in the broadening study, as the equation

$$\Gamma_I = ({}^P\Gamma_i + {}^N\Gamma_i)/2,$$

where ${}^P\Gamma_i$ and ${}^N\Gamma_i$ present the linewidth of spectral holes with same amplitude of positive and negative pressure respectively. Γ_I is the average broadening value that used in our study. The index i is the serial number of the study which is the combination of measurement with positive and negative pressure with same magnitude.

The normalization of the spectral hole broadening is firstly defined as the Equation

below.

$$B_0 = \frac{\Gamma_I - \Gamma_0}{\Gamma_0},$$

where Γ_0 is the initial hole width for the analyzed axis and site. Figure 3-12 shows the normalized broadening B_0 with the uni-axially applied stress.

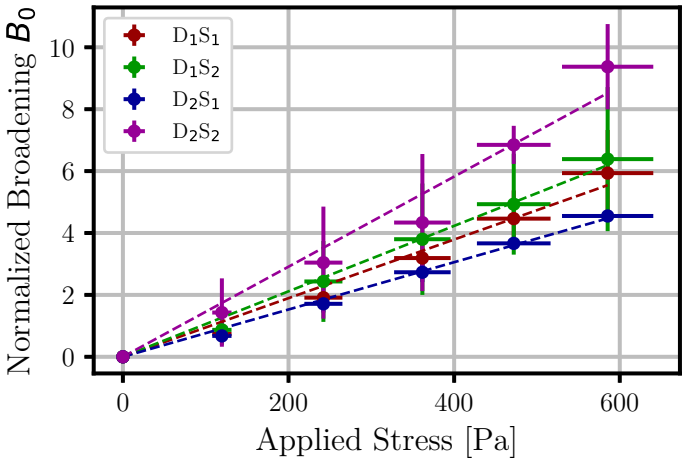

Figure 3-12: Broadening normalization to the initial hole width. The data point shows the normalized broadening B_0. The dashed lines are the linear fitting for the broadening.

In Fig. 3-12, the error bars of the data points contain the linewidth uncertainty as mentioned previously, which can be written as

$$\delta B_0 = -\frac{\Gamma_0 \delta\Gamma_I - \Gamma_I \delta\Gamma_0}{{\Gamma_0}^2}$$

as it shown in the Fig. 3-12.

By depositing the calibrated weights on top of the crystal, the recorded spectra shows a gradually increased linewidth in the shape. By observation, the spectral holes broadening is in line with a linear model, so the broadening of the spectral hole is modeled with a pure linear function

$$B_0 = b_0 \times P,$$

where b_0 is the linear coefficient of the broadening with the unit of Pa^{-1}. Since the $\Gamma_I \gg \Gamma_0$, so that $\delta(\Gamma_I - \Gamma_0) \approx \delta\Gamma_I$. Therefore, another broadening normalization model is carried out in the following section, considering the strain effect on the spectral hole.

3.5.3 Broadening Normalization to the Strain Sensitivity

Since the applied stress in our experiment is not perfectly uniformly distributed in the crystal, there is always some residual inhomogeneity of the stress field. The main cause of this residual inhomogeneity of the stress field is the crystal dimension which has a 0.5° uncertainty in the cutting. The cutting uncertainty lead to a leakage of the stress field on the not desired axes. For instance, if the external stress is supposed to be applied parallel to the D_1 axis, the D_2 and D_3 axes will have a tiny amplitude of stress because of the 0.5° projection.

Therefore, the broadening arising from the residual inhomogeneity depends on the strain sensitivity of the analysed axis and site, meaning that the same stress will cause greater broadening for the more sensitive axis and site. Based on this, the spectral hole linewidth is then normalized by taking into account the stress sensitivity. The stress sensitivity for each axis and site is referenced by the illustrated value in Tab. 3.1, $\kappa(D_1S_1) = 46 \pm 17$ Hz.Pa^{-1}, $\kappa(D_1S_2) = 137 \pm 16$ Hz.Pa^{-1}, $\kappa(D_2S_1) =$ -19 $\pm$ 10 Hz.Pa^{-1}, $\kappa(D_2S_2) =$ -213 $\pm$ 13 Hz.Pa^{-1}.

The broadening normalization to the stress sensitivity can be mathematically expressed as

$$B_1 = \frac{\Gamma_I - \Gamma_0}{\Gamma_0 \times \kappa_{ij}/\kappa_{11}}. \tag{3.5.1}$$

In the Eq. 3.5.1, κ_{ij} is the stress sensitivity coefficient for ith axis and jth site, *i.e.* $i, j = 1, 2$, and for example κ_{11} is the stress sensitivity of D_1 and Site 1.

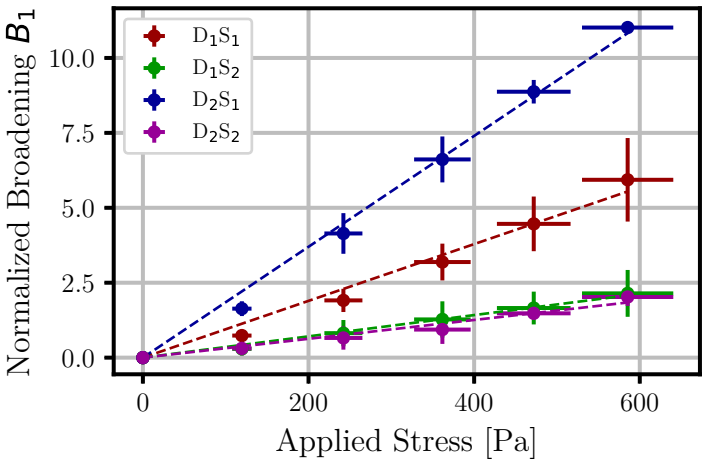

Figure 3-13: Spectral holes normalized broadening B_1 referenced to the stress sensitivity. The raw data is the same as used in Fig. 3-12 but with different analysis.

Figure 3-13 shows the broadening normalized to the strain sensitivity with the same data as Fig. 3-12 but normalized by the Eq. 3.5.1. So the error bars in the data point in the Fig. 3-13 are also in the similar definition as the reproducibility of the measurements. It is symbolized as δB_1 in Eq. 3.5.2, which considers the mathematical relationship of the variables in the fitting model,

$$\frac{\delta B_1}{B_1} = \frac{\delta \Gamma_I}{\Gamma_I} - \frac{\delta \Gamma_0}{\Gamma_0} - \frac{\delta \kappa_{ij}}{\kappa_{ij}} + \frac{\delta \kappa_{11}}{\kappa_{11}}. \tag{3.5.2}$$

The normalized broadening B_I is then fitted by a pure linear model

$$B_1 = b_1 \times P,$$

as the dashed lines showing in Fig. 3-13. The obtained broadening linear coefficient b_1 is tabulated in the Tab. 3.2 as a function of axis and site, corresponding to the curves in Figure3-13.

The uncertainty in the broadening linear coefficient b_1 contains two components, first is the fitting uncertainty of the linear model, and second is the repeatability of

Axis	Site	$(\text{kPa})^{-1}$
D_1	1	9.5 ± 4.6
D_1	2	3.6 ± 2.1
D_2	1	18.5 ± 0.2
D_2	2	3.1 ± 0.1

Table 3.2: Strain broadening coefficients b_1 obtained by normalization to the stress sensitivity.

several independent measurements (4 to 6 independent measurements for each case).

The normalization to the stress sensitivity provide the idea that the spectral hole broadening might be explained by the residual inhomogeneity of the stress field. Considering the not measured b axis, the further study with stress field projection along the b axis may shed more light on the understanding of spectral hole's broadening toward the uni-axial stress.

3.6 Summary and Discussion

We have investigated the europium ions stress sensitivity in a YSO crystalline matrix through the spectral hole burning technique. The calibrated weights allow us to deposit a certain amount of pressure on top of the crystal along D_1 or D_2 axis, achieving a uni-axial stress application. The uniaxial stress sensitivity of rare earth ions can be reflected on the spectral hole behavior, making it possible to study the mechanical properties through spectral hole burning technique.

The homogeneity of the applied stress field is important for both obtaining a well shaped spectral hole and also making the results be repeatable. We have carried out several technical development in order to experimentally optimize the stress field homogeneity. The motorized platform, which is to position the weights, can be movable in x, y, z directions. The platform movement along z axis allows the deposition of weights, and the movement in xy plane can help to get a well centered weights application position (relatively to the crystal geometry center position). We found it

is necessary to apply two thin layers of YSO powder on the top and bottom of the crystal, so that the non-flat contact surface caused stress field inhomogeneity can be reduced. Moreover, to avoid the disturbing electric field in the system, possible ways to prevent the charge collection is done, such as the grounding of all the relevant metal devices and motorized platform is covered by aluminium foil working as a shield of electromagnetic. In addition, since the spectral hole is sensitive to temperature fluctuations, the heat from the optical probing beam and motorized platform movement are all considered, and we conclude that in order to get a steady state, a 5-minute waiting time is needed in between each measurement sequence.

The study of spectral hole linear frequency shift gives us the linear stress sensitivity coefficient. The corresponding acceleration sensitivity of the spectral hole is also deduced that in a 8 mm $\times$8 mm $\times$4 mm crystal the spectral hole acceleration sensitivity is between 7 $\times 10^{-12}$ g^{-1} to 7 $\times 10^{-11}$ g^{-1} in terms of the most and least sensitive axis and site. This is comparable to the Fabry-Perot cavities, mounted on vibration insensitive mountings. Since our crystal is just simply put on top of a cylindrical holder, the mounting of the crystal still have a lot of space for improvements. So for the application in ultra-stable lasers, the spectral hole burning technique is a competitive candidate to the technique of Fabry-Perot cavity.

The spectral hole linewidth broadening due to the uni-axial stress is also investigated. The broadening normalization is firstly done by referring to the initial hole width. Because the main cause of the spectral hole broadening may come from the residual inhomogeneity of the applied stress field, we also studied the broadening by considering the stress sensitivity. Our results show that site 2 D_1 is the most sensitive axis and site in broadening with the coefficient of 18.5 $\pm$ 0.2 $(\text{kPa})^{-1}$. Future experiment about the b axis stress sensitivity will help us to better understand the broadening phenomenon.

Moreover, in terms of the strain-coupled nano-optomechanics, the uniaxial stress sensitivity of europium ions we provided here could be helpful in the observation of

quantum features of a mechanical resonator [12, 13, 54], making it possible to investigate an atomic force sensor through the spectral hole burning technique.

Conclusion and Perspective

Ultra-stable lasers have attracted the attention in scientific research as an essential tool for characterization with a wide range of applications. The spectral hole burning technique, directly on which the main work of this thesis is based, should allow one to achieve a laser with a better frequency stability (at the level of 10^{-17} or better), compared with the standard Fabry-Perot cavity based techniques (which are currently at the level of 10^{-16}). The rare earth ion-doped crystal suits the conditions for spectral hole burning process and is an appropriate material for this purpose due to a number of favourable factors: a narrow homogeneous linewidth, long hyperfine lifetime at cryogenic temperatures, a large number of participating ions, the agility in the engineering of the reference spectral structure, an (expected) low thermal noise, ... This thesis project has been devoted to improve the performance of ultra-stable lasers and eventually transfer the spectral purity to the other scientific domains which requires high-precision measurements.

Firstly, we improved detection noise in the system, which can directly affect the laser frequency stability.

Previous work on our experiment using single heterodyne detection scheme showed that the obtained frequency stability was limited by the detection noise. Our first investigation started with adding one more spectral hole in the detection scheme, where one narrow spectral hole is still used for laser locking while another large square hole (a 100-kHz wide hole with nearly constant transmittance at the center)

is employed for surrounding the monitor mode, in order to limited the noise from the phase dispersion. The error signal deduced from the phase dispersion in such a double heterodyne scheme allows us to reach a lower detection noise at low Fourier frequencies. As a result, our laser frequency stability has been increased about one order of magnitude (corresponding to an Allan deviations of 1.7×10^{-15} at 1 s) which is comparable to the so far best achieved frequency stabilities by spectral hole burning technique.

The double heterodyne detection scheme sheds light on how to further decrease detection noise by adding even more spectral features. In order to achieve the simultaneous multi-hole probing, the digital signal processing flowgraph has been improved accordingly. The optimization includes, first, the usage of the signal generation and reception through polyphase channelizer and polyphase synthesizer function in GNU Radio, and second, the employment of a phase re-wrap functional block. They all contribute to the synthesis of a phase continuous, multi-frequency signal with a cleaner spectrum (i.e. without spurious peaks arising from phase discontinuities). Further studies will therefore benefit from the improved signal-to-noise ratio based on the multiple holes technique. The first attempts with triple-hole probing have proven that a lower detection noise is indeed achievable by increasing the number of holes, even though the obtained laser frequency stability, locked to the triple holes pattern, did not yet reach the desired stability level. However, we are confident that the multi-hole probing method will allow us to reach a lower detection noise and therefore getting better frequency stability in the near future.

Moreover, we also investigated the temperature sensitivity of the spectral hole to the cryogenic environment, i.e. the temperature and isotropic pressures, the fine adjustment of which allowed us to minimize the sensitivity to temperature fluctuations. Since the new setup of our cryostat allows us to put the Eu:YSO crystal in a helium-gas surrounded cold chamber with a fixed volume, a tunable isotropic pressure can be applied on the crystal. By controlling the pressure, the frequency of the spectral hole will be modified according to its pressure sensitivity, which in turn

will modify its temperature sensitivity. Indeed, for a given quantity of He buffer gas, the temperature giving rise to the most insensitive range with respect to temperature fluctuations has been determined (the "magic" environment). The future plan of this study is to add a dilution refrigerator system, which allows us to explore even lower temperatures where the sensitivity, scaling as T^4 would be drastically reduced. A comparison between the "magic environment" and the dilution environment will allow us to determine the best strategy to minimize temperature induced noise for laser frequency stabilization.

Secondly, the Stark effect of Eu^{3+} ions has been experimentally studied. The obtained Stark coefficients allows us to have better understanding about the electric field noise in the ultra-stable laser system.

The Stark effect of europium ions cannot only characterize their properties but also provide useful information in the application of spectral hole burning techniques. Our study about the Stark effect on the Eu^{3+} in the YSO host matrix gives a quantitative description with respect to different crystal axes and sites, which is the first reported result to our knowledge. The linear Stark coefficients are reported with higher precision than those we found in the literature.

Moreover, the asymmetric quadratic Stark shift of spectral holes is important as it amounts to frequency shifts of the spectral hole at low field, thereby translating electric field noise to frequency noise of the spectral hole. The high precision measurement allows us to measure the quadratic Stark shift. Our first reported asymmetric quadratic Stark shift make it possible to estimate the upper limit of the electric field noise for a given laser frequency instability. For instance, by taking the upper limit of the quadratic coefficients as 1×10^{-3} Hz.m^2.V^{-2}, the desired 10^{-17} (at 1 s) relative frequency stability will require a E-field instability to be below 2.3 V.m^{-1}.

Thirdly, the acceleration sensitivity of spectral holes have been studied through the uni-axial stress measurement, providing useful information to minimize the vibration in the system.

The uniaxial stress applied on the Eu:YSO crystal will add modification on the crystal matrix, therefore making changes on the spectral hole. We recently reported the first calibrated uniaxial stress sensitivity measurement in the literature. The spectral hole center frequency shift and linewidth broadening has been studied with respect to the crystal sites and crystalline axes. The deduced acceleration sensitivity of the spectral hole burnt in our crystal varies from 1.5 $\times 10^{-11}$ g^{-1} to 1.3 $\times 10^{-12}$ g^{-1} depending on the stress applied axis and crystal sites. This result is comparable with Fabry-Perot cavities (around 10^{-12} g^{-1}), which have already optimized their mounting design. Consider our crystal is just simply mounted on a cylindrical pedestal, there is still a lot of space to improve the crystal mounting and therefore minimize the mechanical vibrations.

Moreover, the stress sensitivity measurement of spectral hole also inspires us to investigate the opto-mechanical coupling with spectral hole burning technique, which will then shed some light on applications in atomic force sensing. Our first attempts with a micro-scale resonator machined from a bulk crystal has shown the inhomogeneously broadened absorption spectrum of europium ions, indicating that contrary to micro/nano crystals, machining of a bulk crystal does not broaden the spectrum. Further development is needed in order to apply the ultra-low phase noise detection scheme to sense the motion of the micro-scale resonator.

Bibliography

[1] A. J. Freeman and R. Watson, "Theoretical investigation of some magnetic and spectroscopic properties of rare-earth ions," *Physical Review*, vol. 127, no. 6, p. 2058, 1962.

[2] L. Van Uitert, "Characterization of energy transfer interactions between rare earth ions," *Journal of the Electrochemical Society*, vol. 114, no. 10, p. 1048, 1967.

[3] C. Thiel, T. Böttger, and R. Cone, "Rare-earth-doped materials for applications in quantum information storage and signal processing," *Journal of luminescence*, vol. 131, no. 3, pp. 353–361, 2011.

[4] T. Zhong, J. M. Kindem, J. G. Bartholomew, J. Rochman, I. Craiciu, E. Miyazono, M. Bettinelli, E. Cavalli, V. Verma, S. W. Nam, *et al.*, "Nanophotonic rare-earth quantum memory with optically controlled retrieval," *Science*, vol. 357, no. 6358, pp. 1392–1395, 2017.

[5] C. Thiel, Y. Sun, R. Macfarlane, T. Böttger, and R. Cone, "Rare-earth-doped $LiNbO_3$ and $KTiOPO_4$ (ktp) for waveguide quantum memories," *Journal of Physics B: Atomic, Molecular and Optical Physics*, vol. 45, no. 12, p. 124013, 2012.

[6] N. Galland, N. Lučić, B. Fang, S. Zhang, R. Le Targat, A. Ferrier, P. Goldner, S. Seidelin, and Y. Le Coq, "Mechanical tunability of an ultranarrow spectral fea-

ture of a rare-earth-doped crystal via uniaxial stress," *Physical Review Applied*, vol. 13, no. 4, p. 044022, 2020.

[7] O. Gobron, K. Jung, N. Galland, K. Predehl, R. Le Targat, A. Ferrier, P. Goldner, S. Seidelin, and Y. Le Coq, "Dispersive heterodyne probing method for laser frequency stabilization based on spectral hole burning in rare-earth doped crystals," *Optics Express*, vol. 25, no. 13, pp. 15539–15548, 2017.

[8] R. Kolesov, K. Xia, R. Reuter, R. Stöhr, A. Zappe, J. Meijer, P. Hemmer, and J. Wrachtrup, "Optical detection of a single rare-earth ion in a crystal," *Nature Communications*, vol. 3, no. 1, pp. 1–7, 2012.

[9] J. Varignon, M. N. Grisolia, D. Preziosi, P. Ghosez, and M. Bibes, "Origin of the orbital and spin ordering in rare-earth titanates," *Physical Review B*, vol. 96, no. 23, p. 235106, 2017.

[10] M. Abraham, R. Weeks, G. Clark, and C. Finch, "Electron spin resonance of rare-earth ions in thorium oxide: Yb^{3+} and Er^{3+}," *Physical Review*, vol. 137, no. 1A, p. A138, 1965.

[11] R. Ahlefeldt, M. Pearce, M. Hush, and M. Sellars, "Quantum processing with ensembles of rare-earth ions in a stoichiometric crystal," *Physical Review A*, vol. 101, no. 1, p. 012309, 2020.

[12] K. Mølmer, Y. Le Coq, and S. Seidelin, "Dispersive coupling between light and a rare-earth-ion–doped mechanical resonator," *Physical Review A*, vol. 94, no. 5, p. 053804, 2016.

[13] J.-F. Motte, N. Galland, J. Debray, A. Ferrier, P. Goldner, N. Lučić, S. Zhang, B. Fang, Y. L. Coq, and S. Seidelin, "Microscale crystalline rare-earth doped resonators for strain-coupled optomechanics," *Journal of Modern Physics*, vol. 10, pp. 1342–1352, 2020.

[14] M. Schioppo, R. C. Brown, W. F. McGrew, N. Hinkley, R. J. Fasano, K. Beloy, T. Yoon, G. Milani, D. Nicolodi, J. Sherman, *et al.*, "Ultrastable optical clock with two cold-atom ensembles," *Nature Photonics*, vol. 11, no. 1, pp. 48–52, 2017.

[15] R. Tyumenev, M. Favier, S. Bilicki, E. Bookjans, R. Le Targat, J. Lodewyck, D. Nicolodi, Y. Le Coq, M. Abgrall, J. Guéna, *et al.*, "Comparing a mercury optical lattice clock with microwave and optical frequency standards," *New Journal of Physics*, vol. 18, no. 11, p. 113002, 2016.

[16] C. Lisdat, G. Grosche, N. Quintin, C. Shi, S. Raupach, C. Grebing, D. Nicolodi, F. Stefani, A. Al-Masoudi, S. Dörscher, *et al.*, "A clock network for geodesy and fundamental science," *Nature Communications*, vol. 7, no. 1, pp. 1–7, 2016.

[17] I. Ushijima, M. Takamoto, M. Das, T. Ohkubo, and H. Katori, "Cryogenic optical lattice clocks," *Nature Photonics*, vol. 9, no. 3, pp. 185–189, 2015.

[18] T. L. Nicholson, S. Campbell, R. Hutson, G. E. Marti, B. Bloom, R. L. McNally, W. Zhang, M. Barrett, M. S. Safronova, W. L. T. Strouse, G. F. Strouse, and J. Ye, "Systematic evaluation of an atomic clock at 2×10^{-18} total uncertainty," *Nature Communications*, vol. 6, no. 1, pp. 1–8, 2015.

[19] B. P. Abbott, R. Abbott, T. Abbott, M. Abernathy, F. Acernese, K. Ackley, C. Adams, T. Adams, P. Addesso, R. Adhikari, *et al.*, "Observation of gravitational waves from a binary black hole merger," *Physical Review Letters*, vol. 116, no. 6, p. 061102, 2016.

[20] X. Xie, R. Bouchand, D. Nicolodi, M. Giunta, W. Hänsel, M. Lezius, A. Joshi, S. Datta, C. Alexandre, M. Lours, *et al.*, "Photonic microwave signals with zeptosecond-level absolute timing noise," *Nature Photonics*, vol. 11, no. 1, pp. 44–47, 2017.

[21] K. Numata, A. Kemery, and J. Camp, "Thermal-noise limit in the frequency stabilization of lasers with rigid cavities," *Physical Review Letters*, vol. 93, no. 25, p. 250602, 2004.

[22] B. Young, F. Cruz, W. Itano, and J. Bergquist, "Visible lasers with subhertz linewidths," *Physical Review Letters*, vol. 82, no. 19, p. 3799, 1999.

[23] M. Notcutt, L.-S. Ma, J. Ye, and J. L. Hall, "Simple and compact 1-Hz laser system via an improved mounting configuration of a reference cavity," *Optics Letters*, vol. 30, no. 14, pp. 1815–1817, 2005.

[24] S. Häfner, S. Falke, C. Grebing, S. Vogt, T. Legero, M. Merimaa, C. Lisdat, and U. Sterr, "8×10^{-17} fractional laser frequency instability with a long room-temperature cavity," *Optics Letters*, vol. 40, no. 9, pp. 2112–2115, 2015.

[25] D. Matei, T. Legero, C. Grebing, S. Häfner, C. Lisdat, R. Weyrich, W. Zhang, L. Sonderhouse, J. Robinson, F. Riehle, *et al.*, "A second generation of low thermal noise cryogenic silicon resonators," in *Journal of Physics: Conference Series*, vol. 723, p. 012031, 2016.

[26] G. D. Cole, W. Zhang, M. J. Martin, J. Ye, and M. Aspelmeyer, "Tenfold reduction of brownian noise in high-reflectivity optical coatings," *Nature Photonics*, vol. 7, no. 8, pp. 644–650, 2013.

[27] J. M. Robinson, E. Oelker, W. R. Milner, W. Zhang, T. Legero, D. G. Matei, F. Riehle, U. Sterr, and J. Ye, "Crystalline optical cavity at 4 k with thermal-noise-limited instability and ultralow drift," *Optica*, vol. 6, no. 2, pp. 240–243, 2019.

[28] M. J. Thorpe, L. Rippe, T. M. Fortier, M. S. Kirchner, and T. Rosenband, "Frequency stabilization to 6×10^{-16} via spectral-hole burning," *Nature Photonics*, vol. 5, no. 11, pp. 688–693, 2011.

[29] R. Yano, M. Mitsunaga, and N. Uesugi, "Ultralong optical dephasing time in $Eu^{3+} : Y_2SiO_5$," *Optics Letters*, vol. 16, no. 23, pp. 1884–1886, 1991.

[30] R. W. Equall, Y. Sun, R. Cone, and R. Macfarlane, "Ultraslow optical dephasing in $Eu^{3+} : Y_2SiO_5$," *Physical Review Letters*, vol. 72, no. 14, p. 2179, 1994.

[31] R. Oswald, M. G. Hansen, E. Wiens, A. Y. Nevsky, and S. Schiller, "Characteristics of long-lived persistent spectral holes in $Eu^{3+} : Y_2SiO_5$ at 1.2 K," *Physical Review A*, vol. 98, no. 6, p. 062516, 2018.

[32] S. Zhang, N. Lučić, N. Galland, R. Le Targat, P. Goldner, B. Fang, S. Seidelin, and Y. Le Coq, "Precision measurements of electric-field-induced frequency displacements of an ultranarrow optical transition in ions in a solid," *Applied Physics Letters*, vol. 117, no. 22, p. 221102, 2020.

[33] N. Galland, N. Lučić, S. Zhang, H. Alvarez-Martinez, R. Le Targat, A. Ferrier, P. Goldner, B. Fang, S. Seidelin, and Y. Le Coq, "Double-heterodyne probing for an ultra-stable laser based on spectral hole burning in a rare-earth-doped crystal," *Optics Letters*, vol. 45, no. 7, pp. 1930–1933, 2020.

[34] N. Galland, *Vers des systèmes opto-mécaniques et mesures de haute précision à base de cristaux dopés aux terres rares.* PhD thesis, Université Grenoble Alpes (ComUE), 2019.

[35] V. Dolgovskiy, S. Schilt, G. Di Domenico, N. Bucalovic, C. Schori, and P. Thomann, "1.5 μm cavity-stabilized laser for ultra-stable microwave generation," in *2011 Joint Conference of the IEEE International Frequency Control and the European Frequency and Time Forum (FCS) Proceedings*, pp. 1–3, IEEE, 2011.

[36] F. Zheng, F. Fang, W. Chen, S. Dai, K. Liu, and T. Li, "Optical microwave generation with an ultra-stable fabry–perot cavity in a laser diode self-injection loop," *Optics Letters*, vol. 45, no. 5, pp. 1272–1275, 2020.

[37] R. Yano, M. Mitsunaga, and N. Uesugi, "Nonlinear laser spectroscopy of $Eu^{3+} : Y_2SiO_5$ and its application to time-domain optical memory," *Journal of the Optical Society of America B*, vol. 9, no. 6, pp. 992–997, 1992.

[38] O. Gobron, *Lasers ultra-stables asservis sur trous-brûlés spectraux: développement en vue d'une application aux horloges optiques.* PhD thesis, Université Pierre et Marie Curie-Paris VI, 2017.

[39] M. Dramićanin, B. Viana, Ž. Andrić, V. Djoković, and A. Luyt, "Synthesis of $Y_2SiO_5 : Eu^{3+}$ nanoparticles from a hydrothermally prepared silica sol," *Journal of Alloys and Compounds*, vol. 464, no. 1-2, pp. 357–360, 2008.

[40] F. Könz, Y. Sun, C. Thiel, R. Cone, R. Equall, R. Hutcheson, and R. Macfarlane, "Temperature and concentration dependence of optical dephasing, spectral-hole lifetime, and anisotropic absorption in $Eu^{3+} : Y_2SiO_5$," *Physical Review B*, vol. 68, no. 8, p. 085109, 2003.

[41] M. J. Thorpe, D. R. Leibrandt, and T. Rosenband, "Shifts of optical frequency references based on spectral-hole burning in $Eu^{3+} : Y_2SiO_5$," *New Journal of Physics*, vol. 15, no. 3, p. 033006, 2013.

[42] J. G. Proakis and D. G. Manolakis, *Digital signal processing: principles, algorithms, and edition*, pp. 794–804. Prentice Hall, Upper Saddle River, New Jersey, 1995.

[43] F. J. Harris, C. Dick, and M. Rice, "Digital receivers and transmitters using polyphase filter banks for wireless communications," *IEEE Transactions on Microwave Theory and Techniques*, vol. 51, no. 4, pp. 1395–1412, 2003.

[44] N. Timoney, B. Lauritzen, I. Usmani, M. Afzelius, and N. Gisin, "Atomic frequency comb memory with spin-wave storage in $^{153}Eu^{3+} : Y_2SiO_5$," *Journal of Physics B: Atomic, Molecular and Optical Physics*, vol. 45, no. 12, p. 124001, 2012.

[45] P. Jobez, N. Timoney, C. Laplane, J. Etesse, A. Ferrier, P. Goldner, N. Gisin, and M. Afzelius, "Towards highly multimode optical quantum memory for quantum repeaters," *Physical Review A*, vol. 93, no. 3, p. 032327, 2016.

[46] F. R. Graf, *Investigations of spectral dynamics in rare earth ion doped crystals using high resolution laser techniques*. PhD thesis, ETH Zurich, 1998.

[47] R. Macfarlane, A. Arcangeli, A. Ferrier, and P. Goldner, "Optical measurement of the effect of electric fields on the nuclear spin coherence of rare-earth ions in solids," *Physical Review Letters*, vol. 113, no. 15, p. 157603, 2014.

[48] A. Arcangeli, M. Lovrić, B. Tumino, A. Ferrier, and P. Goldner, "Spectroscopy and coherence lifetime extension of hyperfine transitions in $^{153}Eu^{3+} : Y_2SiO_5$," *Physical Review B*, vol. 89, no. 18, p. 184305, 2014.

[49] N. Carvalho, J.-M. Le Floch, J. Krupka, and M. Tobar, "Multi-mode technique for the determination of the biaxial Y_2SiO_5 permittivity tensor from 300 to 6 K," *Applied Physics Letters*, vol. 106, no. 19, p. 192904, 2015.

[50] F. R. Graf, A. Renn, U. P. Wild, and M. Mitsunaga, "Site interference in stark-modulated photon echoes," *Physical Review B*, vol. 55, no. 17, p. 11225, 1997.

[51] S. Zhang, N. Galland, N. Lučić, R. Le Targat, A. Ferrier, P. Goldner, B. Fang, Y. Le Coq, and S. Seidelin, "Inhomogeneous response of an ion ensemble from mechanical stress," *Physical Review Research*, vol. 2, no. 1, p. 013306, 2020.

[52] A. Ferrier, B. Tumino, and P. Goldner, "Variations in the oscillator strength of the $^7F_0 \rightarrow {}^5D_0$ transition in $Eu^{3+} : Y_2SiO_5$ single crystals," *Journal of Luminescence*, vol. 170, pp. 406–410, 2016.

[53] D. R. Leibrandt, J. C. Bergquist, and T. Rosenband, "Cavity-stabilized laser with acceleration sensitivity below 10^{-12} g^{-1}," *Physical Review A*, vol. 87, no. 2, p. 023829, 2013.

[54] S. Seidelin, Y. Le Coq, and K. Mølmer, "Rapid cooling of a strain-coupled oscillator by an optical phase-shift measurement," *Physical Review A*, vol. 100, no. 1, p. 013828, 2019.

Appendix A

List of Published Papers

- S. Zhang, N. Lučić, N. Galland, R. Le Targat, P. Goldner, B. Fang, S. Seidelin, and Y. Le Coq, "Precision measurements of electric-field-induced frequency displacements of an ultranarrow optical transition in ions in a solid," Applied Physics Letters, vol. 117, no. 22, p. 221102, 2020.

- N. Galland, N. Lučić, B. Fang, S. Zhang, R. Le Targat, A. Ferrier, P. Goldner, S. Seidelin, and Y. Le Coq, "Mechanical tunability of an ultranarrow spectral feature of a rare-earth-doped crystal via uniaxial stress," Physical Review Applied, vol. 13, no. 4, p. 044022, 2020.

- N. Galland, N. Lučić, S. Zhang, H. Alvarez-Martinez, R. Le Targat, A. Ferrier, P. Goldner, B. Fang, S. Seidelin, and Y. Le Coq, "Double-heterodyne probing for an ultra-stable laser based on spectral hole burning in a rare-earth-doped crystal," Optics Letters, vol. 45, no. 7, pp. 1930–1933, 2020.

- S. Zhang, N. Galland, N. Lučić, R. Le Targat, A. Ferrier, P. Goldner, B. Fang, Y. Le Coq, and S. Seidelin, "Inhomogeneous response of an ion ensemble from mechanical stress," Physical Review Research, vol. 2, no. 1, p. 013306, 2020.

- J.-F. Motte, N. Galland, J. Debray, A. Ferrier, P. Goldner, N. Lučić, S. Zhang, B. Fang, Y. L. Coq, and S. Seidelin, "Microscale crystalline rare-earth doped resonators for strain-coupled optomechanics," Journal of Modern Physics, vol. 10, pp. 1342–1352, 2020.

RÉSUMÉ

Les trous brûlés spectraux dans les cristaux dopés aux ions de terres rares sont des systèmes polyvalents, adaptés à la métrologie temps-fréquence et aux applications connexes. La transition optique étroite des ions dopants peut ainsi servir de référence pour la stabilisation en fréquence d'un laser. La stabilité de fréquence fractionnaire attendue peut potentiellement être de plusieurs ordres de grandeur meilleure que celle des lasers asservis sur des cavités Fabry-Pérot à température ambiante. L'objectif de ce projet de thèse est d'améliorer les techniques de stabilisation, et d'explorer les limites fondamentales de ces techniques. La sensibilité des trous spectraux vis-à-vis de contraintes uniaxiale, ainsi que d'un champ électrique externe a été caractérisée, de sorte que l'effet sur la fluctuation de la fréquence laser puisse être déduit et minimisé. Un environnement spécial a été également exploré, où l'effet des fluctuations de température sur la fréquence des trous spectraux peut être compensé au premier ordre par un décalage en sens inverse induit par un changement de pression. De plus, un travail important a été consacré au développement de techniques de détection à ultra-faible bruit, qui permettent d'obtenir un bruit de détection plus faible en utilisant différentes structures spectrales.

MOTS CLÉS

Laser ultra-stable, Ions de terres rares, Métrologie des fréquences

ABSTRACT

Spectral hole burning in rare-earth ion doped crystals is a versatile system in time-frequency metrology and related applications. The narrow optical transitions of the dopant ions can serve as a frequency reference for laser stabilization. The expected fractional frequency stability can potentially be orders of magnitude better than room temperature Fabry-Perot-cavity-locked lasers at the state of the art. The aim of this thesis project is to improve, and explore the fundamental limits of such techniques. The spectral holes' sensitivity towards the uni-axial stress and external E-field has been characterized, so that the effect on the laser frequency fluctuation could be deduced and minimized. A special environment has also been explored, where the effect of temperature fluctuations on the frequency of spectral holes can be compensated at first order by pressure-induced shift in the opposite direction. Moreover, much work has been devoted to the development of ultra-low-noise detection techniques, which allows getting lower detection noise by employing different spectral structures.

KEYWORDS

Ultra-stable laser, Rare-earth ions, Frequency metrology